NATIONAL AERONAUTICS AND SPACE ADMINISTRATION

Space Programs Summary 37-65, Vol. I

Flight Projects

For the Period July 1 to August 31, 1970

JET PROPULSION LABORATORY
CALIFORNIA INSTITUTE OF TECHNOLOGY
PASADENA, CALIFORNIA

September 30, 1970

NATIONAL AERONAUTICS AND SPACE ADMINISTRATION

Space Programs Summary 37-65, Vol. I

Flight Projects

For the Period July 1 to August 31, 1970

JET PROPULSION LABORATORY
CALIFORNIA INSTITUTE OF TECHNOLOGY
PASADENA, CALIFORNIA

September 30, 1970

SPACE PROGRAMS SUMMARY 37-65, VOL. I

Prepared Under Contract No. NAS 7-100
National Aeronautics and Space Administration

Preface

The Space Programs Summary is a multivolume, bimonthly publication that presents a review of technical information resulting from current engineering and scientific work performed, or managed, by the Jet Propulsion Laboratory for the National Aeronautics and Space Administration. The Space Programs Summary is currently composed of four volumes:

Vol. I. *Flight Projects* (Unclassified)

Vol. II. *The Deep Space Network* (Unclassified)

Vol. III. *Supporting Research and Advanced Development* (Unclassified)

Vol. IV. *Flight Projects and Supporting Research and Advanced Development* (Confidential)

Contents

Contents (contd)

I. *Mariner* Mars 1971 Project

A. Project Description

The primary objective of the *Mariner* Mars 1971 Project is to place two spacecraft in orbit around Mars that will be used to perform scientific experiments directed toward achieving a better understanding of the physical characteristics of that planet. Principal among these experiments are measurements of atmospheric and surface parameters at various times and locations to determine the dynamic characteristics of the planet. Approximately 70% of the Martian surface will be observed during a minimum of 90 days of orbital operations.

During Mission A, it is planned to map the topography of a large portion of the Martian surface at a resolution significantly higher than that achievable with earth-based methods or by the *Mariner* Mars 1969 spacecraft. In addition, measurements will be made of the composition, density, pressure, and thermal properties of the planet's atmosphere. Other measurements will be directed toward an understanding of Mars' surface temperatures, composition, and thermal properties (particularly at the polar caps); its apparent lack of internal activity; its mass distribution; and its shape.

During Mission B, data will be sought on time-variable features of the Martian surface associated with the wave of darkening wherein both seasonal and secular changes occur. Also, information on atmospheric structure and gross dynamics will be obtained, as well as information directed toward an understanding of Mars' mass distribution, its shape, and its apparent lack of internal activity.

A capability will exist to redirect goals for either mission to the alternate mission if desired. The two launches are anticipated for May 1971, with arrival at the planet during the following November.

An engineering objective of the project is to demonstrate the ability of the spacecraft to perform orbital operations in an adaptive mode wherein information from one orbital pass is used to develop the operations plan for subsequent orbital passes. Studies indicate a high probability that at least one of the spacecraft will survive the sun occultation period which occurs shortly after the 90-day mission is completed. This makes it possible to conduct an Extended Mission for about a year after orbit insertion. The Extended Mission will probably consist of one or two data taking sequences per week with the capability of recording and playing back about a half-recorder of data (16 TV frames and 11 min of spectrometer data).

One of the *Mariner* Mars 1971 flight spacecraft will be new, and the other will be the spare flight spacecraft of

the *Mariner* Mars 1969 Project modified to meet the requirements of the 1971 missions and to enhance mission reliability. The proof test model spacecraft of the *Mariner* Mars 1969 Project will be modified to become the proof test model for the *Mariner* Mars 1971 Project, to be used for preliminary testing and as a simulator in support of flight operations. A major modification for the *Mariner* Mars 1971 mission will be the addition of a rocket motor required to decelerate the spacecraft and place it in orbit around Mars.

Separate scientific instrument subsystems will be required to accomplish the television, infrared radiometer, ultraviolet spectrometer, and infrared spectrometer interferometer experiments given in Table 1. The S-band occultation and celestial mechanics experiments will require no additional equipment on the spacecraft.

Management responsibilities for the overall project, the Spacecraft System, the Mission Operations System, and the Tracking and Data System have been assigned to JPL.

Lewis Research Center has been assigned management responsibility for the Launch Vehicle System. The launch vehicle will be an *Atlas/Centaur* developed by General Dynamics/Convair.

The *Mariner* Mars 1971 missions will be supported by the Air Force Eastern Test Range launch facilities at

Table 1. *Mariner* Mars 1971 scientific experiments and principal investigators

Television	
H. Masursky	Team leader
H. Masursky	PI/U.S. Geological Survey
R. Batson	CI/U.S. Geological Survey
W. Borgeson	
M. Carr	
J. F. McCauley	
D. Milton	
R. Wildey	
D. Wilhelms	
J. Lederberg	PI/Stanford University
E. Levinthal	CI/Stanford University
J. B. Pollack	CI/Cornell University
C. Sagan	CI/Cornell University
G. de Vaucouleurs	PI/University of Texas
W. B. Thompson	PI/Bellcomm
G. A. Briggs	CI/Bellcomm
P. L. Chandeysson	CI/Bellcomm
E. N. Shipley	CI/Bellcomm
B. Smith	PI/New Mexico State University
M. E. Davies	CI/Rand Corp.
W. K. Hartmann	CI/Arizona State University
N. H. Horowitz	CI/Caltech
R. B. Leighton	CI/Caltech
C. B. Leovy	CI/University of Washington
T. B. McCord	CI/MIT
B. C. Murray	CI/Caltech
R. P. Sharp	CI/Caltech
Ultraviolet spectrometer	
C. Barth	PI/University of Colorado
C. W. Hord	CI/University of Colorado
J. B. Pearce	CI/University of Colorado

Infrared interferometer spectrometer	
R. A. Hanel	PI/Goddard Space Flight Center
B. J. Conrath	CI/Goddard Space Flight Center
W. A. Hovis	CI/Goddard Space Flight Center
V. Kunde	CI/Goddard Space Flight Center
G. V. Levin	CI/Biospherics
P. D. Lowman	CI/Goddard Space Flight Center
C. Prabhakara	CI/Goddard Space Flight Center
B. Schlachman	CI/Goddard Space Flight Center
Infrared radiometer	
G. Neugebauer	PI/Caltech
S. C. Chase	CI/Santa Barbara Research Center
H. Kieffer	CI/UCLA
E. D. Miner	CI/JPL
G. Munch	CI/Caltech
Celestial mechanics	
J. Lorell	Team leader
J. Lorell	PI/JPL
J. D. Anderson	CI/JPL
W. L. Martin	CI/JPL
W. L. Sjogren	CI/JPL
I. Shapiro	PI/MIT
M. Ash	CI/MIT
W. Smith	CI/MIT
S-band occultation	
A. Kliore	PI/JPL
D. L. Cain	CI/JPL
G. Fjeldbo	CI/JPL
B. L. Seidel	CI/JPL

PI = Principal investigator, who is the proposer for each experiment.

CI = Co-investigator, who assists the proposer on each experiment.

Team leader heads a particular group of PIs and CIs on an experiment where there is more than one PI.

Cape Kennedy, the tracking and data acquisition facilities of the Deep Space Network, and other NASA facilities.

B. Space Sciences

1. Testing and Selection of Vidicons for the *Mariner* Mars 1971 Television Subsystem

a. Introduction. This article describes the vidicon screening program established for the *Mariner* Mars 1971 project. This program has been used in selecting reliable vidicons for space flight, and also to increase the understanding of the performance characteristics of the slow-scan vidicon used in the *Mariner* Mars 1969 and 1971 television subsystems.

b. Vidicon description and requirements. The vidicon used in the *Mariner* Mars 1971 television subsystem is a specialized version of a common photoconductive sensor. The key component of a vidicon is the target, which consists of a transparent conductive coating on an optically flat faceplate covered by a thin film of a photosensitive semiconductor material. Figure 1 illustrates basic vidicon construction.

The photoconductor can be considered as an array of elements, each of which acts as a parallel-plate capacitor shunted by a photosensitive resistor. In the absence of illumination, the rear (cathode side) of the photoconductor is charged to cathode potential by the scanning electron beam. The front (illuminated side) of the photoconductor is biased to a positive potential (typically 10–20 V).

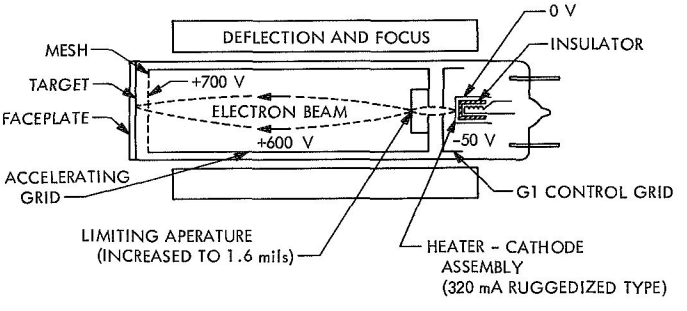

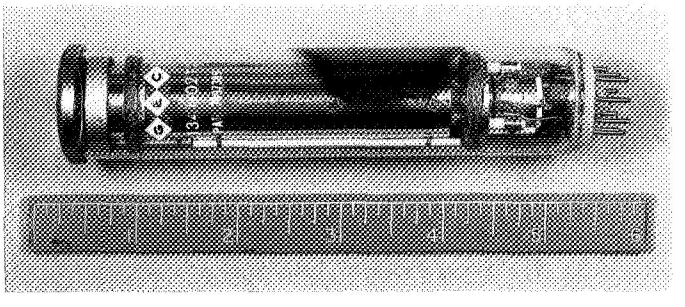

Fig. 1. Basic *Mariner* Mars 1971 vidicon construction

Illumination of the faceplate creates a photocurrent that discharges the target elements in proportion to the intensity of illumination. The electron beam then recharges the target elements, which results in a current in the signal lead.

The vidicon ancillaries include a scanning mechanism to move the electron beam across the target and an amplifier chain to process the signal current. Various types of vidicons utilize different combinations of magnetic and electrostatic focus and deflection to accomplish target scanning.

A slow-scan television system, such as that of *Mariner* Mars 1971, requires a vidicon with the ability to store an image for a long period of time. (Some slow-scan systems have readout times of several minutes.) Also, the *Mariner* Mars 1971 camera system requires the vidicon to have a reasonable response to the orange light in which Martian features have their highest contrast. The photoconductor and cathode must have stable characteristics for the life of the mission.

The vidicon must have adequate sensitivity to achieve the required signal-to-noise ratio of the system. In addition, the light transfer characteristics[1] of the tube must be held within certain limits to allow predictable operation of the automatic exposure control used in the *Mariner* Mars 1971 television subsystem. Also, at the scan rate used for this system, the vidicon dark current[2] is an appreciable portion of the signal current; therefore, a careful compromise must be made between sensitivity and dark current. Additional requirements are placed on the vidicon by the vibration expected during the launching of the spacecraft and by the temperature extremes expected in the mission.

c. Mariner Mars 1969 vidicons and changes for Mariner Mars 1971. The *Mariner* Mars 1971 television subsystem uses a vidicon very similar to that used on the *Mariner* Mars 1969 Project. The vidicon utilizes all magnetic focus and deflection. The tube is fully ruggedized and uses a special slow-scan photoconductor developed

[1]The light-transfer characteristic is a plot of the vidicon signal current as a function of faceplate illumination.

[2]Dark current is the vidicon signal current in the absence of faceplate illumination.

by the manufacturer (General Electrodynamics Corp., Garland, Texas).

The photoconductor is made of sulfur-doped selenium using a process proprietary to the manufacturer. The selenium–sulfur combination gives a more stable photoconductor than pure selenium and also has significantly more response to orange light. Figure 2 illustrates the spectral response characteristics of the two types of photoconductors.

The selenium photoconductive coating is deposited in the amorphous state and tends to revert to the more stable crystalline state with time. The sulfur doping acts to slow this ageing process, but does not eliminate it. The ageing process is accelerated at elevated temperatures and by repeated charge–discharge cycling of the photoconductor. The effect of this ageing process is to increase the sensitivity and dark current of the vidicon. With a slow-scan vidicon, this is a serious problem since the dark current is an appreciable portion of the signal. Another problem with slow-scan vidicons is that the area of the cathode that contributes to the signal current is small, which means that the vidicon is susceptible to a loss of signal current due to localized cathode damage caused by positive ion bombardment or local cathode defects.

Based on evaluation of the *Mariner* Mars 1969 vidicon failures, two changes were made in the vidicon design for *Mariner* Mars 1971. The changes were (1) incorporation of a ruggedized heater–cathode assembly and (2) enlargement of the beam-forming aperture in the electron gun.

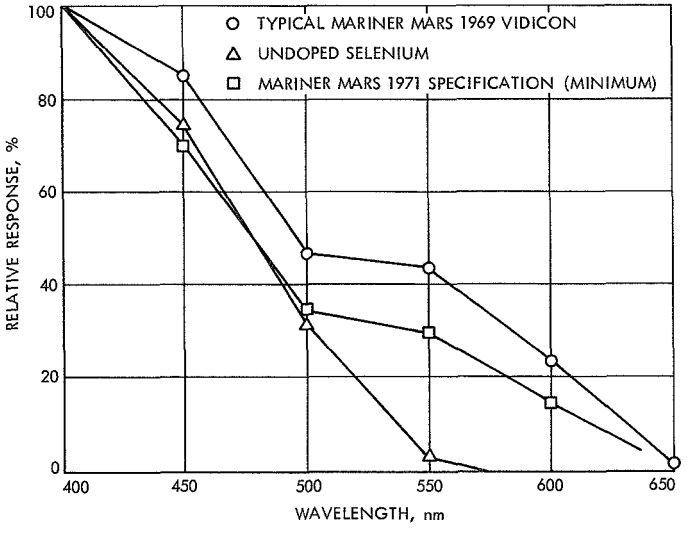

Fig. 2. Vidicon spectral response (constant video output)

The new heater employs a heavier wire and is completely isolated from the cathode by an insulating sleeve that provides additional shock and vibration resistance and also decreases the possibility of a filament-to-cathode short. The new filament requires more power to achieve the same cathode temperature due to the presence of the insulating sleeve.

The larger beam-forming aperture is intended to increase the vidicon reliability by increasing the area of the cathode that contributes to the scanning beam. This should make the vidicon less vulnerable to localized cathode damage.

d. Mariner Mars 1971 vidicon screening program. The vidicon screening program includes acceptance tests performed by the manufacturer and screening tests performed by JPL.

Testing performed by the manufacturer. The manufacturer is responsible for performing all testing involved in the production of electron tubes. Tubes which successfully complete the production cycle are subjected to a low-level vibration test to detect loose particles in the tube structure. The tubes are then tested at standard commercial scan rates to determine their suitability for slow-scan operation. Those vidicons which are found to be suitable are then tested at the *Mariner* Mars 1971 42-s scanning rate, using test equipment supplied by JPL. The vidicon operating voltages must be carefully adjusted during slow scan testing to achieve the best possible compromise between sensitivity, dark current, erasure performance, and other parameters.

The final test performed by the manufacturer is the slow scan acceptance test to verify that the vidicon meets the requirements set forth in the procurement specification.

Vidicon screening at JPL—objectives and procedures. The objectives of the screening program at JPL are to verify that the vidicon meets acceptance test requirements and to select reliable and stable tubes for use in flight cameras. The initial step of vidicon screening is the acceptance test, which is a duplicate of the test performed by the manufacturer. This test provides a check on vendor quality control, possible shipping damage, and provides baseline data for all subsequent JPL testing.

Additional tests performed at the time of the acceptance test are residual gas content (gas ratio), dark current vs target voltage, and cathode emission.

Stability of vidicon parameters is evaluated by subjecting the tube to a 100-h nonoperational ageing at 50°C, followed by three 50-h periods of operational ageing at 25°C, and at standard commercial scan rates. The vidicon is given a brief performance check at the end of each ageing period and a final acceptance test at the end of ageing. During this final test, the vidicon parameters are readjusted for optimum operation. Data taken during each of the performance checks, as well as during the initial and final acceptance tests, provide the basis for evaluation of critical vidicon parameters as a function of time.

The evaluation of screened vidicons is a somewhat subjective procedure. There are no absolute specifications applied to such parameters as sensitivity and dark current changes, cathode stability, and gas ratio. All of the *Mariner* Mars 1971 flight vidicons have been chosen on the basis of comparison with other vidicons available at the time of selection.

The two areas of greatest concern in vidicon screening are photoconductor stability and cathode reliability. As mentioned previously, the slow-scan photoconductor is an inherently unstable semiconductive coating. As the vidicon ages, the sensitivity and dark current gradually increase. If, during the mission, the dark current were to increase enough, the camera would be useless since no provision exists for readjusting the vidicon parameters in flight.

(1) *Photoconductor stability.* The evaluation of photoconductor stability is based primarily on changes in the dark current vs target voltage characteristic as a function of ageing time. This curve exhibits a "breakpoint" at which the dark current begins to increase rapidly with target voltage. Figure 3 illustrates a typical family of dark current curves. An attempt is made to select a target voltage that allows a maximum latitude for further increases in dark current while achieving a specified minimum sensitivity. A plot of sensitivity as a function of ageing time is also used in evaluating photoconduction stability. Other photoconductor characteristics considered in tube selection are blemishes,[3] residual image, and spectral response.

[3]A blemish is a photoconductor imperfection that most commonly takes the form of a small, high-conductivity spot on the target, which results in a white spot in the reproduced TV image.

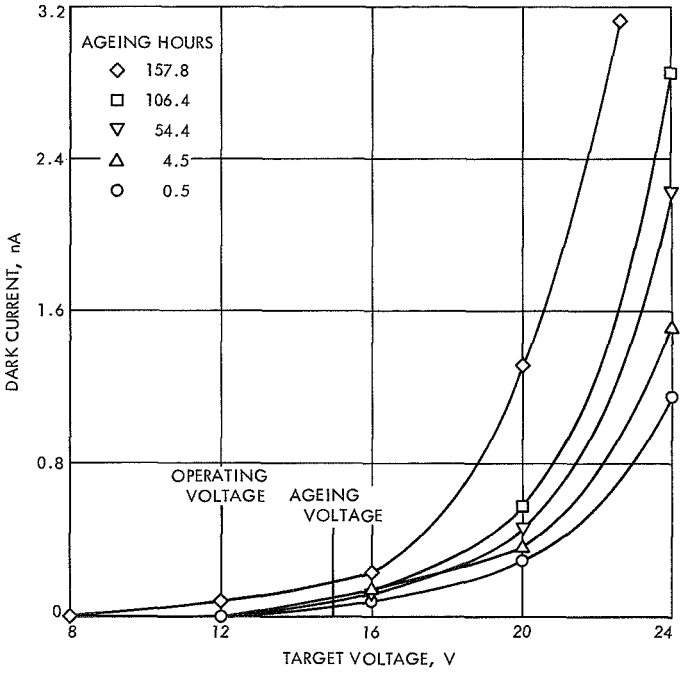

Fig. 3. Dark current as a function of target voltage

(2) *Cathode condition and emission stability.* Two tests are performed during screening to detect variations in cathode performance as a function of time. First, the cathode current obtained with fixed electrode potentials provides a measure of cathode emission decay as a function of operating time. The second test is designed to determine whether or not any degradation is occurring in the small region of the cathode producing beam current. This is accomplished by measuring beam current and cathode current and expressing the ratio of the two. This ratio should change if any change in cathode performance occurs in the region contributing to the beam.

Additionally, during initial acceptance tests, the maximum obtainable cathode current is measured. This is obtained by momentarily grounding the control grid and noting the cathode current.

(3) *Gas ratio.* The gas ratio test permits measurements of relative residual gas pressure within the vidicon. This is accomplished by generating positive ions with vidicon beam current electrons and measuring directly both the ion and electron current. The number of gas ions produced is proportional to the number of gas molecules present, the number and energy of ion-producing electrons present, and the ionization path length. Therefore, for any given vidicon configuration with constant accelerator electrode potential, the gas content will be directly related to the ratio of ion current and ion-producing

electron current. Selection of vidicons with the lowest gas content decreases the probability of cathode damage due to ion bombardment.

(4) *Other measurements.* Other parameters that are important to the performance of the camera system, but do not have a direct bearing on the reliability of the vidicon, are:

(a) Resolution. Resolution is measured using a slant-bar resolution target. This target has the line groups slanted so that measurements at different spatial frequencies may be made at constant electrical bandwidth.

(b) Residual image. Residual image is measured as the percentage of the signal from a high contrast scene, with the following frame dark.

(c) Spectral response. Spectral response measurement techniques are discussed under the test equipment description.

Description of Test Equipment

(1) *Mariner Mars Vidicon Test Set.* The vidicon screening program for *Mariner* Mars 1971 included the construction of two identical test sets, one for use at the vendor's facility, and the other for use at JPL. The vidicon test set (Fig. 4) was designed to use *Mariner* Mars 1971 flight-type circuits wherever practical both in order to test vidicons under conditions as close as possible to actual flight and to gain experience with the circuits.

The test set is built in two parts. The main console houses all the control circuitry, most of the signal chain electronics, power supplies, and the commercial test equipment (oscilloscope, digital voltmeter, and a TV monitor). The control panel has controls for all major vidicon parameters as well as focus and sweep adjustments. The vidicon test fixture houses the signal preamplifier, deflection coils, and shutter mechanism. The vidicon test fixture is designed to mount to a Photo-Research Corp. TV Optoliner, which has a calibrated light source with provision for insertion of neutral density filters and test targets. The vidicon test fixture is provided with an adaptor to mount to a Bausch and Lomb grating monochromator for spectral response measurements.

A valuable feature of the test set is the dual scan rate capability. Setup and testing of a camera system with a

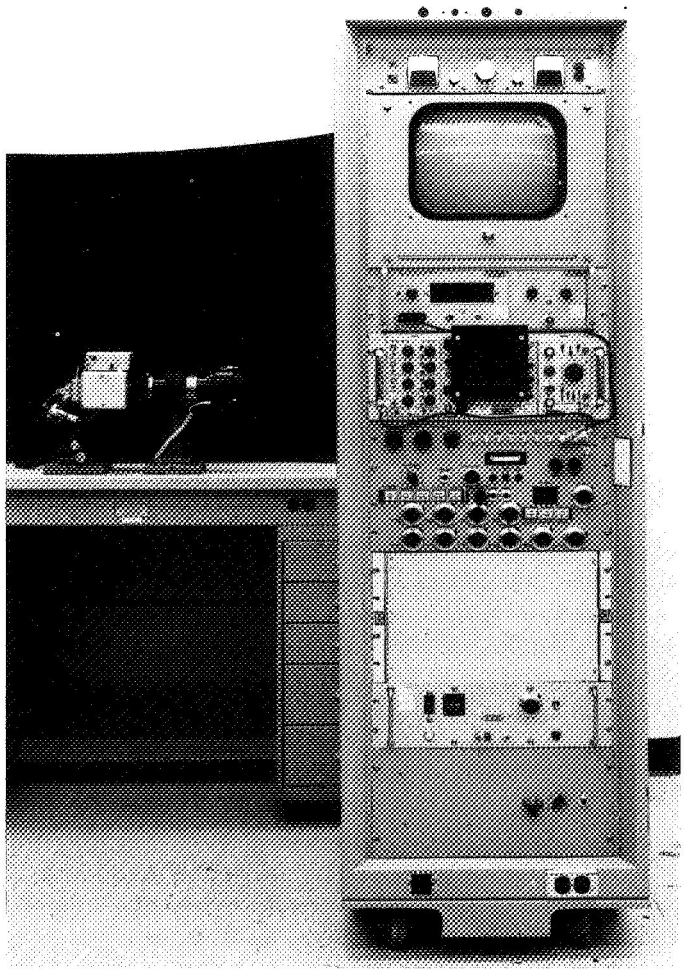

Fig. 4. *Mariner* Mars 1971 vidicon test set

42-s frame time is a very tedious procedure. This is avoided in vidicon testing by providing an accelerated scan rate for vidicon setup purposes. The test set operates in the normal 42-s frame rate with an erase interval having the number of erase cycles selectable from 1–14 (the *Mariner* Mars 1971 TV camera uses 14 cycles). In addition, the test set will operate in a 2-s frame mode with no erase interval. The 2-s frame mode is used not only for setup, but also for measurements of spectral response, blemishes, and other parameters not dependent upon frame time.

Other features of the test set are a self-calibrating signal chain, provision for triggering the oscilloscope on any one of the 700 scan lines, and an electronically generated cross-hatch pattern for evaluating raster distortion. The test set has protection circuits to prevent damage to the vidicon in the event of a sweep failure, or excessive high-voltage potentials.

(2) *Spectral response test equipment.* To measure spectral response, the monochromator replaces the TV optoliner as the light source. The monochromator is fitted with a controlled tungsten halogen light source and provides an output wavelength range of 400–800 nm. Response characteristics to monochromatic light of various wavelengths is measured by varying the input irradiance to produce a constant video output. Video output is read on a digital voltmeter using the video frame integrator provided in the test set. The monochromator output is calibrated using a thermopile detector and a Princeton Applied Research lock-in voltmeter system. The detector output is proportional to input power density and, when inverted and normalized to the maximum response, produces the relative spectral response of the vidicon.

(3) *Ageing test set.* The ageing test set provides capability for unattended operational ageing of two vidicons simultaneously. This test set consists of a modified commercial 945-line, standard frame rate television camera and monitor components. Protection circuits have been added so that the vidicon tube cannot be damaged by either circuit or power malfunction, or operator error. During operational ageing, the vidicon has normal *Mariner* Mars 1971 electrode potentials applied and operates in an open shutter mode. The input light level is set just below saturation for a cathode current of 20 μA.

(4) *Gas ratio test set.* The gas ratio test set consists of battery and power supply voltage sources together with the switches and metering circuits necessary to permit measurement of the small currents that constitute the gas ratio.

e. Screening results and vidicon performance characteristics

Cathode Damage and Emission Stability. Data obtained during stability testing has shown great tube-to-tube variability in cathode emission as a function of operating time. Because of this, emission has become the most important indicator of the potential life of a cathode. The rate of emission decay allows a comparison to be made between vidicons. All other things being equal, the vidicon showing the smallest rate of decay would be selected for flight.

As mentioned previously, maximum cathode emission is also measured. On the basis of this data alone, several vidicons have been rejected because this parameter decreased below the specified minimum during the course of screening. The test relating beam current to cathode current has produced no indication of localized cathode damage. This can mean either that no such damage exists or the test is incapable of detecting it. Further, since cathode ion damage should be related to gas content, it was hoped that a correlation could be found between cathode condition and gas ratio; unfortunately, no such correlation was found.

The gas ratio test, even though it has not been correlated to cathode condition measurements, has been useful in vidicon selection. By accumulation of gas ratio data on *Mariner* Mars 1969 and 1971 vidicon tubes, an acceptable gas ratio limit has been determined. This value is used as a basis for quality comparison during acceptance testing. Additionally, by making two gas ratio measurements separated in time, leaks in the base pin glass-to-metal seals can be detected. Experiment has verified the correlation of an abnormally high gas ratio and cracks in the glass-to-metal base pin seals of the vidicon.

Photoconductor characteristics. At the beginning of the *Mariner* Mars 1971 screening program, the objective was to select vidicons with stable photoconductors using plots of sensitivity, dark current, and blemishes with ageing time. Some of the sensitivity data were erratic and dark current plots showed little variation for tubes with low dark current and large increases for those with high dark currents. Blemish data tended to be inconclusive.

The screening techniques were modified to select the target voltage to be used during ageing based on dark current measurement rather than using manufacturer's recommended values, and to take dark current data in the form of the dark current vs target voltage curve shown in Fig. 3. Observation of the changes in the dark current characteristic with ageing time has provided much more consistent results than earlier methods, and is now used as the single most useful indication of vidicon photoconductor stability. Sensitivity characteristics are used as backup information and generally show good correlation with the dark current data.

Blemishes give the appearance of increasing in size and number with ageing time. It has been speculated that the apparent increase in number is simply an increase in the *detectability* of blemishes as the dark current increases. Vidicons have not been rejected on the basis of blemish data unless an abnormal number or distribution is observed during screening.

Typical vidicon spectral response is shown in Fig. 2. No conclusions have been reached on the change in spectral response characteristics with ageing time and spectral response information is primarily used for calibration and for selection of the camera (wide or narrow angle) in which the vidicon will be used. The automatic exposure control used on *Mariner* Mars 1971, coupled with the eight-position filter wheel used on the wide-angle camera, makes it necessary to select a vidicon that provides the best balance between exposures with the different filters.

The residual image performance of the *Mariner* Mars 1971 vidicons remains a significant problem. One vidicon was rejected in screening for excessive residual image. Typical residual image when used in the *Mariner* Mars 1971 erase mode is 1–3%, measured against a dark field. Other measurement techniques give very different results, indicating a need for a better measurement procedure.

In summary, the selection of flight vidicons has been based on initial acceptance testing, cathode stability, and photoconductor stability. Spectral response, residual image, resolution, blemishes, and other characteristics have played a relatively minor role in the selection process. Selection of vidicons is based to a large degree on comparison with other tubes available, rather than comparison to an absolute specification.

f. Areas for improvement in future screening programs

Spectral response. The technique discussed for measurement of spectral response gives relative response measurements rather than absolute. It would be useful to have absolute measurements to facilitate comparison of tubes in a specific wavelength range and also to simplify exposure and spectral filter calculations. Another problem with currently used spectral response techniques is in specifying the signal level at which measurements are to be taken. Transfer curves taken at several different wavelengths show that the selection of operating point has a large effect on the shape of the response curve. The optimum method, of course, would be to take the entire set of transfer characteristics for each vidicon; however, this would be extremely time consuming.

Cathode condition. As mentioned previously, no evidence of localized cathode damage has been found. Possibly the only way of verifying the validity of the test will be to attempt to induce cathode damage in a vidicon that has a high gas content and then try to detect the damage. Even though there is increased confidence in the cathodes through use of the gas ratio test, it would be extremely helpful to develop a proven test for localized damage.

Residual image. Recent system test results, as well as the vidicon test data, have shown that the residual image measurement procedure is very poorly defined. A variation of 3/1 in the residual signal (expressed as a percentage of the reference signal) can be obtained by using different measurement techniques. A comprehensive study of the residual image characteristics of the *Mariner* Mars 1971 vidicon is being undertaken, with the objective of defining proper measurement procedures, defining methods for removal of residual image from pictures, and studying methods of residual image reduction through hardware modification or special picture-taking sequences. While it has no effect on reliability, the residual image performance of the *Mariner* vidicon stands out as one of the more serious problems.

g. Conclusion. The *Mariner* Mars 1971 vidicon test and screening program represents an attempt to increase the understanding of the performance characteristics of the vidicon and to increase confidence in the reliability of the vidicon for an extended space mission. Although it is too early to judge the success of the latter, it may be noted that all flight systems have now been assembled and have logged considerable test time with no vidicon failures or gross parameter changes. (The prototype TV suffered a cracked vidicon caused, it is believed, by an excessively low test temperature.)

Perhaps the most useful screening tests developed during the *Mariner* Mars 1971 vidicon screening program have been the photoconductor stability test and the gas ratio test. The dark current stability curves have provided a useful method of choosing an operating target voltage to give maximum vidicon reliability consistent with adequate sensitivity. The gas ratio test has given a high degree of confidence in the mechanical integrity of the vidicons, even though the anticipated correlation between gas ratio and cathode condition was not found. Two *Mariner* Mars 1971 vidicons having much higher than average gas ratios were also found to have cracks by the pin seals. These were returned to the vendor for replacement. Other tests and screening procedures have yielded useful data, but have not completely fulfilled the objectives of the screening program or are not sufficiently accurate for use as component calibration data. Specific measurement techniques needing further development for future programs are those for spectral response, cathode condition, and residual image.

C. Guidance and Control

1. Orbiter Power Subsystem

a. Introduction. *Mariner* Mars 1971 Orbiter mission requirements necessitated a number of changes in the *Mariner* Mars 1969 power subsystem design. The major modification is a new battery design, which incorporates 26 nickel–cadmium cells, selected to replace the 18-cell silver–zinc battery used on *Mariner* Mars 1969. The battery was changed because of the increased number of cycles required, and also because the increased dependency of the mission upon battery performance during the Mars' orbit insertion sequence requires a battery with an extended lifetime.

Mariner Mars 1971 uses a slightly modified *Mariner* Mars 1969 solar array. The modifications consist of reducing the number of solar panel temperature sensors from two to one and providing outriggers to mechanically extend the *Mariner* Mars 1969 solar panel to accommodate the larger propulsion fuel tanks.

The power subsystem conditioning electronics (PCE) for the *Mariner* Mars 1971 was also modified to provide for more complex switching and power distribution and to accommodate the greater power requirements of the mission. This article describes the *Mariner* Mars 1969 PCE modifications necessary to obtain the *Mariner* Mars 1971 design (Fig. 5).

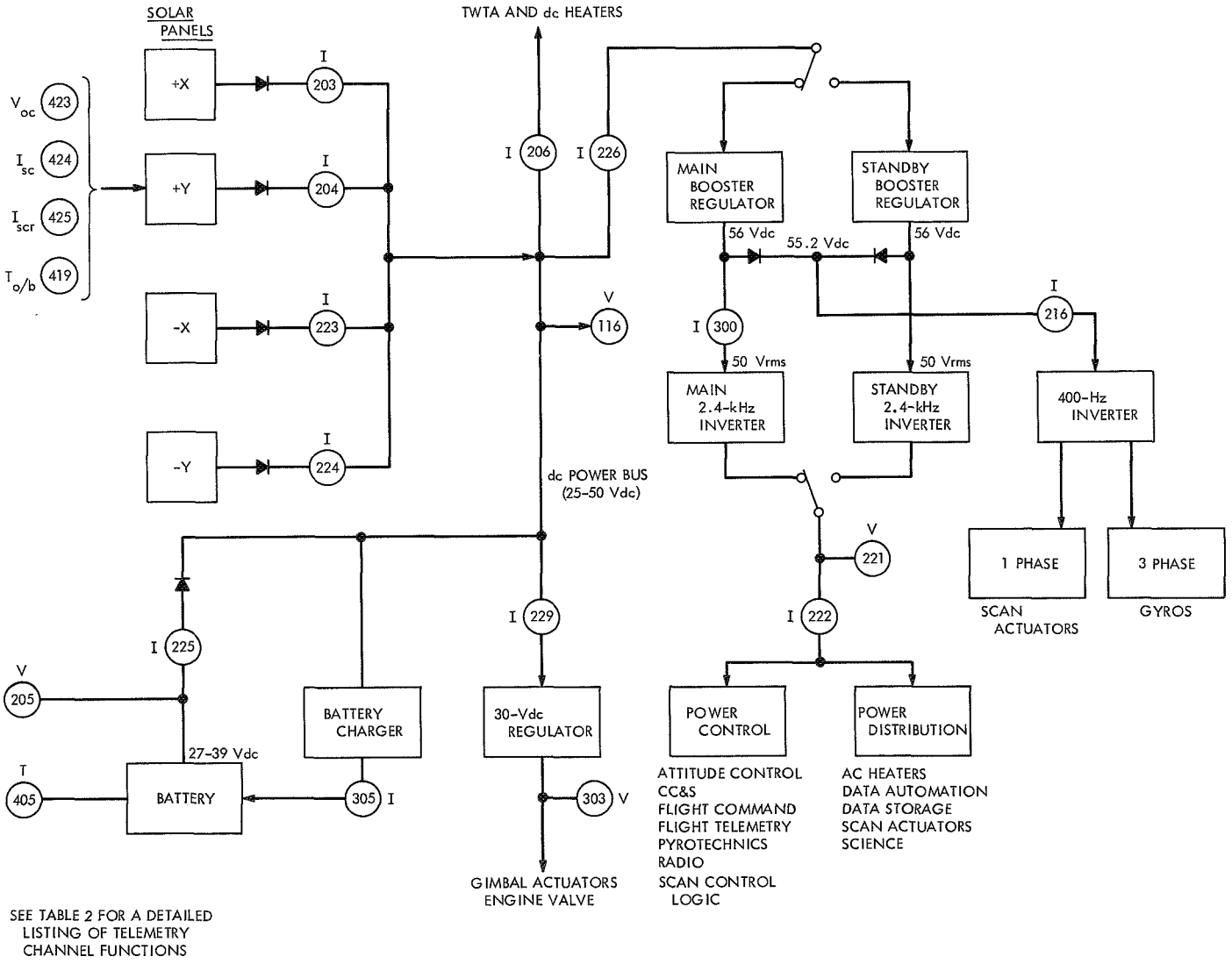

Fig. 5. *Mariner* Mars 1971 power subsystem

b. Battery charger. One of the major PCE changes is a modified battery charger that recharges the nickel–cadmium battery at a high charge rate (2.0 A), used to recharge the battery in a short time interval, and a low rate (0.65 A), used to maintain full battery capacity when the battery is not required for spacecraft loads. The high charge rate will be used after such sequences of battery use as post-launch, or possibly post-maneuver. The high-rate charger is a pulse-width modulated switching regulator. Constant-current regulation is maintained by duty-cycle variation of the series regulator as a function of output current changes. The low, or trickle, charge rate is provided by a constant-current series regulator whose fixed output of 0.65 A is controlled by the voltage developed across a resistor in series with its output.

The *Mariner* Mars 1971 battery charger contains circuits to automatically change the high charge rate to the low rate at times of:

(1) Full battery charge. As the battery terminal voltage reaches 37.5 V, the charger voltage detection circuit will sense the battery approaching full charge and automatically cause the charger to switch to the low-rate mode.

(2) High battery temperature. Automatic transfer to the low rate is made if the battery reaches 100°F during high-rate charge.

This automatic function is not reversible (i.e., the charger is not switched to high rate when voltage drops below 37.5 V).

The battery charger may be commanded to toggle on or off, or to charge at high or low rates, by either a direct ground command or one stored in the central computer and sequencer (CC&S). The charger can also be ground-commanded to retain a given charge rate under any operating mode by inhibiting the automatic switchover function.

c. 30 Vdc regulator. This regulator, new to *Mariner* power conditioning circuitry, is used on the *Mariner* Mars 1971 Orbiter to provide the input power requirements of the gimbal actuators and the propulsion engine valve. The unit is a pulse-width modulated down regulator and dc-to-dc converter with a power rating of 150 W maximum that provides an output voltage of 30 Vdc $\pm$ 5%. The main power source for the module is the dc power bus; its operation is controlled by a relay in the regulator, energized by a command from the attitude control subsystem. The module provides an isolated output to the users who reference their signal returns to the spacecraft structure, from which the power return is isolated.

d. Power source and logic. The *Mariner* Mars 1971 power source and logic (PS&L) houses the share-mode detector and boost converter circuitry. These circuits, which detect and relieve the power subsystem of an unnecessary battery-array share mode, were located in the *Mariner* Mars 1969 battery charger module. The *Mariner* Mars 1971 PS&L also houses the battery test load relay that was located in the *Mariner* Mars 1969 heater and dc power distribution module.

As with all *Mariner* power subsystems, the *Mariner* Mars 1971 PS&L conducts all spacecraft input electrical power, whether generated by the solar array, battery, or an external source. It also contains both the diode logic to automatically switch in battery power to supplement array power upon spacecraft demand and the motor-driven switch that transfers power at launch from the external power supply to the battery. The modified PS&L was able to accommodate the additional circuitry required by using welded modules to reduce the volume of the existing circuits. (These welded modules are being used in the *Mariner* power subsystem for the first time.) Circuits used repetitively in the power subsystem, i.e., telemetry and command circuits and some of the regulated supplies used for command functions, were packaged in these modules.

e. Power distribution. Due to the requirement for greater flexibility for load switching *Mariner* Mars 1971 power distribution is more intricate than that provided for *Mariner* Mars 1969. On *Mariner* Mars 1969, all science loads were simultaneously switched on or off; the *Mariner* Mars 1971 mechanization will permit the switching of individual science instruments, which will afford better power distribution management with the limited power capability of the solar array in the Mars environment. It will also permit greater utilization of instruments during post-encounter investigations as the spacecraft heliocentric distance increases. Moreover, an instrument may be switched out of operation in the event that its failure loads the power subsystem or affects the performance of other instruments thus minimizing the damage to the total mission. Both the *Mariner* Mars 1969 power distribution and heater and power distribution modules were modified to obtain the new switching

capability, and these are now called the power distribution modules A and B, respectively.

More efficient spacecraft power utilization on *Mariner* Mars 1971 will be obtained by further modifications to enable:

(1) Commanding the operation of only the roll gyro at times the pitch and yaw gyros are not required.

(2) Transferring the heaters that formerly operated from the 2.4-kHz bus to the dc power bus. These heaters toggle on to maintain a proper ambient temperature as the science instruments are commanded off. Eliminating the booster regulator and 2.4-kHz inverter losses required when powering the heaters from the ac bus saves dc power.

The operation of the booster regulators and 2.4-kHz inverters is the same as for *Mariner* Mars 1969. However, the mission requirements necessitate increasing the booster regulator power rating from 250 to 295 W and the inverters from 200 to 250 W. Information regarding *Mariner* Mars 1969 power subsystem equipment that remain unchanged for *Mariner* Mars 1971 may be found in SPS 37-47, Vol. I, pp. 2–3, and 37-51, Vol. I, pp. 13–19.

f. Power subsystem telemetry. *Mariner* Mars 1971 power subsystem telemetry transducers are given in Table 2. Their location is noted in Fig. 5. In addition to those listed, telemetry channel 406 will telemeter the position of relays that control the battery charge rate, charger rate transfer, and the boost converter operation. Also, telemetry channels 411 and 434 will provide temperature data for PCE bays I and II, respectively.

Table 2. *Mariner* Mars 1971 Orbiter power subsystem telemetry channels

Telemetry channel	Function
116	PSL output voltage
203	+X solar panel current
204	+Y solar panel current
205	Battery voltage
206	RFS and dc heater current
216	400-Hz inverter input current
221	2.4-kHz inverter output voltage
222	2.4-kHz inverter output current
223	−X solar panel current
224	−Y solar panel current
225	Battery output current
226	Booster regulator input current
229	30-Vdc regulator input current
300	Main 2.4-kHz inverter input current
303	30-Vdc regulator output voltage
305	Battery charger output current
405	Battery temperature
419	+Y solar panel outboard temperature
423	Standard cell voltage
424	Standard cell current
425	Radiation-resistant cell current

2. Scan Actuator

The *Mariner* Mars 1971 scan actuator is identical to the *Mariner* Mars 1969 actuator except for a minor change in the mounting configuration. An additional mounting hole was added to the existing unit to provide for a shift in the clock axis range of 12.8 deg. With the addition of this small change, the *Mariner* Mars 1971 hardware requirements were satisfied by refurbishment of *Mariner* Mars 1969 units.

Three sets of actuators (two actuators per set) have been flight qualified for *Mariner* Mars 1971. Originally, these actuators were used as the *Mariner* Mars 1969 engineering prototype, proof test model, and flight spare sets. Qualification of the units was accomplished by rebuilding and testing the prototype and proof test model sets; bench testing only was performed on the flight spare set. Rebuilding included complete disassembly, inspection, cleaning, and relubrication of all bearings. A few parts that revealed wear or stress by previous evaluation and type approval testings were replaced.

The scan actuator and its functional characteristics have been described previously (Ref. 1). Figure 6 shows rear- and front-view cutaways of the actuator.

Reference

1. *Proceedings of the Fourth Aerospace Mechanisms Symposium*, Technical Memorandum 33-425. Edited by G. G. Herzl and M. F. Buehler. Jet Propulsion Laboratory, Pasadena, Calif., Jan. 15, 1970.

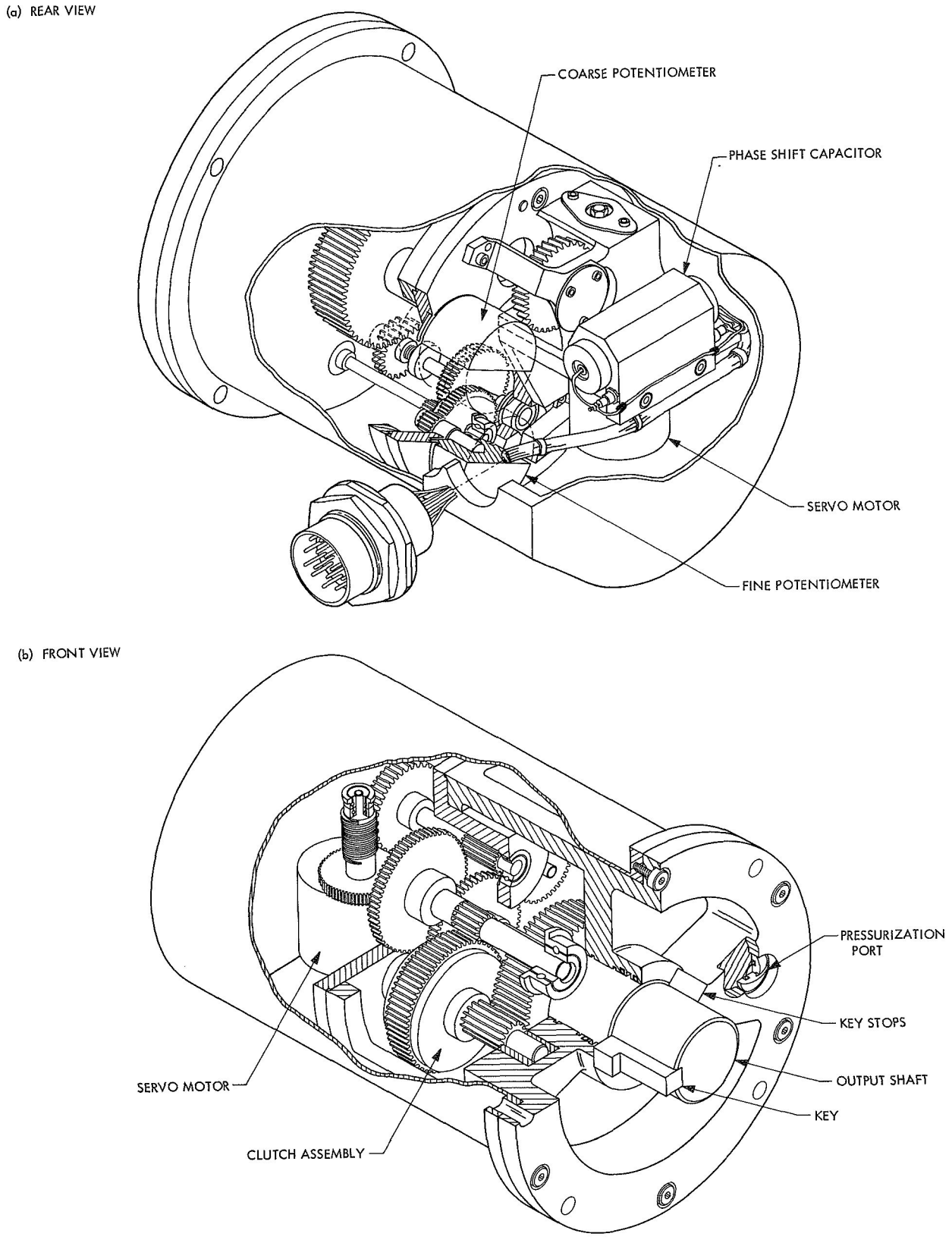

Fig. 6. *Mariner* Mars 1971 scan actuator

3. Sun Acquisition Performance with Latched Solar Panels

a. Introduction. This article discusses the operation of the *Mariner* Mars 1971 attitude control subsystem and the Sun acquisition performance while the solar panels are in their latched configuration. Sun acquisition performance with latched solar panels is of concern for the late launch opportunities where spacecraft separation will occur in a sunlit condition.

At spacecraft separation, the attitude control subsystem is turned on and Sun search initiated by a signal from the pyro arming switch. Following separation, approximately 3 min elapse (separation initiated timer) before solar panel deployment. During this time, the spacecraft will attempt to acquire the Sun with the solar panels in their latched configuration.

The results of an analysis and computer simulation of this mode of operation indicates that an unstable null exists around the desired Sun-acquired orientation ($-Z$ axis pointing at the Sun). A stable null was found to exist with the spacecraft roll axis oriented 90 deg from the Sun direction. In this orientation, the position of the Sun is at a spacecraft cone-angle of 90 deg. Spacecraft clock-angle position of the Sun will depend on the initial conditions at separation.

b. Discussion. The acquisition Sun sensors for the *Mariner* Mars 1971 spacecraft are located on the ends of the solar panels. Previous *Mariner* spacecraft had these sensors mounted near the central bus structure at the base of the solar panels. This was not feasible for the *Mariner* Mars 1971 spacecraft due to the shadowing created by the antenna and propulsion tank structure.

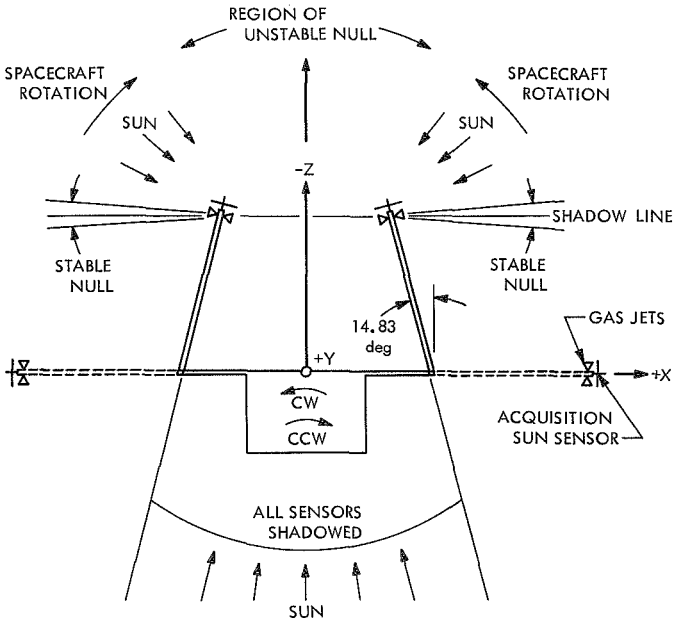

Fig. 7. Sun acquisition geometry with latched solar panels

One acquisition Sun sensor is located on the end of each solar panel. Two fine (cruise) Sun sensors and a Sun gate are located on the +Y solar panel outrigger structure. When the solar panels are deployed, the combined field of view of the four acquisition and two cruise Sun sensors is 4π sr. These sensors provide pitch and yaw axis error signals, measuring the angular deviation of the Sun line from the negative roll axis of the spacecraft. When this cone-angle deviation is between 3 to 6 deg, the Sun gate switches out the acquisition sensors and Sun acquisition is completed with the fine Sun sensors.

The following changes in the attitude control configuration are present when the solar panels are in their latched configuration (Fig. 7):

(1) The combined field of view of the four acquisition Sun sensors is reduced to approximately 2π sr. A large dark region exists in the rear hemisphere containing the spacecraft +Z axis. This results from the orientation of the Sun sensors and the shadowing presented by spacecraft solar panels and bus structure.

(2) The cruise Sun sensors and Sun gate are completely shadowed by the folded panels.

(3) Gas jet polarities remain the same, but their effective lever arms are reduced and they no longer function in couples. Pitch and yaw gas jet lever arms are reduced from 10.92 ft to 6.14 ft. Roll jet lever arms are reduced to 1.625 ft.

The acquisition and cruise Sun sensors are connected in a bridge arrangement as shown in Fig. 8. Each acquisition Sun sensor has three photo-sensitive cadmium-sulphide cells. The resistance of each cell depends on its angular deviation from the Sun direction, i.e., the resistance of a cell is inversely proportional to the amount of light impinging on its photo-sensitive surface and a totally dark cell has, for all practical purposes, an infinite resistance. Referring again to Fig. 7, attitude control operation in the region of the unstable null can be explained in the following simple terms (the panels in their deployed position are shown with dotted lines): With the panels deployed, consider as an example, a clockwise

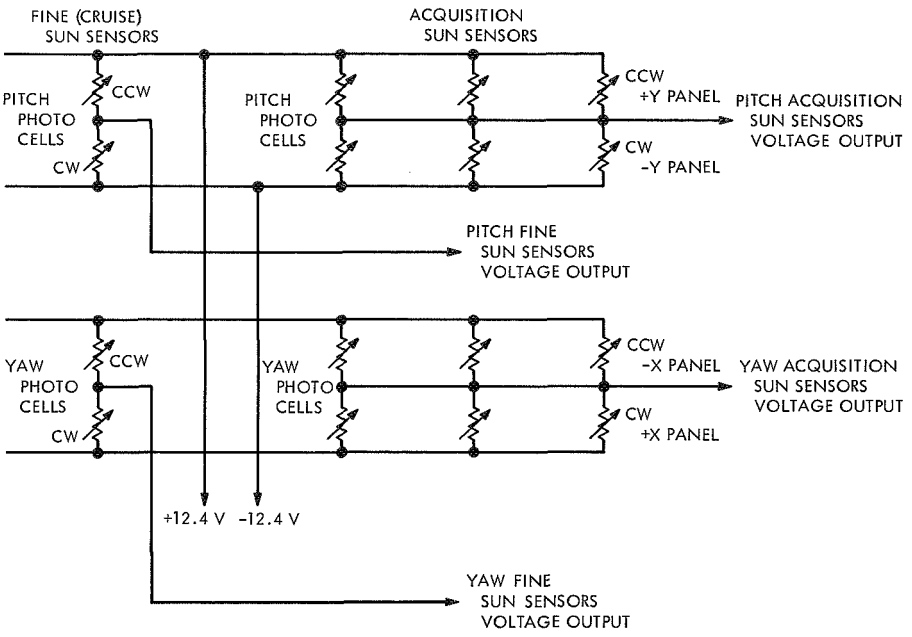

Fig. 8. *Mariner* Mars 1971 sun sensor schematic

(CW) yaw error. To correct this error, the spacecraft must rotate counter-clockwise (CCW) about yaw. To rotate CCW, the resultant output voltage from the Sun sensors on the +X and −X panels must be negative in order to fire the CCW gas jets. In the deployed configuration, a CW yaw error will cause the Sun sensor on the +X panel to be more illuminated than the Sun sensor on the −X panel. Thus, the +X panel sensor resistance is lower than the −X panel sensor resistance. Inspection of Fig. 8 shows this condition will indeed produce a negative output voltage from the bridge circuitry for the yaw photocells.

Now consider the same case with the panels latched. The −X panel sensor is now more illuminated than the +X panel sensor, which produces a net positive voltage from the yaw photo cells to fire the CW jets and rotate the spacecraft farther from the Sun in a CW direction. The spacecraft will continue to rotate CW until the −Z axis is 90 deg from the Sun direction. At this point, a sudden shadowing of the −X panel sensor occurs that causes its resistance to increase, thereby increasing the magnitude and reversing the polarity of the yaw photocell output voltage. The phase reversal causes the CCW jets to fire and rotate the spacecraft back in the direction of the Sun. However, as the 90-deg position is passed, the −X panel sensor is again illuminated (more than the +X panel sensor) and the spacecraft rotates CW. The end result is a stable limit cycle with the −Z axis pointing 90 deg from the Sun direction. In general, the Sun direction in spacecraft cone and clock angle after the stable null is achieved will be:

(1) Sun cone angle equal to 90 deg.

(2) Sun clock angle dependent on initial conditions at separation.

The Sun acquisition behavior described above will occur after any imparted spacecraft tip-off rates have been reduced. It should be noted that the effects of reflected light from the spacecraft structure are neglected in the above discussion. During the initial reduction of tip-off rates, the gyro rate error signals will dominate. If the Sun direction is in the dark region around the spacecraft +Z axis after the removal of tip-off rates, the spacecraft will drift at the rate deadband limits until one or more sensors is illuminated. At this time, the acquisition behavior described above will begin. The position of the Sun in spacecraft clock angle will depend on the initial spacecraft position at separation relative to the Sun and the imparted tip-off rates. With the Sun direction located at a spacecraft cone angle of 90 deg, the spacecraft clock angle position of the Sun will be directly influenced by spacecraft roll position behavior. The spacecraft roll axis during this time is under gyro rate control. After tip-off rates have been reduced, spacecraft roll position will drift slowly at the roll deadband rate until after the panels are deployed and the Canopus acquisition sequence is initiated.

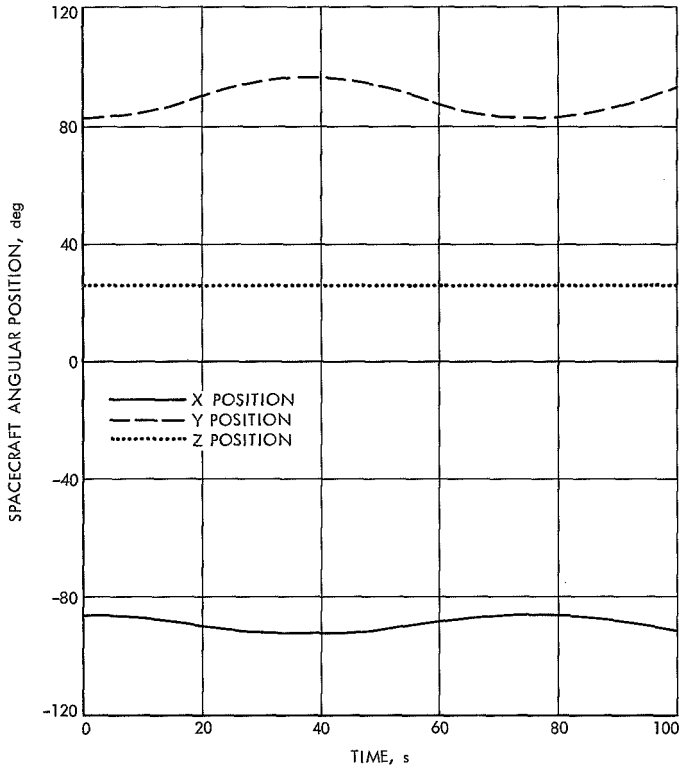

Fig. 9. Spacecraft angular position vs time

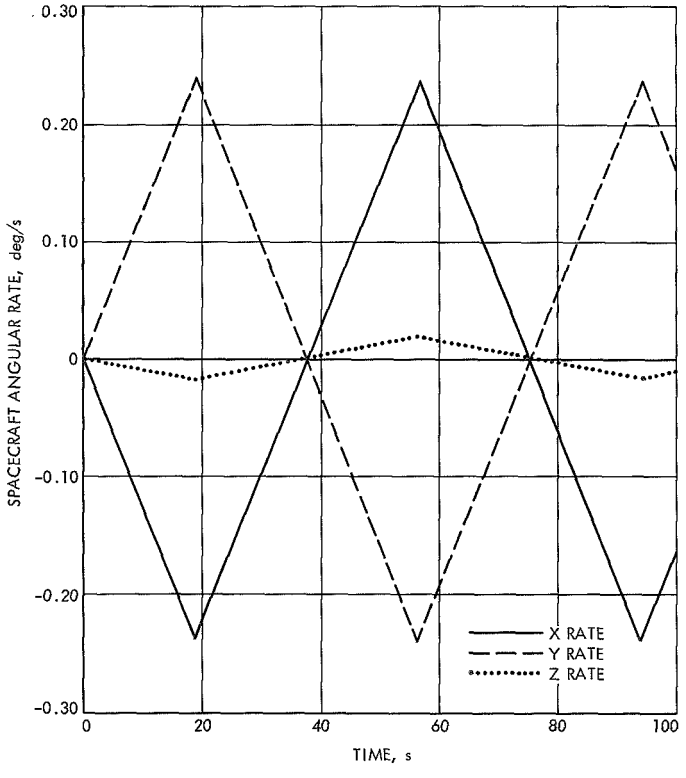

Fig. 10. Spacecraft angular rate vs time

c. Computer simulation. The foregoing description of spacecraft attitude control performance was verified by a three-axis digital computer simulation. The computer program was written in CSSL for the Univac 1108 computer. (This simulation language was recently developed under the NASA OART Program No. 125-17-15-10.)

Figures 9–12 show some typical results of the simulation. These figures depict the following case:

(1) Initial Sun cone angle = 87 deg.

(2) Initial Sun clock angle = 251 deg.

The initial position of the Sun in spacecraft cone and clock angle is considered to be the orientation of the spacecraft relative to the Sun after reduction of tip-off rates. A cone angle near 90 deg was chosen to show the limit cycle behavior within a reasonable computer run time. These initial cone and clock angle positions of the Sun after initial rate reduction correspond to the following initial attitude errors:

(1) $\theta_{xi} = -87$ deg.

(2) $\theta_{yi} = 83$ deg.

(3) $\theta_{zi} = 26$ deg.

(4) $\dot{\theta}_{xi} = \dot{\theta}_{yi} = \dot{\theta}_{zi} = 0$.

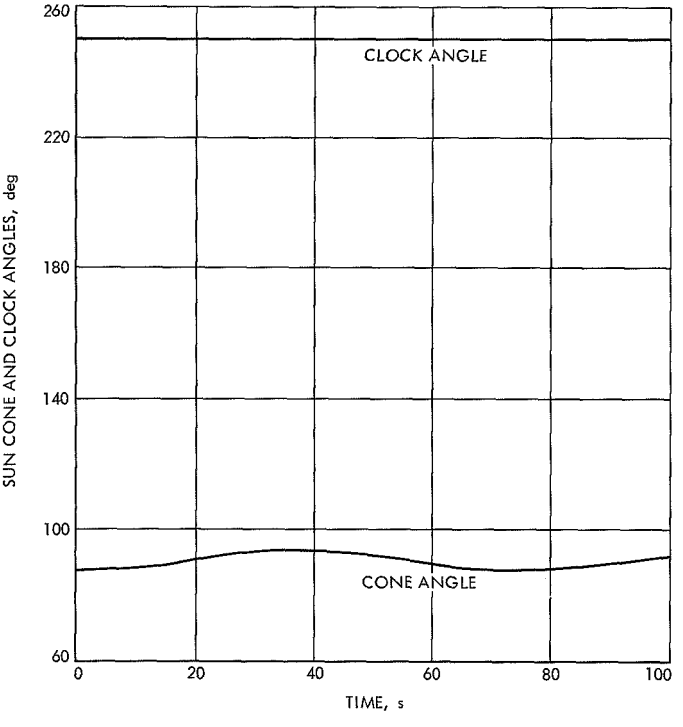

Fig. 11. Sun cone and clock angles in spacecraft coordinates

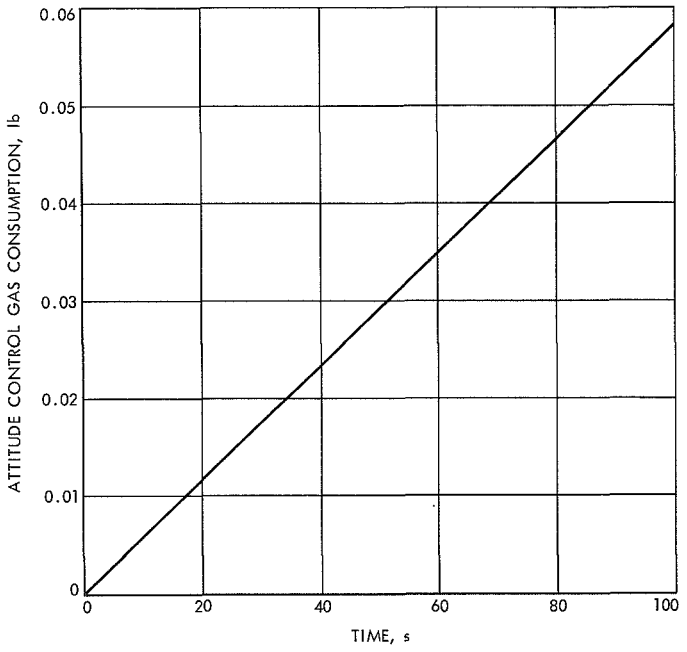

Fig. 12. Attitude control gas consumption vs time

The unknown effects of reflected light from the spacecraft structure on the sensors is not considered.

Figure 9 shows a plot of spacecraft pitch, yaw, and roll position vs time for a period of 100 s. This plot clearly shows pitch and yaw position initially moving away from the Sun and beginning to limit cycle around 90 deg from the Sun line Roll position essentially remains constant over this period of time.

The pitch and yaw limit cycle behavior in angular rate is shown in Fig. 10. Similar limit cycle behavior to that shown in spacecraft pitch and yaw attitude is seen in the Sun cone angle position shown in Fig. 11. Sun clock angle, like spacecraft roll position, remains essentially constant. Referring again to Fig. 9, it can be seen that the amplitudes of the pitch and yaw limit cycles are very large. For this particular case, the peak-to-peak amplitude is 6 deg in pitch and 12 deg in yaw. The limit cycle amplitude will, in general, depend on the spacecraft orientation after reduction of tip-off rates. If the Sun sensors are lit after reduction of tip-off rates, the spacecraft will begin to rotate the −Z axis away from the Sun until the shadow condition at 90 deg is reached. The spacecraft angular rate at the first cross-over of this shadow line will determine the limit cycle amplitude. This is the case depicted in Figs. 9–12. If the Sun sensors are pointing away from the Sun after reduction of tip-off rates, the spacecraft will rotate at the attitude control rate deadband limits until one or more sensors are lit. The attitude control will then rotate the −Z axis toward the Sun until the 90-deg shadow line is reached.

The dependence of limit cycle amplitude on angular rate at first cross-over is due to an apparent discontinuity in the combined Sun sensor characteristic when the shadow line is pointed at the Sun. With the Sun in the vicinity of the shadow line, the Sun sensor output voltage is approximately −3 V for Sun cone angles less than 90 deg and +3 V for angles greater than 90 deg. There is an abrupt change of 6 V as the shadow line is crossed due to the large change in photocell resistance that occurs as the sensors become shadowed. The large voltage change that occurs at each cross-over causes the pitch and yaw gas valves to be continuously on during the limit cycle. Since no rate damping can be provided by the gyros under this condition, peak limit cycle excursion will depend on the initial angular rate at first cross-over of the shadow line (after any large tip-off rates are removed). Attitude control gas consumption for the case discussed is given in Fig. 12, which shows gas consumption increasing linearly with time. This corresponds to continuously on pitch and yaw gas valves. The rate of gas consumption is 0.000585 lb/s. If this condition persisted for the 3 min between separation and panel deployment, 0.1 lb of gas would be consumed.

d. Conclusion. The results of the analysis and computer simulation show that a normal Sun acquisition with the spacecraft −Z axis pointed at the Sun cannot occur when the solar panels are in their latched configuration. The orientation of the Sun sensors relative to the spacecraft when the spacecraft −Z axis is in the vicinity of the Sun line causes a reversal in polarity of the Sun sensor error signal. This produces an unstable null around the normally acquired spacecraft orientation relative to the Sun. A stable limit cycle condition was found to exist when the spacecraft −Z axis is oriented 90 deg from the Sun line (Sun cone angle = 90 deg). This stable null condition is produced by the shadowing effects of the spacecraft structure on the Sun sensors in this orientation.

The following conclusions are drawn regarding this non-standard mode of operation:

(1) The only adverse effect produced on the attitude control subsystem is the high-rate attitude control gas consumption. This is caused by the hard-on gas valve condition created by the unusual limit cycle behavior around the stable null. If, for some

reason, solar panel deployment did not occur at 3 min after separation, approximately 45 min would elapse before the back-up command was sent by the central computer and sequencer. This could result in as much as 1.6 lb of attitude control gas consumption. Since very little margin exists in the initial attitude control gas storage weight, any non-standard mode of operation that can cause large expenditures of attitude control gas should be avoided.

(2) A potentially dangerous situation exists with regard to pointing the TV camera at the Sun. The cone and clock angle in spacecraft coordinates of the instruments in their stowed position are 96 and 237.38 deg, respectively. The location of the Sun at the stable null can be at any clock angle and a cone angle of 90 deg.

(3) The effects of reflected light from the spacecraft structure are unknown and were therefore not considered. Reflected light on the Sun sensors can produce spurious output signals that can alter the predicted off-Sun-line null behavior and/or possibly introduce additional acquisition nulls.

4. Gimbal Actuator

a. Introduction. The *Mariner* Mars 1971 spacecraft is controlled in its midcourse maneuver, and later into orbit about Mars, by an autopilot system using a 300-lbf gimbaled bipropellant rocket engine powered by hypergolic fuels. Orientation about the two axes of the gimbaled engine is controlled by an electromechanical linear actuator (Fig. 13) capable of pointing the engine ± deg about each axis. (The third axis control is provided by the attitude control system's cold gas reaction jets on the ends of the solar panels; these jets exert millipound force.) Two gimbaled actuators are required, one for each axis. Since the functional requirements for the actuators are identical, it was possible to design one actuator to be interchangeable on either axis.

b. Design requirements. The actuator was designed to meet the following performance requirements:

(1) Motor voltage from 0 to 30 Vdc.

(2) Motor current limited to 1.75 A.

(3) Stroke, fully retracted to fully extended, 0.785 ± 0.030 in.

(4) Rate vs load as illustrated in Fig. 14.

(5) Backlash (total), including effects of mounting, limited to 0.004 in. of stroke under a load of at least 5 lb.

(6) Null position within 0.002 in. of actuator's center stroke.

(7) Response time less than 0.100 s.

(8) Operating life 50,000 h (continuous).

c. Description. The gimbal actuators provide a controlled linear motion in order to point the gimbaled engine in response to the command of the autopilot system. The actuator is a very simple device (Fig. 13) consisting of only three major parts contained in a pressurized, O-ring-sealed housing. The three major parts are:

(1) A linear motion transducer.

(2) A recirculating ball lead screw assembly.

(3) A direct current drive motor.

These parts and the housing are described below.

Linear motion transducer. The linear motion transducer is a linear, variable differential transformer excited by 6000 Hz sine waves at 17 Vrms. The demodulated transducer scale factor is 3.2 Vdc/in. of linear movement. Average power required is only 0.2 W. A unique feature of the recirculating ball lead screw assembly is that the shaft of the assembly is bored out to provide an installation position for the linear motion transducer, which can be placed concentrically in the actuator. This arrangement allowed for a very compact design.

Recirculating ball lead screw assembly. The ball screw assembly consists of a screw and mating nut, each having a specially formed concave helicoid ball groove. The nut, perfectly mated over the screw, contains the balls filling one or more circuits that serve as the engagement medium between the nut and screw. Three ball circuits are used in the gimbal actuator, each containing about 35 balls. The pitch of the screw is 1/10 in. per turn, with a ball circuit diameter of 5/8 in.

The ball screw assembly uses 1/16-in.-diam balls. Transfer inserts spaced symmetrically around the nut circumference form a cross-over path guiding the balls from the end of the turn to the start of the same turn. This arrangement provides a continuous recirculation or closed circuit of balls, which prevents the balls in a particular circuit from entering any other race within the nut.

(a) ASSEMBLED ACTUATOR

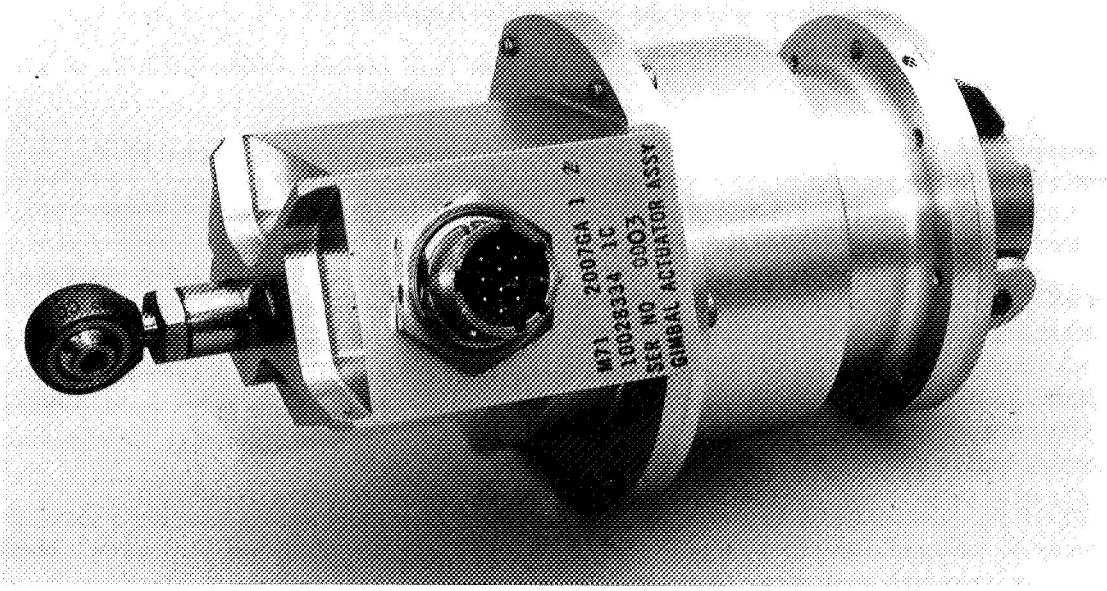

(b) CUTAWAY VIEW

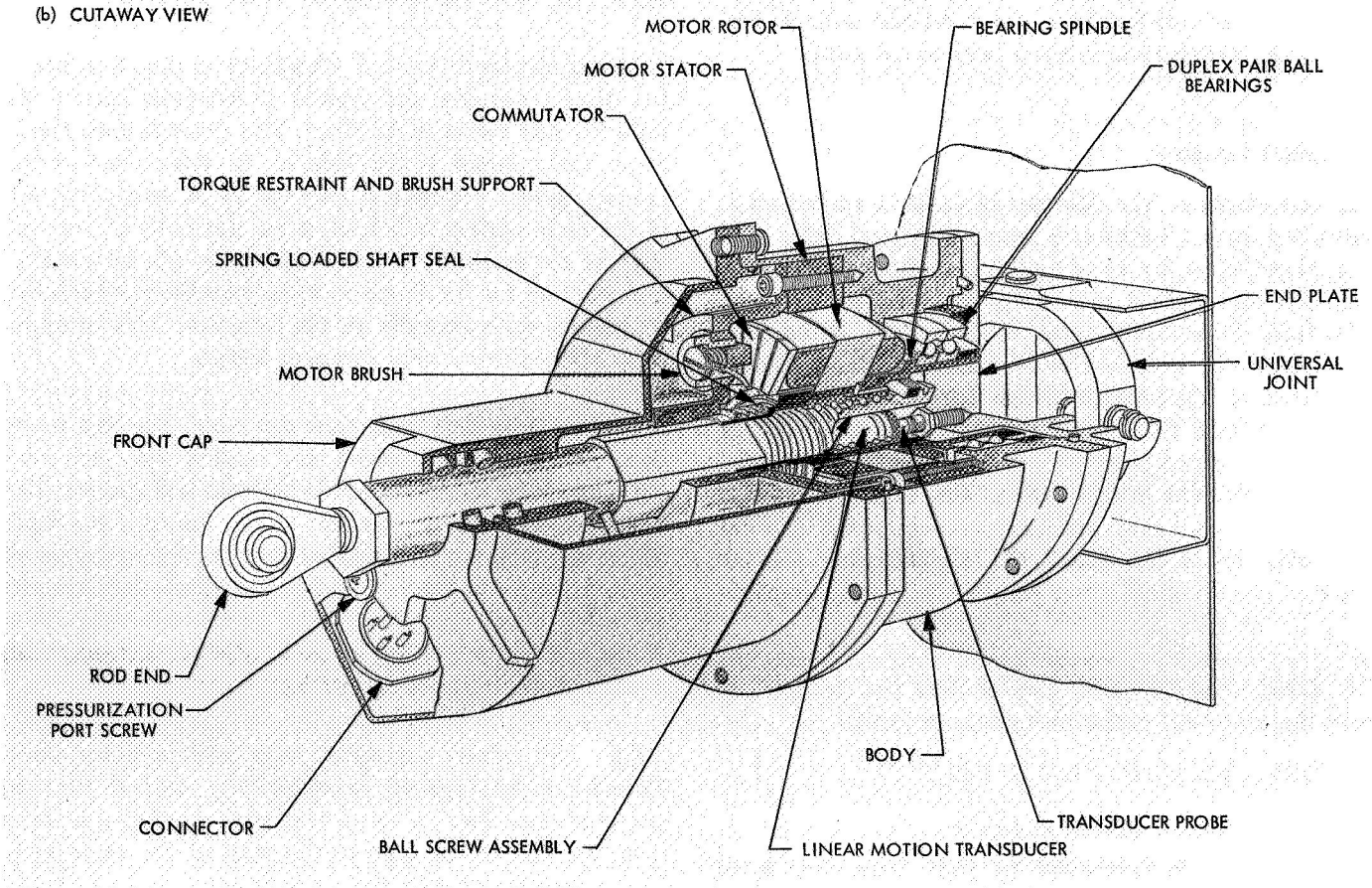

Fig. 13. *Mariner* Mars 1971 gimbal actuator assembly

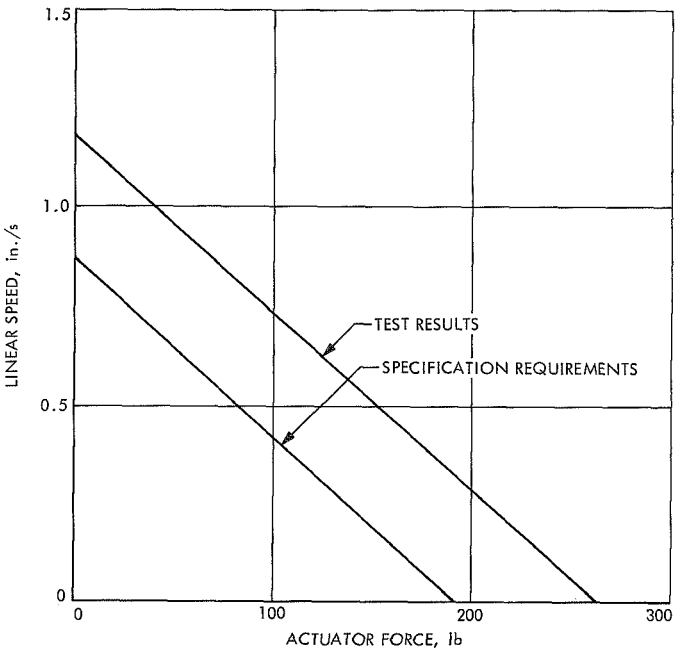

Fig. 14. Gimbal actuator load speed performance

The use of internal transfer inserts is one of the unique features of this ball screw assembly. Because the inserts eliminate external projection, the ball-nut assembly is ideally suited to be assembled inside the bearing spindle, which also supports the motor armature.

Because each circuit is only one complete turn of balls, the number of balls being recirculated is limited. This reduces the effect of friction produced by adjacent balls skidding on each other and eliminates the use of spacer balls entirely. The rotation of the shaft pushes the balls (never exceeding two or three at a time) through the transfer.

The ball track, which is similar to a ball-bearing groove, has a ball-diameter-to-groove-radius conformity of 56%. The initial contact angle is set up within 35 to 45 deg. The contact angle change under load is not drastic; therefore, it permits higher loads to be carried without fear of the contact elipse overlapping the shaft radius.

The load-carrying static capacity of the ball screw assembly in the gimbal actuator is 550 lb per circuit. With three circuits, this provides a static capacity of 1650 lb. The mechanical efficiency of the ball lead screw assembly is 94%. Under ideal conditions of configuration and loading, this value can be a point or two higher. The material selected for the recirculating ball lead screw assembly was AISI 440C stainless steel. This high-chromium stainless steel can be hardened to higher values than any of the other stainless steels. In the hardened condition, it has full corrosion and wear resistance.

The efficiency of the ball lead screw is a function of the screw lead angle. A comparison between the efficiency of a ball lead screw and that of an Acme screw (Ref. 1) is shown in Fig. 15.

Direct current drive motor. The motor in the actuator is of the reversible dc type, which was chosen in preference to an ac type because of packaging and power efficiency for the required output torque. The current requirement is in an approximately linear relationship to the load.

The rotor for this motor is wound in an eight-pole configuration. A permanent magnet stator is placed outside the rotor (Fig. 13). The rotor is wound with a 20-Ω resistance. The commutator is placed axially on the shaft. The motor has a top speed of 700 rev/min and a linear torque speed characteristic with a stall torque value of 70 oz-in.

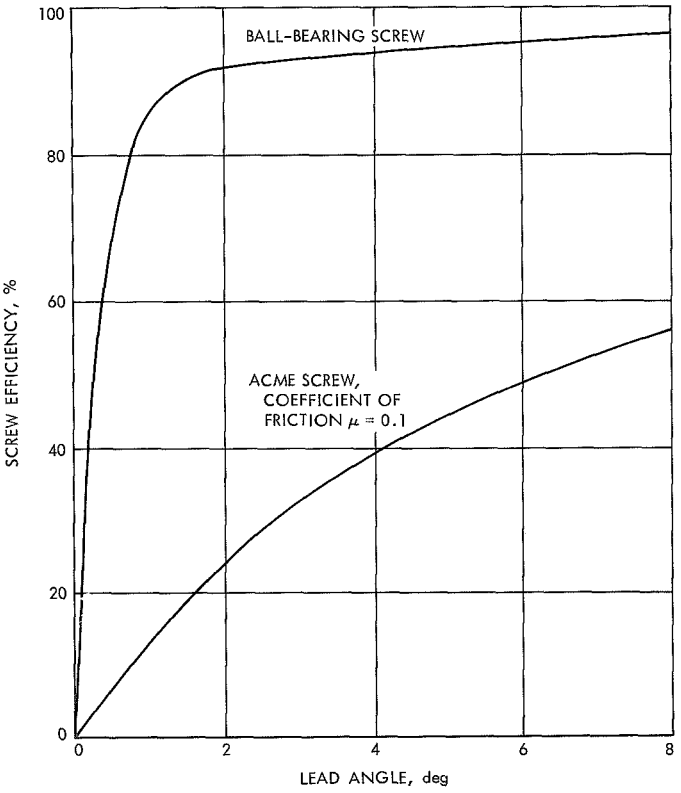

Fig. 15. Comparison of ball lead screw and Acme screw efficiency

The motor current demand is linear from a minimum value required for no-load operation to a maximum value of 1.5 A at stall. The actuator has a 0.015-s time constant, which can be attributed to the configuration of the drive motor with its unusually large-diameter air gap.

Actuator housing. The actuator housing was designed in three parts: the front cap, the actuator body, and the end cap. The base of the end cap is supported by a universal joint providing two-axis freedom of actuator mounting. The actuator is sealed by five O-rings: three in static-seal configuration; with one at the end position, one sealing the body to the front cap, and one under the connector plug; and two carefully selected O-rings that provide the dynamic seal around the output shaft.

The actuator is filled with a mixture by volume of 90% nitrogen and 10% helium at 5 psig; the allowable leak rate is in the molecular flow regime. The helium in the gas mixture inside the actuator provides a helium trace that enables the use of a mass spectrometer leak detector to measure the leak rate. This helium leak rate is modified by a conversion constant in order to obtain the mixture leak rate. For the gimbal actuator, this mixture leak rate is specified to be 0.07 standard cm^3/h. Figure 16 shows the exponential decay of pressure from the actuator as a function of time in deep space at the maximum allowable leak rate. The gas pressurization of the actuator protects the brushes and bearings and allows it to be lubricated by a conventional lubricant (General Electric Silicon GS300).

d. Testing and Performance. All components of the actuator are chosen so that they are capable of withstanding temperatures of 450°F, with the exception of the arc suppression capacitors, which will withstand only 400°F. Accordingly, the actuator is readily heat sterilizable. The actuator high-temperature test requirement is 315°F.

The axial arrangement of the brushes with respect to the commutator simplifies assembly, as the brushes can be installed from the front. Even with brush commutation, it is expected that the useful operating life of the device will be more than 50,000 h.

The electrical efficiency of the actuator is shown in Fig. 17, and the load speed performance is shown in Fig. 14.

The actuator was life-tested by having it drive a 30-lb load at 90% of full amplitude through 120,000 cycles (equivalent to 100,000 h operation). The brush wear after the life test was 0.015 in., about 6% of the brushes' active length. No measurable degradation was observed in any other parts of the actuator.

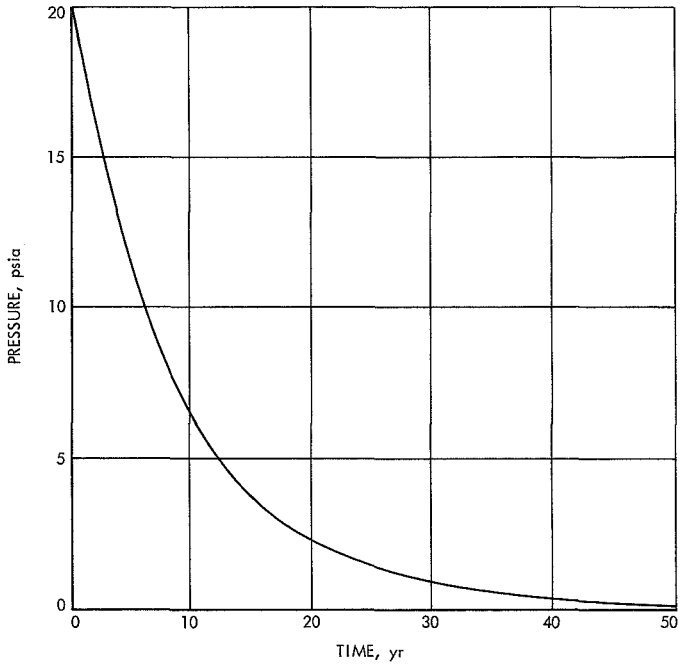

Fig. 16. Molecular regime leak rate

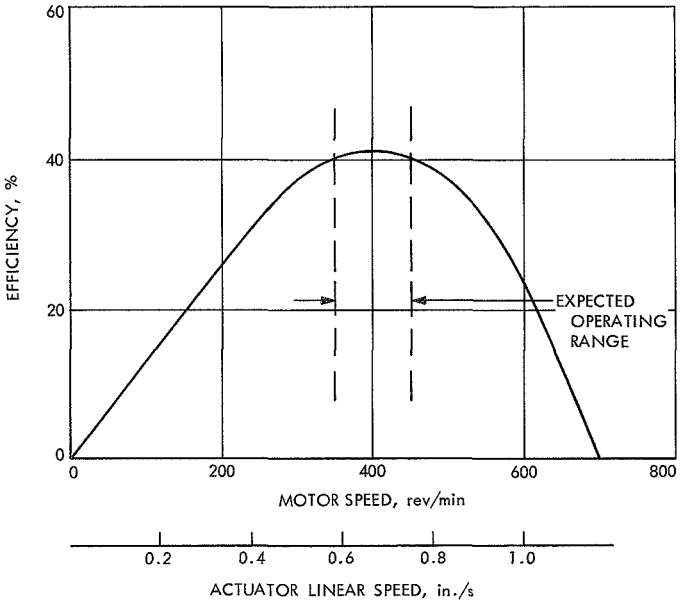

Fig. 17. Gimbal actuator electrical efficiency

Table 3. Actuator performance

Parameter	Value
Time constant, s	0.015
Stall force, lb	285
Stall current, A	1.5
Voltage, Vdc	0–30
Weight, lb	2.75

The actuator has been successfully qualified to special *Mariner* Mars 1971 environmental requirements. The unit was heat cycled 12 times, during a 2-wk period, in a vacuum environment (10^{-6} torr) from +167 to +315°F after being cooled to −22°F for 24 h. Vibration testing, at levels of 9 g, was conducted using both random noise and a sine sweep from 0 to 2000 Hz. The actuator was in operation and performed well during the vibration test; no resonant disturbances were observed. Performance parameters are shown in Table 3. These values are actual test measurements recorded during bench testing of the actuators.

Reference

1. Phelan, R. M., *Fundamentals of Mechanical Design,* Second Edition, p. 195, McGraw-Hill Book Co., Inc., New York, 1962.

5. Reaction Control Assembly

The reaction control assembly (RCA) provides the actuating torques required to provide spacecraft attitude control. Each *Mariner*-series spacecraft carries two identical half gas systems consisting basically of a high-pressure storage vessel, a pressure-reducing regulator, a low-pressure distribution system and six jet valve-nozzle assemblies.

The required actuating torque is produced by exhausting controlled amounts of nitrogen gas through two jet valve-nozzle assemblies on either side of the spacecraft (one from each half system) mounted on the tips of the solar panels. Each set of four jet valves provides control about each of the X, Y, and Z axes and are labeled as the pitch, yaw and roll valves, respectively (i.e., two jet valves for plus pitch rotation and two for negative pitch). Command excitation to the valves of 28 Vdc is provided by the attitude control electronics (ACE) in either the form of 20-ms pulses (e.g., limit cycle operation) or continuous excitation (e.g., commanded turn and initial acquisition modes).

The *Mariner* Mars 1971 design is nearly identical to the *Mariner* Mars 1969 RCA design described in a forthcoming JPL technical report.[4] The design philosophy underlying the entire *Mariner* Mars 1971 spacecraft design cycle was to utilize the existing *Mariner* Mars 1969 residual hardware to the maximum extent possible within the constraints imposed by the more stringent *Mariner* Mars 1971 mission requirements. The *Mariner* Mars 1971 design utilizes nearly all of *Mariner* Mars 1969 hardware, which has held procurement of new hardware to an absolute minimum.

The first design study conducted for *Mariner* Mars 1971 was to determine the thrust levels obtainable from the jet valve–flight nozzle combinations. Higher spacecraft inertias, coupled with the anticipated increase in midcourse engine swirl torques, require thrust levels nearly 3.5 times greater than those used prior to the *Mariner* Mars 1969 program. Accordingly, the computer program originally developed during the *Mariner* Mars 1969 build cycle, and utilized for final sizing of the *Mariner* Mars 1969 flight nozzles, was again used to determine the maximum thrust capability of the jet valves. A curve of these results is shown plotted in Fig. 18. Also plotted are test data obtained from actual jet valve–nozzle combinations mounted on a cantilever beam (the technique for obtaining thrust measurement in this manner is described in SPS 37-44, Vol. IV, pp. 41–42). The test results show good correlations with the computer data, and the ability of the valves to meet the 0.017-lbf requirement is demonstrated (0.017 lbf is required in the roll axis to provide 2 in.-lb of torque per gas system to counteract midcourse engine swirl torques).

An additional concern pertaining to the jet valves was their ability to perform during the extended mission environments where solar-panel temperatures in the range of −200°F to −300°F are anticipated (this occurs approximately 90 days after the Mars orbit insertion when the spacecraft goes into solar occultation). A test to prove the jet valve's ability to perform in this low temperature environment was conducted on two jet valves installed on a pitch manifold and placed in a thermal chamber maintained at −300°F. Functional tests were performed while maintaining the −300°F temperature. Satisfactory performance assured the compatibility of the valves with this environment extreme.

[4] *Mariner Mars 1969 Project Final Report: Volume I,* Technical Report 32-1460. Jet Propulsion Laboratory, Pasadena, Calif. (to be published).

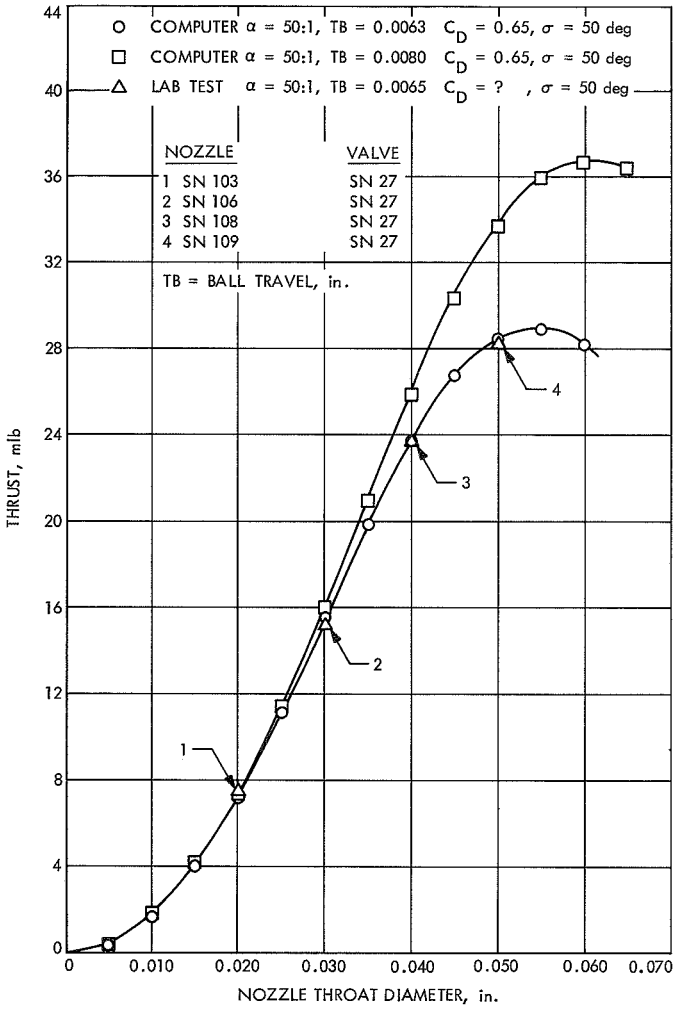

Fig. 18. Jet valve maximum thrust capability

Another problem that was resolved was storage of the additional gaseous nitrogen propellant needed to meet the *Mariner* Mars 1971 higher thrust levels and longer mission life. A fracture mechanics study conducted on the TI-6AL-4V titanium pressure vessels over the past few years had recently been completed and the published results enabled the man-rated safety factor associated with these vessels to be reduced from 2.2:1 down to 2.0:1. This permitted the storage pressure to be increased from 2560 psig (*Mariner* Mars 1969 flight pressure) up to 2740 psig, thereby increasing the stored mass of gas from 2.50 lbs to 2.70 lbs, respectively.

As a consequence of the above design studies, it was determined that all RCA component designs flown on the *Mariner* Mars 1969 Program were reusable on the *Mariner* Mars 1971 Mission. With this baseline established, the remainder of the design effort was to perform layout studies in order to achieve a compatible interface with the bus structure.

The basic "strap-on" RCA design used for *Mariner* Mars 1969, and previous *Mariners*, has been retained in the *Mariner* Mars 1971 design. The primary design difference occurs in the rerouting of three segments of low-pressure tubing that distribute the nitrogen gas from the pressure regulator outlet to each solar panel hinge point. The two enlarged fuel tanks required by the midcourse propulsion system were the main reason for this redesign. The effect on the RCA was twofold: First, the solar panel outriggers added to the basic spacecraft bus structure to enable rotation of the solar panels into a stowed position around the enlarged propulsion tank volume required additional low-pressure distribution tubing out to the new hinge points. Secondly, the position of the high-pressure portion of the gas system assembly on the top surface of the octagon bus structure had to be relocated to a new position compatible with these tanks.

A bracket and clamp arrangement has been added to the high-pressure vessel support ring to provide added support to the base of the pressure transducer. This was done because the high "Q" associated with the *Mariner* Mars 1969 cantilever mounting produced *g* loads exceeding the manufacturer's specified levels. Although this condition produced no degradation of performance with respect to the *Mariner* Mars 1969 transducers, this opportunity was taken to rectify the design.

Due to the restricted field of view presented by the enlarged propulsion fuel tanks, the acquisition sun sensors have been moved from their previous position on the bus to a new location outboard of the jet valves on the solar panels. A mounting bracket arrangement has been provided on the manifolds to accommodate the sun sensors and the necessary cabling for the sensors has been incorporated into the RCA wiring harness. This is not the first time a unit has been supported piggyback on the jet valve manifolds; the solar vane actuators were mounted in this position during the *Mariner* Mars 1964 Mission.

The wiring harness, although basically the same as the *Mariner* Mars 1969 design, now incorporates a single ground return for each pair of jet valves as opposed to a common ground for all six valves as on previous systems. This permits a splice within the harness to be eliminated resulting in a higher reliability rating for the jet valve harness assembly.

Although not part of the flight equipment, the fill manifold remains an integral part of the RCA until its removal just prior to launch. The function of the fill manifold is to provide filter protection to the RCA system during charging operations associated with the build cycle and subsequent testing operations. The shutoff valve incorporated into this fill manifold functions as a "valve saver" for the flight shutoff valve located in the flight manifold.

A new design for this fill manifold was generated to eliminate problems encountered on previous programs with leaking shutoff valves and checkvalve anomalies. The new design incorporates a soft-seat shutoff valve in place of the hard-seat ball valve and a bidirectional filter element. Use of a bidirectional filter permits the check valve to be removed, thereby eliminating a problem area.

D. Astrionics

1. Flight Telemetry Subsystem

a. Introduction. This article discusses the *Mariner* Mars 1971 flight telemetry subsystem (FTS) design requirements and the mechanization implemented to meet them. The article contains actual subsystem implementation and performance information rather than purely analytical data.

b. Functional Description

Subsystem description. The *Mariner* Mars 1971 FTS (Fig. 19) performs the data conditioning, multiplexing, encoding, and modulation of spacecraft engineering parameters. In addition, the FTS performs modulation and block coding of science data for transmission to Earth. It does not perform radio transmission functions, scientific instrument data conditioning, or data storage functions. Eighty-two analog inputs are accepted, digitized, and multiplexed with 12 digital inputs for transmission via the engineering data channel. Data rate, data mode, and modulation index switching is provided.

A total of three data channels are provided: one for science data (channel A), one for engineering data (channel B), and one for high-rate (block coded) data (channel C). The three channels provided accomplish the following:

(1) *Channel A:*

(a) Accepts serial, digital science data at 50 bits/s for real-time transmission to Earth.

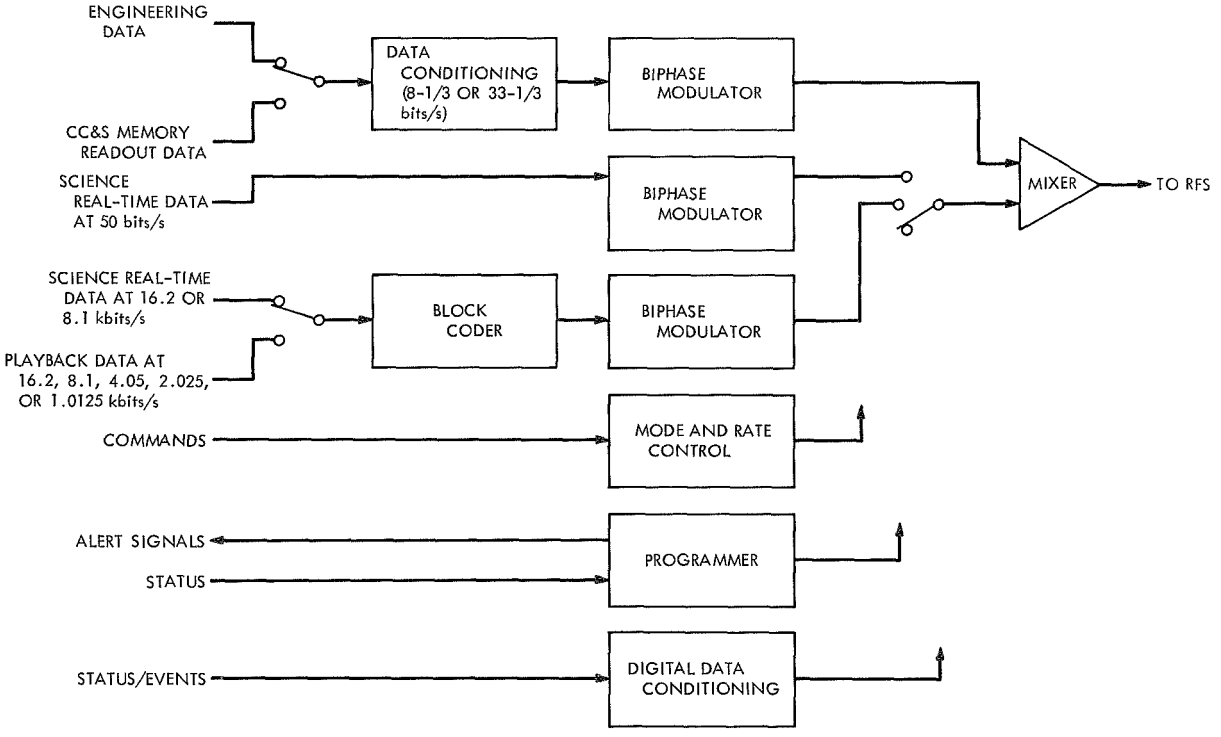

Fig. 19. FTS simplified block diagram

(b) Biphase modulates the science data with the subcarrier for this channel.

(2) *Channel B:*

(a) Accepts analog and digital measurement data from the spacecraft for transmission to Earth at 33⅓ or 8⅓ bits/s.

(b) Accepts and keeps an accumulative count of event pulses from the spacecraft.

(c) Conditions and encodes the engineering data into a 7-bit non-return-to-zero (NRZ) word format.

(d) Inserts a unique code into the data to provide frame synchronization.

(e) Inserts an index word that will identify subcommutation words during each cycle of high-rate commutation and will identify the initiation of central computer and sequencer (CC&S) memory readout.

(f) Biphase modulates the engineering data with the subcarrier for this channel.

(3) *Channel C:*

(a) Accepts serial digital data from either the science subsystem at 16.2 or 8.1 kbits/s or data storage subsystem at 16.2, 8.1, 4.05, 2.025, or 1.0125 kbits/s for block coding and subsequent transmission to Earth.

(b) Biphase modulates the block coded data with the subcarrier for this channel.

Element description. A detailed block diagram of the FTS is shown in Fig. 20. The detailed requirements of the major physical elements are given in the following listing:

(1) *Commutator.* The commutator format is shown in Fig. 21. The 200 deck commutators are stepped once for each cycle of the 100 deck; the 300 and 400 decks are stepped once for each cycle of the 200 decks.

(2) *Commutator frame synchronization.* To establish frame synchronization, a 15-bit pseudo-noise (PN) code word is provided in the high-speed frame. To aid the ground equipment in establishing decommutation, the 15-bit PN code is followed by a 6-bit index word indicating the position of the subcom deck or the initiation of a CC&S memory readout.

(3) *Digital data conditioner.* The digital engineering data is routed to the engineering data multiplexer via the transfer register. The transfer register accepts data from the following registers:

(a) Frame counter. The frame counter is a 7-bit binary counter that counts each complete engineering telemetry data frame. It accumulates a count of 100 before resetting to one. Its contents are read out in parallel to the transfer register upon a signal from the programmer.

(b) Event register. The event register consists of four 3-stage binary counters that count spacecraft events. Each counter accumulates eight counts and then spills over. The counters are read out in pairs to the transfer register as directed by the programmer. Engineering channel bit rate and data processor identification are also encoded on the event register channels.

(c) Frame synchronization. The frame synchronization logic inserts a 15-bit PN code into the first 15-bit positions of the commutator high-rate frame. The code inserted is as follows:

MSB LSB

000011101100101

Readout is most significant bit (MSB) first.

(d) Index word. A 6-bit index word denoting the states of the subcom channels of the commutator is inserted following the 15-bit PN code. This word has 49 states, 48 to identify the subframes in the engineering data stream and one to identify the initiation of CC&S memory readout.

(e) Event timer. The event timer is a 7-stage binary counter that measures the time duration of a relay closure to ground received from the CC&S subsystem. The count is accumulated by gating a reference frequency of bit sync divided by two. The count is stored in the counter and is read out in parallel to the transfer register upon direction from the programmer.

(f) Status monitor register. The status monitor register is a 7-bit register that contains information on the spacecraft identification, data mode, and RF subsystem status. The first two stages contain the spacecraft identification and the third through fifth stages identify the existing data mode. The sixth stage indicates traveling wave tube power high/low and the seventh stage indicates RF

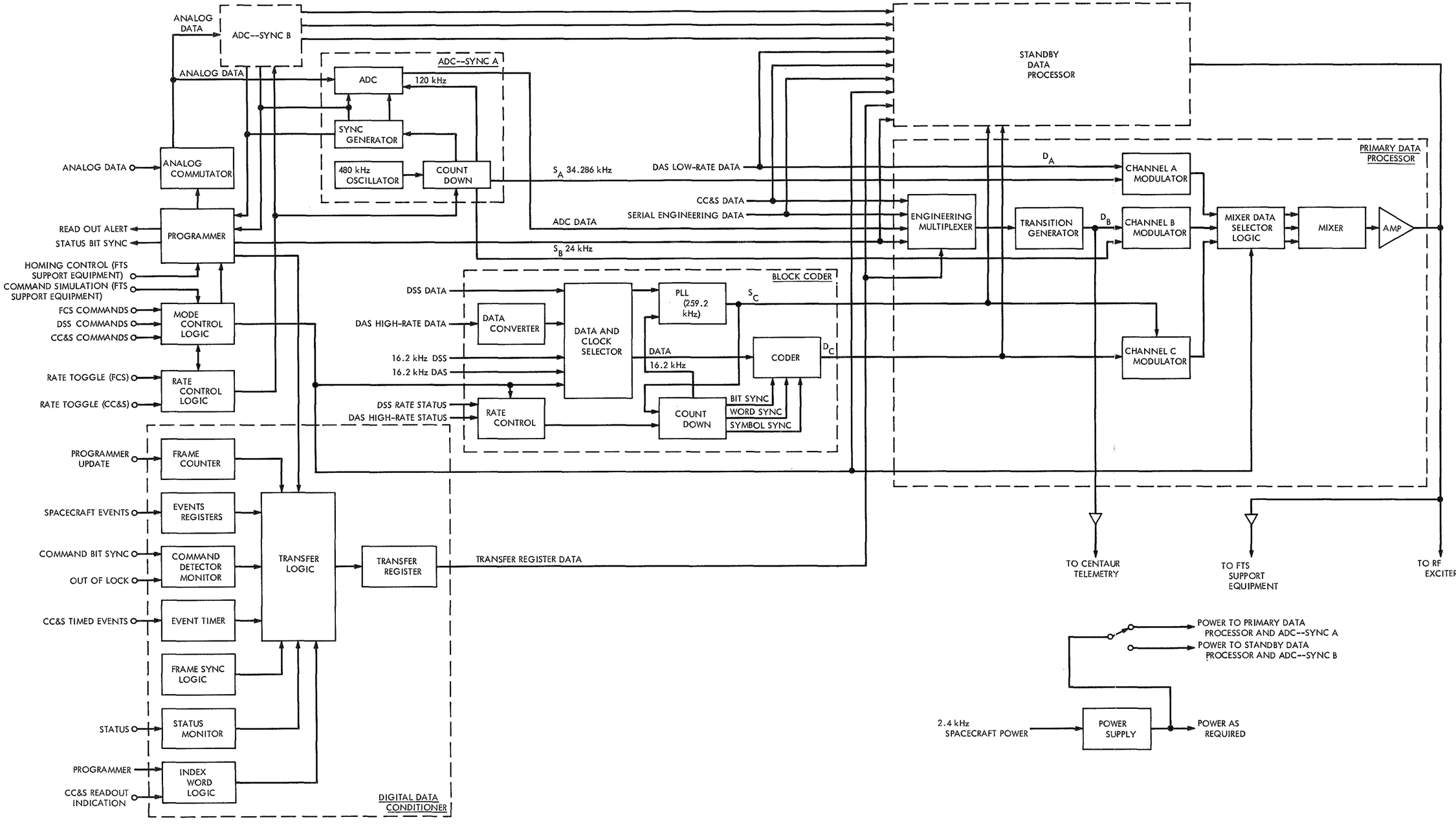

Fig. 20. FTS detailed block diagram

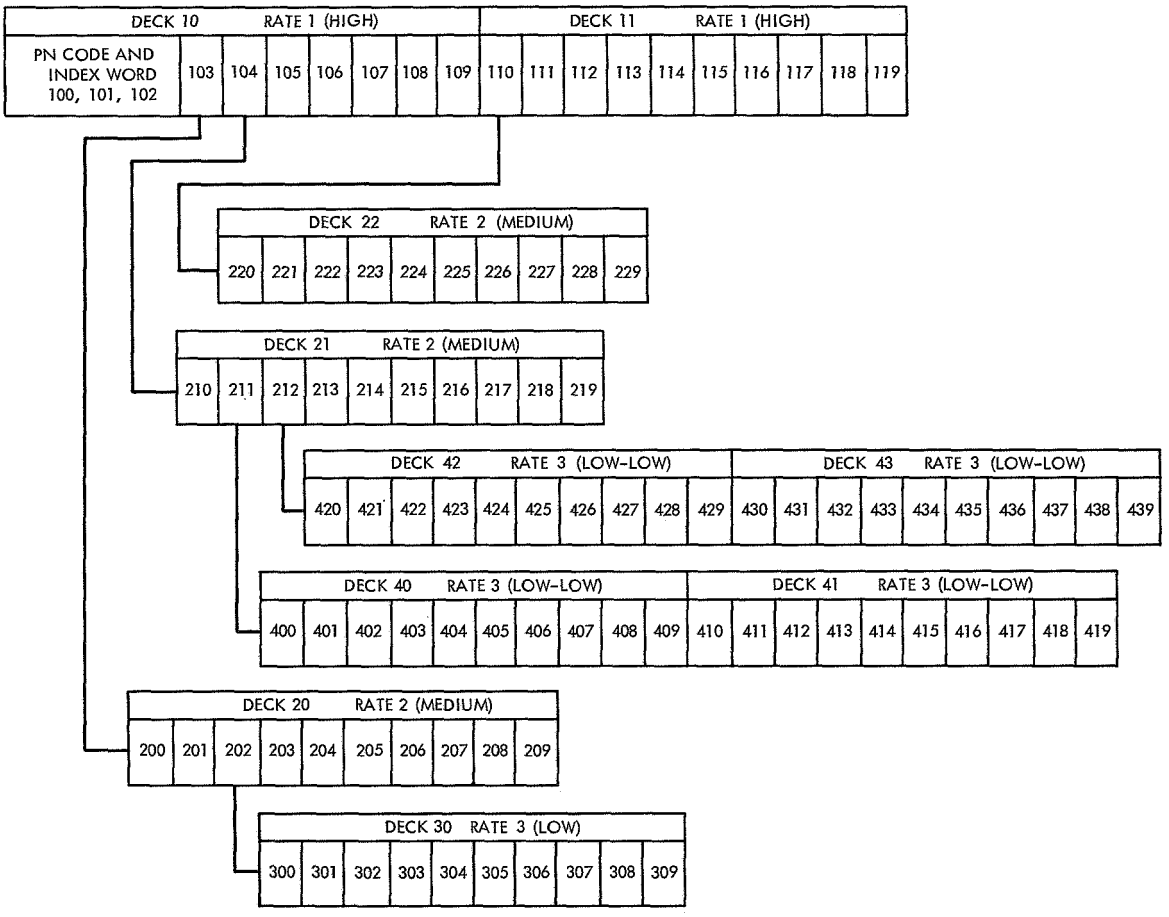

Fig. 21. FTS commutator format

ranging on/off. The contents of the register are transferred in parallel to the transfer register as directed by the programmer.

(g) Command detector monitor. The command detector monitor register is a 5-stage counter that accumulates 12 kHz for one command bit sync interval. One additional stage indicates whether the command detector is in or out of lock. The contents of this register are read out in parallel to the transfer register as directed by the programmer.

(h) Transfer register. The transfer register is a 7-stage shift register. The digital data entry is accomplished in parallel. The readout of the register is in a serial form to the engineering data multiplexer. The gating in and shifting out of data is controlled by the programmer.

(4) *Analog-to-digital converter–sync block.* The analog-to-digital converter (ADC)–sync block converts the analog commutator output to 7-bit NRZ digital words and also provides the basic timing signals for the FTS. The ADC–sync block is redundant and is made up of the following devices:

(a) 480-kHz oscillator. The basic timing source for the FTS is a 480-kHz crystal-controlled oscillator. The oscillator has a frequency stability of $\pm 0.01\%$. The oscillator output drives the ADC–sync countdown circuitry.

(b) Countdown circuitry. The ADC–sync countdown circuitry digitally counts down the 480-kHz oscillator output to obtain the channel A subcarrier, channel B subcarrier, ADC clock, and the sync generator input frequency. The countdown is controlled by the rate and mode of operation. The sync generator clock is that required by the specific mode of operation.

(c) Sync generator. The sync generator generates the required timing signals for the analog-to-digital conversion and the programmer. The generator

generates bit-sync pulses for clocking the information bits. There is 1-bit sync pulse per information bit. The generator also generates one word sync pulse for 7-bit sync pulses.

(d) ADC. The ADC accepts the analog output of the commutator and converts it into 7-bit binary words. The ADC accepts 0 to 3 V levels from the commutator for digitizing and receives timing signals from the sync generator and countdown circuitry.

(5) *Primary/secondary data processor.* The primary data processor consists of the engineering multiplexer, transition generator, channel modulators, mixer data selection logic, and the mixer amplifier. The data processor is redundant and is made up of the following devices:

(a) Engineering multiplexer. The engineering multiplexer switches the various data inputs to the channel B modulator as directed by the programmer. It receives inputs from the ADC, CC&S subsystem, transfer register, and the data storage subsystem (DSS) (serial digital data). The science data selector receives data inputs from the DSS (non-real time) and the data automation subsystem (DAS) (real time).

(b) Transition generator. The transition generator inverts alternate data bits in the engineering data stream. This design circumvents the problem of maintaining synchronization with the data on the ground in the event of a relatively long period of no data, i.e., CC&S memory readout.

(c) Modulators. The modulators (engineering, science, and block coding) perform biphase modulation of each data channel with their respective subcarriers. The engineering modulator modulo-two adds the engineering data D_B with the channel B subcarrier S_B. The result is $D_B \oplus S_B$. The science modulator modulo-two adds the real-time science low rate data D_A with the channel A subcarrier S_A. The resultant output is $D_A \oplus S_A$. The block coding modulator modulo-two adds the block coder output D_C with the channel C subcarrier S_C. The resultant is expressed as $D_C \oplus S_C$.

(d) Mixer data selection logic. The mixer data selection logic is controlled by the mode control logic. It selects the output of the appropriate modulator(s) to comprise the composite signal to the radio frequency subsystem (RFS).

(e) Mixer. The mixer adds channels A, B, and C. The output of the mixer can be expressed as follows:

Data mode	Output
Engineering	$K_1 (D_B \oplus S_B)$
Real-time science I	$K_1 (D_B \oplus S_B) + K_2 (D_A \oplus S_A)$
Playback or real-time science II	$K_3 (D_B \oplus S_B) + K_4 (D_C \oplus S_C)$

where K_1, K_2, K_3, and K_4 are constraints determined by the RF modulation angles.

(6) *Programmer.* The programmer controls the state of the commutator, engineering data multiplexer, and the digital data processor by providing timing and alert signals to generate the correct data format.

(7) *Rate–mode logic.* The data rate and mode logic control the specific engineering data rates and FTS modes. The rate and mode control is accomplished such that upon loss of power, the FTS will maintain the state commanded prior to power loss. The telemetry modes of operation and available data rates are shown in Table 4.

(8) *Power supply.* The power supply provides all voltages necessary for FTS operation. The power supply operates from the 2400-Hz spacecraft power.

(9) *Block coder.* The block coder converts each 6 bits of DAS or DSS serial data into a 32-bit biorthogonal comma-free code. The resultant data stream is transmitted at (32/6 × input bit rate) symbols per second. The block coder is made up of the following devices (Fig. 22):

(a) Input selector and data conditioner. The input selector and data conditioner selects inputs from DAS or DSS, depending upon the FTS mode of operation, and is controlled by the mode control logic. It also converts the DAS pulse return-to-zero (RZ) data into NRZ form for use by the coder logic. Inputs from DAS or DSS consist of data, rate indication to control the FTS block coder data rate, and a 16.2-kHz reference frequency for synchronization.

(b) Phase-locked loop. The phase-locked loop (PLL) derives a 259.2-kHz squarewave from the 16.2-kHz reference received from the DAS or DSS. The

Table 4. Telemetry modes and data rates

Subcarrier frequency	Channel A (34.286 kHz)		Channel B (24.000 kHz)		Channel C (259.2 kHz)	
Mode	Data	Data rate, bits/s	Data	Data rate, bits/s	Data	Data rate, kbits/s
Engineering	—	—	Engineering[a] (CC&S)[b]	8⅓ 33⅓	—	—
Real-time science I	Real-time science	50	Engineering[a] (CC&S)[b]	8⅓ 33⅓	—	—
Real-time science II	—	—	Engineering[a] (CC&S)[b]	8⅓ 33⅓	DAS high rate	16.2 8.1
Playback	—	—	Engineering[a] (CC&S)[b]	8⅓ 33⅓	DSS	16.2 8.1 4.05 2.025 1.0125

[a]The launch mode will be engineering data at 33⅓ bits/s.

[b]Submode = CC&S memory readout; CC&S data substituted for engineering data at the existing data rate.

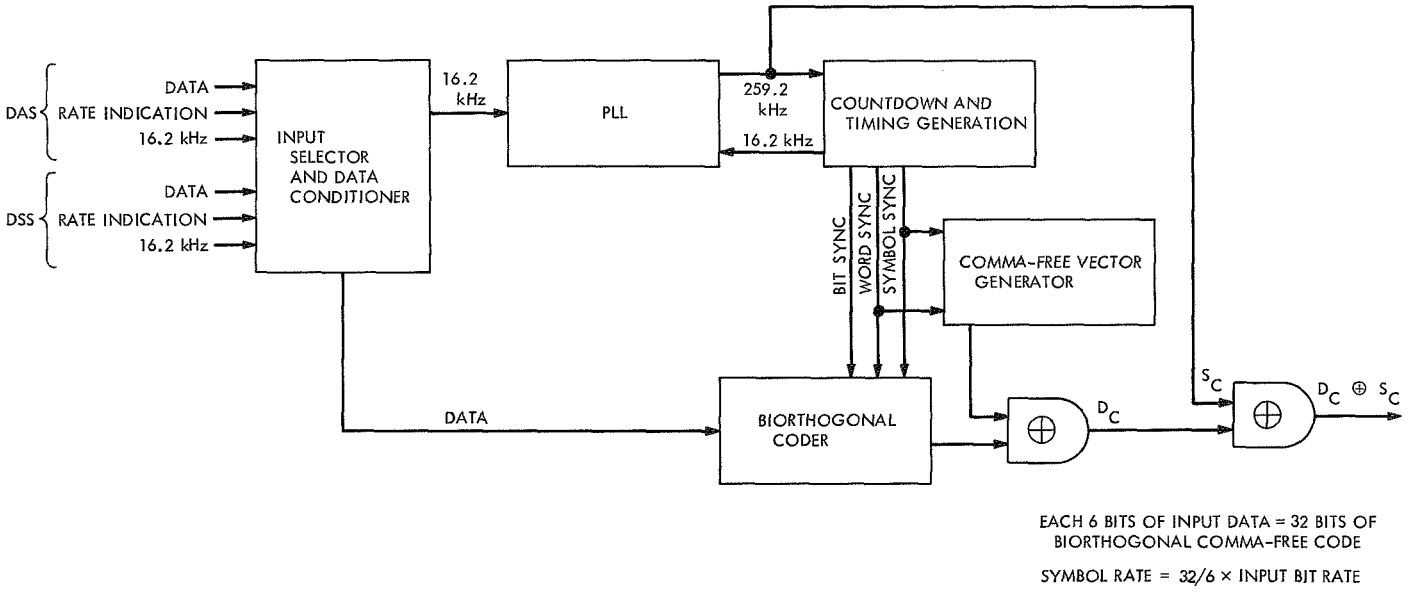

Fig. 22. FTS block coder block diagram

259.2-kHz signal is phase coherent with the 16.2-kHz reference signal. The PLL has a loop bandwidth of 100 Hz and a frequency stability of ±0.01%. The 259.2-kHz signal is used for the channel C subcarrier.

(c) Countdown. From the PLL, the countdown circuitry derives the necessary bit sync, word sync, and symbol sync required by the coder.

(d) Biorthogonal coder. The biorthogonal coder converts each 6 bits of input data into a 32-symbol biorthogonal code. The symbol rate is (32/6) × input data bit rate.

(e) Comma-free vector generator. The comma-free vector generator consists of a 5-stage PN generator, the output of which is a 32-bit PN code. The biorthogonal comma-free code is obtained through

biphase modulation of the biorthogonal code by the output of the comma-free vector generator. The resultant output is then biphase modulated by the channel C subcarrier (259.2 kHz).

c. Implementation. The *Mariner* Mars 1971 FTS is a modification of the *Mariner* Mars 1969 FTS design. Flight equipment supplied for the *Mariner* Mars 1971 Program include one flight-spare FTS [modified *Mariner* Mars 1969 proof-test model (PTM) FTS], one flight FTS (modified *Mariner* Mars 1969 flight-spare FTS), and one flight FTS (new build).

Mariner Mars 1969 FTS modifications. Functional design studies were performed in 1968 in order to improve the *Mariner* Mars 1969 FTS design with respect to better data handling capabilities and new spacecraft requirements. The following recommended conclusions from these functional design studies were incorporated into the *Mariner* Mars 1971 FTS.

(1) *Telemetered data.* Due to *Mariner* Mars 1971 channel assignment requirements, the analog measurement capacity was changed from 77 to 82 channels and the digital measurement capacity was changed from 17 to 12 channels.

A transition generator that inverts alternate engineering data bits was provided in the *Mariner* Mars 1971 design. This design feature prevents degradation of the data due to loss of synchronization during relatively long periods of no data, i.e., CC&S memory readout.

The clock for "CC&S events timing" was changed from FTS engineering word synchronization ÷ 2 to FTS engineering bit synchronization ÷ 2 for increased resolution.

(2) *Data rates.* The low-rate science data rate was changed from 66⅔ bits/s to 50 bits/s to optimize the science instruments requirements.

Block coder data rates were changed from 16.2 kbits/s to 16.2 or 8.1 kbits/s (DAS) and from 16.2 kbits/s to 16.2, 8.1, 4.05, 2.025, or 1.0125 kbits/s (DSS) to increase signal performance. Also, provisions were incorporated to control the block coder data rate from status information received from the source (DAS or DSS).

(3) *Mode changes.* The low-rate data playback (270 bits/s) mode used on the *Mariner* Mars 1969 Program was eliminated on the *Mariner* Mars 1971 Program.

(4) *CC&S memory readout.* The CC&S memory readout selection logic was changed from asynchronous to synchronous to eliminate noise problems experienced on the *Mariner* Mars 1969 Program, which were associated with false selection of the CC&S memory readout mode.

Redundancy. Redundant units, selectable by ground command, are provided for the ADC, data processor, and timing circuits.

Performance parameters. The accuracy of a measurement as read from the input to the FTS to the ADC output is maintained at ±1% of full scale for all 0–3 and ±1.5 V signals and ±3% of full scale for 0–100 mV and all temperature measurements. This accuracy is maintained for the mission lifetime requirements and under all specified environmental conditions.

Physical characteristics. The physical characteristics of the FTS are as follows:

(1) *Weight:* 23 lb (exclusive of case and case harness).

(2) *2.4-kHz squarewave power:* 16.1-W maximum.

(3) *Volume:* 750 in.^{3}.

d. Performance and testing. The *Mariner* Mars 1971 Project Office required environmental testing of all electronic, electrical, and electromechanical assemblies intended for flight on the *Mariner* Mars 1971 spacecrafts. The purpose of these requirements was to assure design qualification of the *Mariner* Mars 1971 assemblies and to demonstrate the flight acceptability of these assemblies for selected critical environments.

Since it was a minimum change *Mariner* Mars 1969 unit, the *Mariner* Mars 1971 FTS PTM had been subjected to type approval (TA) environmental test levels on the *Mariner* Mars 1969 Program. As a re-qualification for the *Mariner* Mars 1971 Program, the PTM was required to pass vibration tests at flight acceptance (FA) levels and thermal vacuum tests at TA levels and FA duration. The two flight FTSs were subjected to FA testing.

Subsystem testing

(1) *Launch vibration testing*

(a) Sinusoidal vibration tests. The FTS was subjected to sinusoidal vibration at frequencies between 5 and 2000 Hz. The sweep rate was logarithmic at 1.0 octave/min for TA tests and 3.0 octave/min for FA tests.

(b) Random vibration. The FTS was subjected to a shaped spectrum of random vibration. The sweep rate for the TA tests was 60 s per test axis and the sweep rate for the FA tests was 20 s per test axis. The vibration was of gaussian amplitude distribution, except that instantaneous peak amplitudes of greater than 3 σ were suppressed. The test requirements were identical for all three test axes.

(2) *Thermal vacuum tests.* The FTS thermal vacuum tests were implemented by using a conductive heat exchanger within the vacuum chamber. The TA temperature range was from −20°C to +75°C. The FA temperature range was from 0°C to +55°C. The FTS was operated during chamber pressure reduction. All modes and input–output measurements were verified at room temperature and at both the low and high temperature extremes.

Special tests

(1) *Subsystem calibrations.* Each FTS underwent special subsystem calibration in order to verify proper ADC operations and to provide highly accurate input–output data. Each FTS was calibrated using the calibration console. The calibration console provides the input of the FTS with a ramp function controlled by a detection network. The detection network responds to the digital output of the FTS. In this manner, the FTS (which includes analog switches, a 7-bit ADC, and associated signal conditioning networks) can be calibrated at the ADC "indecision zones" with repeatable accuracy of ±2.0 mV on the FTS 0.0 V to 3.0 V channels.

(2) *Margin tests.* Special subsystem margin tests were performed on the *Mariner* Mars 1971 FTS PTM. The object of these tests was to determine design margins of the FTS with respect to input voltage variation and FA temperature extremes.

(3) *Electromagnetic compatibility tests.* The FTS PTM was subjected to electromagnetic compatibility testing for the purpose of evaluating the performance of the FTS when subjected to simulated noise and crosstalk on spacecraft interface wiring.

e. Present status. The first two FTS subsystems (*Mariner* Mars 1969 hardware modifications) were completed and delivered for spacecraft testing on schedule. The third (new) FTS subsystem is presently under test with delivery scheduled for August 31, 1970. The subsystem contractor (Texas Instruments, Inc.) is completing the final stages of its design, fabrication, and test responsibilities with assembly and test of several spare modules prior to contract closeout, which is expected by October 1, 1970.

E. Propulsion

1. Propulsion System

The *Mariner* Mars 1971 spacecraft incorporates an on-board modularized propulsion subsystem to furnish impulse to the spacecraft for trans-Mars trajectory correction, orbit insertion, and orbit trims. The propulsion subsystem operates on liquid propellants: nitrogen tetroxide and monomethyl hydrazine. The subsystem is a regulated-pressure, constant-thrust system employing (1) gaseous nitrogen pressurant stored at 3650 psia within two 15-in.-diam titanium vessels, (2) teflon-bladdered, 30-in. titanium propellant tanks capable of storing 635 lb of nitrogen tetroxide and 410 lb of monomethyl hydrazine, (3) two pressurant check and relief valve assemblies, (4) explosively actuated isolation valves in both the pressurant and liquid circuits, and (5) a 300-lbf thrust, conduction-cooled rocket engine.

2. Pressurant Relief Valve Component Evaluation

a. Introduction. The pressurant relief valve is located in the propellant feed portion of the propulsion subsystem (PSS), more particularly as part of the pressurant storage and control subassembly. The specific location of the relief valve is shown diagrammatically in Fig. 23; note that two relief valves are present in the propulsion system, one for each propellant tank. The primary purpose of the relief valve is to vent off high-pressure gases in the event of gas regulator failure, and thereby avoid possible rupture of the lightweight thin-shell propellant tanks. The requirement for this safety device is necessitated by the storage of *Mariner* Mars 1971 PSS N_2 pressurant gas at 3650 psia regulated down to 260 psia as applied to each propellant tank. The relief valve is designed to initiate venting at 320 psig nominal system pressure, and to permit an N_2 throughput of 0.125 lb/s without exceeding 340 psig at its inlet, which is to say at the propellant tank inlet. Thus, these capacities will prevent the pressure in the propellant tank from exceeding the tank proof pressure (450 psig) and thereby avoid any risk of mission degradation. The outlet of each relief valve is branched to two equal and opposing nozzle configurations to prevent the application of any unbalanced forces (torques) to the spacecraft when venting occurs.

b. Design and operation. As noted above, the relief valve (RV) is primarily required to provide a controlled

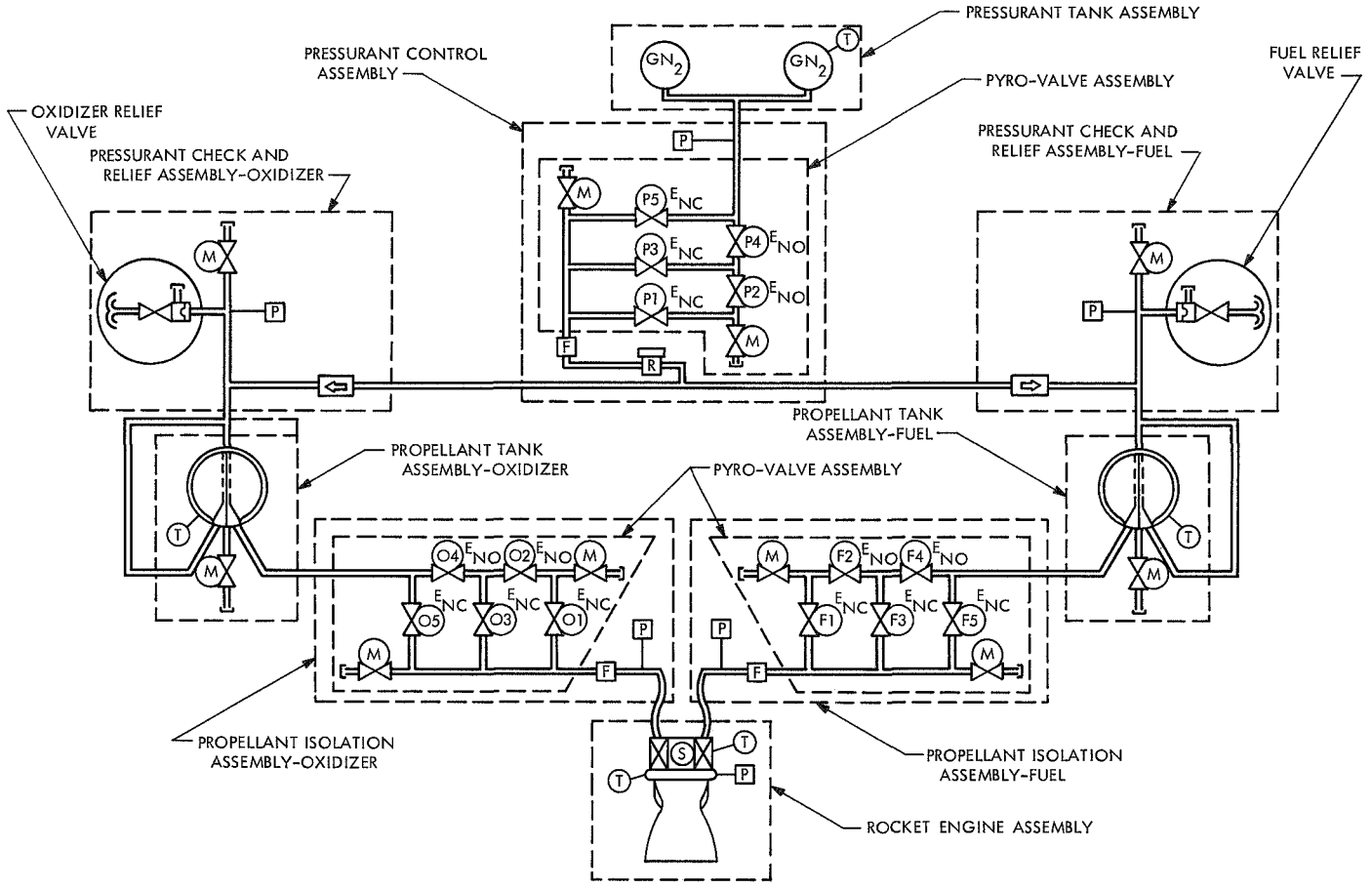

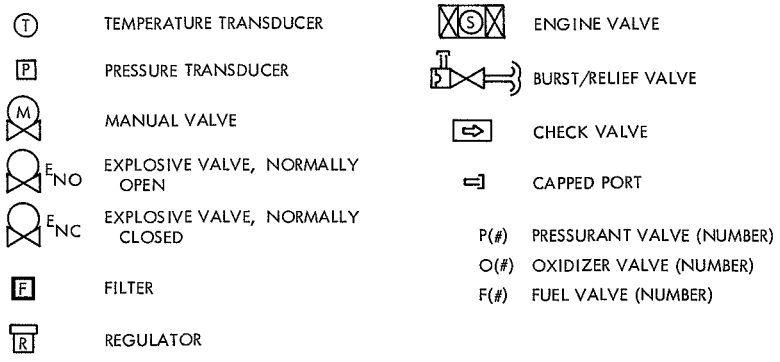

Fig. 23. Propulsion subsystem

free access sink for mass deposition of N_2 pressurant gas. This function must occur quickly and reliably at specifically designated pressures should a regulator failure occur. Failure to protect the propellant tanks in such an eventuality could result in gross mission failure. Thus, the basic attributes of the relief valve must include the following features:

(1) It must be capable of immediate relief at its design operation pressure.

(2) It must have virtually no leakage (for extended space missions) in its pressurized passive mode.

(3) It must be able to withstand unlimited cycling up to pressures just under its relief pressure without degrading the preset relief pressure level.

Additionally, the relief valve must be capable of satisfactory service under the usual environments of propellant exposure, temperature, and vacuum customary for liquid propulsion systems for space application. The specific values derived to assure the above features are:

(1) A burst diaphragm initial rupture pressure (for initial relief) of only 20 psi (i.e., ± 10 psi) tolerance band on the relief pressure of 320 psi.

(2) A minimum throughput of 0.125 lb/s N_2 and 340 psig maximum at valve inlet.

(3) A leakage rate of not greater than 1×10^{-7} scc/s He at 300 psi.

(4) No degradation of designated relief pressure after a maximum of 1000 pressure cycles at 95% of relief pressure.

All these requirements were met for the *Mariner* Mars 1971 relief valve by incorporating two simple mechanical devices: (1) a spring-loaded sliding poppet in series with and downstream of a (2) thin-gage burst disc. The poppet arrangement provides the capability of repeated on–off operation so that high pressure is vented only while the level is above the relief valve design value. Thus, as soon as the supply pressure is reduced (below the design relief pressure), the poppet closes to conserve gas for continued mission utilization. The burst disc, being a passive device, will provide an extremely leak-tight obstacle while it is on-line in standby mode; however, it can also be ruptured simply, upon demand, within ± 10 psig of the design relief pressure. A longitudinal cross-section view of the relief valve is shown in Fig. 24, which illustrates the burst disc, the main relief poppet, and their respective integrating details.

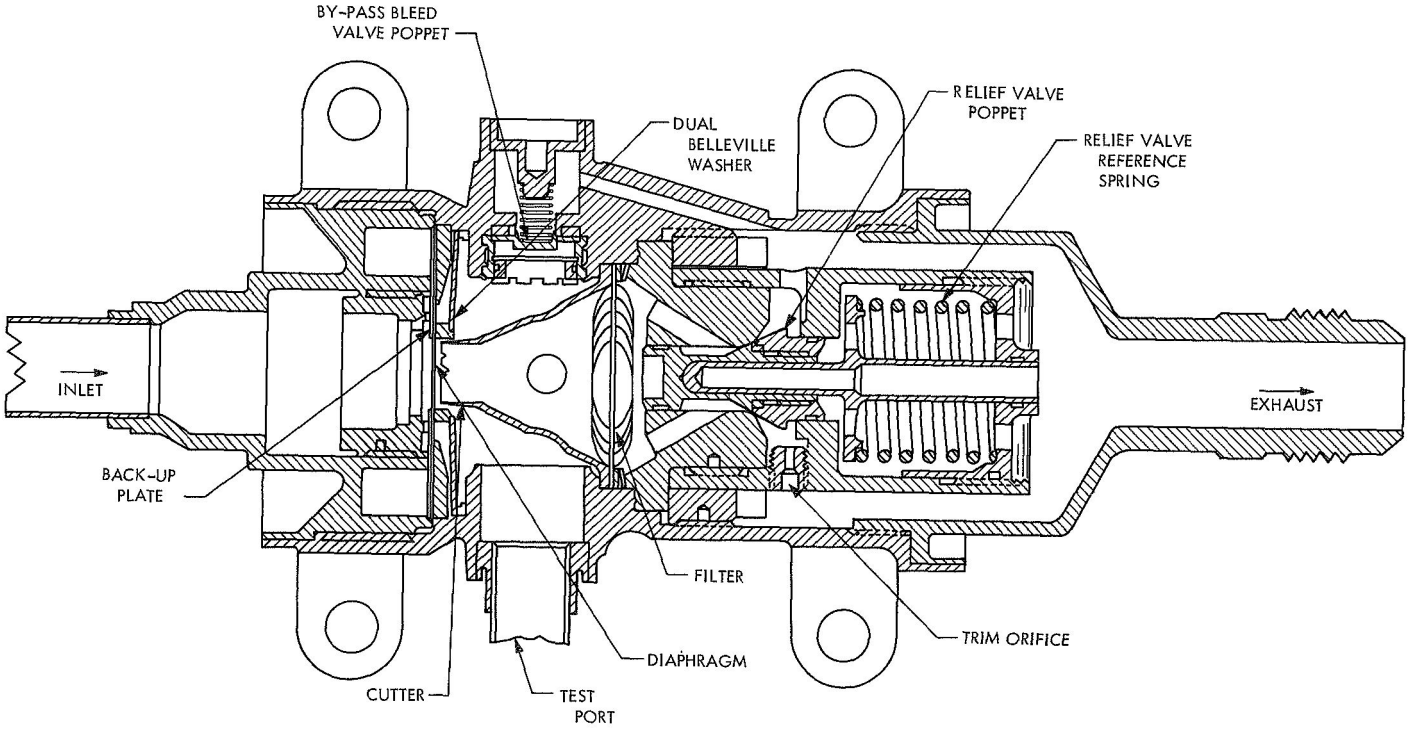

Fig. 24. Pressurant relief valve

The essence of safe and reliable disc bursting operation in this component is the unique application of a supporting Belleville spring. Unlike coil springs that require a uniformly increasing force to compress, the Belleville spring can be designed to change from increasing to decreasing force during its stroke. This is shown qualitatively in Fig. 25. By presetting the load on the backup Belleville spring to a specific range, the travel prior to spring snap-over is minimized and assures immediate burst of the relief disc by cutter action. Other detail features of the assembly are:

(1) A variable trim orifice to adjust the main poppet closing pressure.

(2) Teflon seat material, with metal backing, for tight closing action to minimize leakage.

(3) A low pressure-drop filter (screen) to withhold disc particles that otherwise might damage the poppet seat.

(4) A by-pass bleed valve to vent off any gas accumulating between the disc and main seat.

The feature listed in (4) was incorporated in view of the extremely thin gage disc, which may develop pinhole leaks. This auxiliary bleed poppet is normally open at a pressure from 0 to 20 psid to allow gas venting (from the potential pin hole leaks) and closes from 20 to 40 psid as the applied pressure continues to build up following normal burst diaphragm rupture. Without this by-pass poppet, pressures on each side of the burst disc could become equalized and, although the ΔP required to burst the diaphragm would not be affected, the upstream pressure might require a value of upwards to 600 psi before rupture and relief would occur. Obviously, since the *Mariner* Mars 1971 relief setting is at 320 psi, a 600 psia pressure at the propellant tanks would be intolerable. The valve is constructed entirely of 18-8 steel and hard anodized aluminum; total weight is 3.3 lb. A cutaway view of the valve is shown in Fig. 26.

c. Specific modifications for Mariner Mars 1971 application. The relief valve configuration employed for *Mariner* Mars 1971 has had extensive qualification and flight confirmation during the *Apollo* manned space program. It is used in both the Service Module and the Lunar Excursion Module and has performed with no malfunctions. Nonetheless, certain design improvements required by *Mariner* Mars 1971, together with the change required for operating pressures peculiar to *Mariner* Mars 1971, necessitated a margin limit test

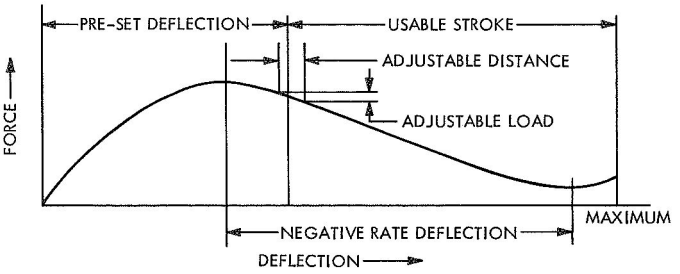

Fig. 25. Belleville spring characteristic deflection for relief valve application

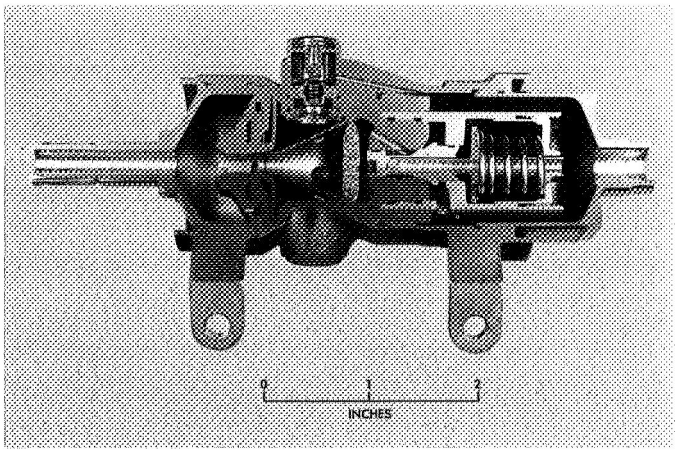

Fig. 26. Pressurant relief valve (cutaway view)

(MLT) program on the components. These improvement changes are listed below:

(1) Use of AISI (full hard) stainless-steel burst disc, in place of aluminum, for improved service in corrosive environments.

(2) Use of welded-in burst disc, to replace an earlier mounting installation, for improved leakage service.

(3) Installation of a backup supporting disc on the upstream side of the burst disc to avoid disc damage in the event of an inadvertent reverse pressurization.

(4) Increased length (Δ = 0.015 in.) on the poppet support surfaces to prevent seat chatter during vibrational loads.

In the MLT program structured by JPL to qualify these changes, the primary test conditions that were selected were:

(1) Internal pressure loading.

(2) Gas flow at elevated temperature.

(3) Burst disc pressure cycle endurance.

(4) Poppet seat actuation cycle endurance.

(5) Vibrational environment.

(6) Shock environment.

(7) Flow characterization from 50 to 150% of rated flow.

(8) Propellant exposure.

In order to make maximum use of the available test components, only four valves were used for the MLT. It is noted that none of the tests are repeats of one another; therefore, the testing scope is necessarily non-regressive. Nonetheless, as conducted, the program indicates that the relief valve will function within the prescribed limits. There were no problems or failures encountered during this MLT. Table 5 shows the MLT matrix for the relief valve.

At the end of the MLT program, relief valve 8 was completely disassembled and each piece-part individually examined for any indications of marginality that might limit the valve performance under expected mission conditions. The significant findings of this piece-part evaluation are summarized below.

Table 5. Pressurant relief valve MLTs

Test condition	Valve serial number			
	8	9	10	11
Acceptance test at vendor	1	1	1	1
Abbreviated acceptance test at JPL consisting of: proof, leak, crack, and reseat	2	2	2	2
Diaphragm endurance, 2000 cycles, 0–295 psig	3	4		
Diaphragm reverse loading, 4 cycles, 1 h each, 0–350 psig	4	3		
Diaphragm rupture	5	5	6	6
Vibration: sine and random combined	6	6	4	4
Shock loading			5	5
Valve poppet endurance, 5000 cycles	7	7		
Flow vs ΔP, 50 to 150%, room temperature	8	8	7	7
Flow vs ΔP, high and low temperature; at rated flow	9	9		
Propellant exposure, N_2O_4			3	
Propellant exposure, MMH				3

NOTE: Numbers in the columns under each valve serial number indicate the sequential order of testing.

Cleanliness. Of some 56 parts comprising the relief valve assembly, three non-critical parts showed evidence of stain marks of the type indicating possible residue from cleaning fluids. Five pieces showed the presence of several metal particles. However, all appeared to be confined to surface contact rather than to have been embedded at critical seating surfaces. The general particulate count for affluent gas (15 ft^3) was only slightly in excess of the components cleanliness requirements. It is felt that the larger particles probably were generated during the disassembly operation.

Surface wear. Most parts showed bearing marks from mating-part contact, although none gave any indication of excessive wear. None of the anodized surfaces were disturbed or showed any cracking or chipping.

Dimensional verification. Approximately 20 piece-parts were accurately measured at their critical mating or contacting surface(s). Only two measured dimensions were not within their drawing tolerance requirements, although the slightly excessive clearance thus obtained was not detrimental to valve operation.

d. Component performance record to date. Beyond the component tests described above, the relief valve has seen extensive service in several overall propulsion system models. The relief valve has performed acceptably throughout all evaluations. The valve record to date adds further confidence to the expected satisfactory performance during actual flight application.

3. Analysis of Pressurant Gas Solubility in the *Mariner* Mars 1971 Propellant Tanks

a. Introduction. The oxidizer tank is filled to 90.0% capacity with 635 lb of nitrogen tetroxide (N_2O_4), and the fuel tank to 95.7% capacity with 410 lb of monomethylhydrazine (MMH); each tank is pressurized to 30 psig after completion of the propellant loading. The initial ullage gas will be loaded inside the bladders in order to minimize loading of the teflon bladders during launch acceleration and vibration. Gas separators and liquid traps in the standpipes will prevent gas bubbles from being drawn into the feed lines and engine.

After the propellants have been stored for up to 6 wk before launch, enough gas will have dissolved into the

propellants for the pressures to decrease and the propellants to saturate at 30 psia. The pressurant squib valves will be opened 5 days after launch, and 1 day before the first midcourse maneuver. Nitrogen gas will flow through the regulator to the tanks and increase the pressures on the outside of the bladders to 260 psi. The gas bubbles inside the bladders will be compressed to approximately 135 in.^{3} in the oxidizer tank and 75 in.^{3} in the fuel tank. Gas will begin to permeate through the bladders and diffuse from the bladders and from the bubbles into the liquid. The pressurant and propellant squib valves will be closed 1 wk after the midcourse, and, as gas continues to dissolve into the propellants, the pressures will decrease.

Nominally, 20 wk after the propellant tanks are isolated, the pressurant and propellant squib valves will be opened, allowing the tanks and propellant feed lines to be repressurized to the regulated pressure. Then, 1 day later, there will be a short second midcourse firing; 3 wk later, there will be a 900-s orbit-insertion firing.

The dissolved nitrogen will affect the mixture ratio and unusable propellant residue after the orbit-insertion firing; the gas bubble volume inside the bladders could affect the gas-free delivery of propellants through the standpipe. The propellant tank pressures will affect the magnitude of the waterhammer surge during the propellant squib valve actuation before the second midcourse. The pressure differential between propellant tanks will affect the gas and vapor leakage through the check valves during cruise. A determination of the amount of gas absorption expected was required in order to evaluate the phenomena discussed above.

b. Discussion. A mathematical model of the *Mariner* Mars 1971 propellant tanks was developed to predict the rate of pressurant gas absorption into the liquid propellants, the volume of the gas bubble inside the teflon bladders, and the propellant tank pressures before the second midcourse pressurization. The model was programmed for use on the Univac 1108 computer to print and plot gas concentration, average gas concentration, bubble volume, and tank pressure as functions of pressurant squib valve profile, radius, and time. Required inputs are propellant and initial bubble volumes, propellant diffusivity and solubility, bladder permeation coefficient, and the bladder thickness.

Nitrogen gas will permeate through the Teflon bladders and diffuse into the liquid propellants because of a concentration gradient that develops after the first midcourse pressurization. These processes can be compared to the transfer of heat due to a temperature gradient. Diffusion of gas through liquid (with resistance and capacitance) is analogous to the conduction of heat:

$$\text{Heat Conduction:}\quad \frac{dq}{dt} = -kA\frac{dT}{dx} \tag{1}$$

$$\text{Gas Diffusion:}\quad \frac{dm}{dt} = -DA\frac{dC}{dx} \tag{2}$$

Concentration C is analogous to temperature T, diffusivity D is analogous to conductivity k, and mass transport rate dm/dt is analogous to heat transfer rate dq/dt. Permeation of gas through the Teflon bladder (with resistance only) is analogous to the convection of heat:

$$\text{Heat Convection:}\quad \frac{dq_{12}}{dt} = hA\,(T_1 - T_2) \tag{3}$$

$$\text{Gas Permeation:}\quad \frac{dm_{12}}{dt} = \frac{\sigma KA}{s}\,(C_1 - C_2) \tag{4}$$

The product of the permeation coefficient σ times Henry's constant K divided by bladder thickness s is analogous to the heat convection coefficient h.

Since liquid volume is analogous to thermal capacitance, the second-order differential equation describing each system is a similar form of the Fourier Equation:

$$\text{Heat Transfer:}\quad \nabla^2 T = \frac{1}{\alpha}\frac{\partial T}{\partial t} \tag{5}$$

$$\text{Mass Transport:}\quad \nabla^2 C = \frac{1}{D}\frac{\partial C}{\partial t} \tag{6}$$

The thermal diffusivity α is analogous to the mass transport diffusivity D.

In the gas diffusion model, the mass transport equations were rewritten and solved as finite difference equations. The liquid propellant volumes were assumed spherical and contained within bladders exposed on the outside to pressurant gas. The initial ullage bubble inside the bladder was assumed spherical and located at the center of the tank (Fig. 27). Provisions were made for varying the bubble's surface area, at constant volume, to investigate the effects on bubble decay if the bubble were to attach to the standpipe or bladder walls.

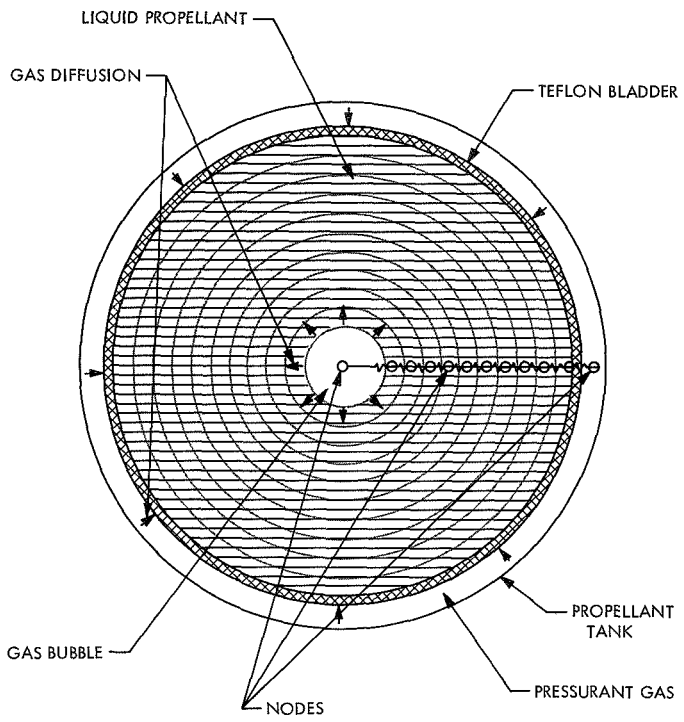

Fig. 27. Propellant tank gas diffusion model

The liquid volume is divided into 10 concentric spheres and represented as 10 liquid nodes. Each node is defined by a volume (capacitance) and gas concentration (potential); the nodes are connected by variable liquid conductors (Fig. 27).

The gas ullage volume outside the bladder and the bubble volume inside the bladder are represented by two gas nodes. Gas pressures are assumed equal to the regulated pressure (260 psia) when the pressurant squib valves are open, but will decrease as gas dissolves into solution after the squib valves are closed. The effective gas concentration in the gas volumes is equal to the pressure divided by the liquid solubility (inverse of Henry's Constant). Gas nodes are connected to the liquid nodes by two variable conductors corresponding to the bladder on the outside radius and to liquid on the inner radius. Positions and volumes of each of the nodes, and the conductance of each of the conductors, is calculated by the program. The program recalculates each conductance as the bubble volume and surface area decrease.

Sample runs were made with 3 and 20 liquid nodes before the optimum of 10 was selected. The program solutions were verified by comparison with existing solutions for simple configurations and by hand calculation for the more complex configurations.

After the computer program was verified, it was used to predict the nominal propellant saturation, bubble volume, and tank pressure, and to determine the effect of variances and uncertainties in squib valve profile, propellant diffusivity, and bladder permeation coefficient.

From testing and analysis, the diffusivities, permeabilities, and solubilities were determined as follows:

Input	N_2O_4	MMH	Teflon (5 mils TFE, 5 mils FEP)
Diffusivity ($in.^2/s$)	6×10^{-6} to 10×10^{-6}	3×10^{-6} to 21×10^{-6}	—
Solubility (scc_{N_2}/psi gm_{sol})	0.01	0.0024	—
Permeation Coefficient (lbm_{N_2}-in./ $in.^2$-h psi)	—	—	0.65×10^{-11} to 2.6×10^{-11} (1.2×10^{-11} nominal)

For the nominal mission predictions, it was assumed that the propellant tanks will be isolated from the pressurant tanks 1 wk after the first midcourse maneuver, the diffusivity of nitrogen was assumed to equal 10×10^{-6} $in.^2/s$ in N_2O_4 and 21×10^{-6} $in.^2/s$ in MMH, and the nitrogen permeation through the teflon bladder was assumed to equal 1.2×10^{-11} lbm_{N_2}-in./$in.^2$-h psi.

The results indicated that the oxidizer would become 55% saturated and the MMH 90% saturated at 260 psi at the time of the orbit-insertion firing. The 135-$in.^3$ gas bubble inside the oxidizer bladder will dissolve into solution before the second midcourse maneuver, but, because of the lower solubility of the MMH, more than 40 $in.^3$ of gas will remain inside the fuel bladder. At the time of the second midcourse pressurization, the oxidizer tank pressure will have decreased from 260 to 120 psi and the fuel tank pressure from 260 to 200 psi. The nominal predicted gas concentrations, bubble volumes, and pressures for the oxidizer and fuel tanks are plotted in Figs. 28 and 29.

The variation in propellant diffusivity and bladder permeability results in less than 15% variation in propellant saturation and tank pressure before the second midcourse pressurization.

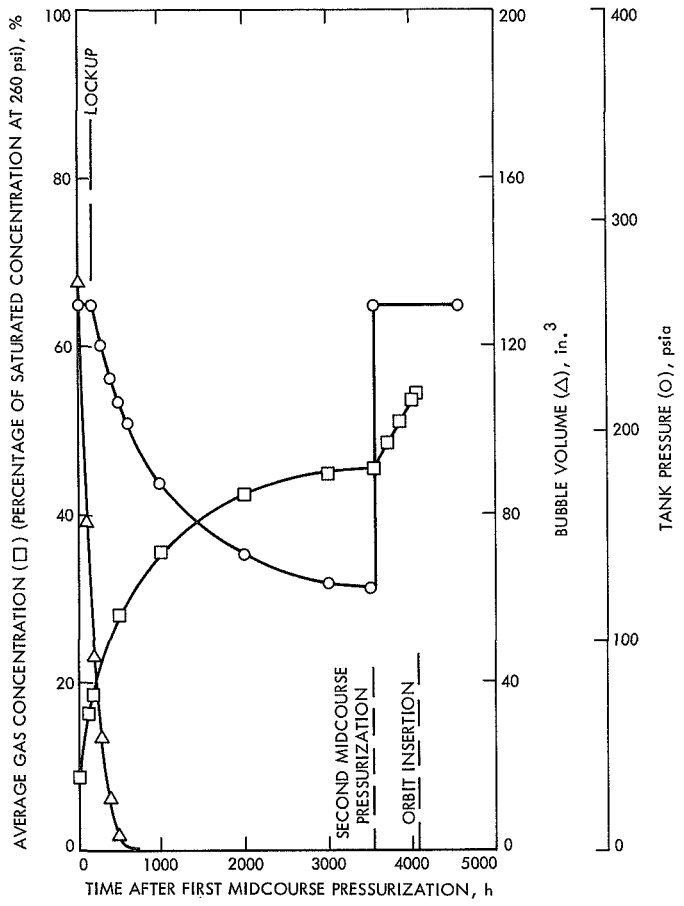

Fig. 28. Oxidizer tank predicted N_2O_4 saturation, pressure, and bubble volume vs time

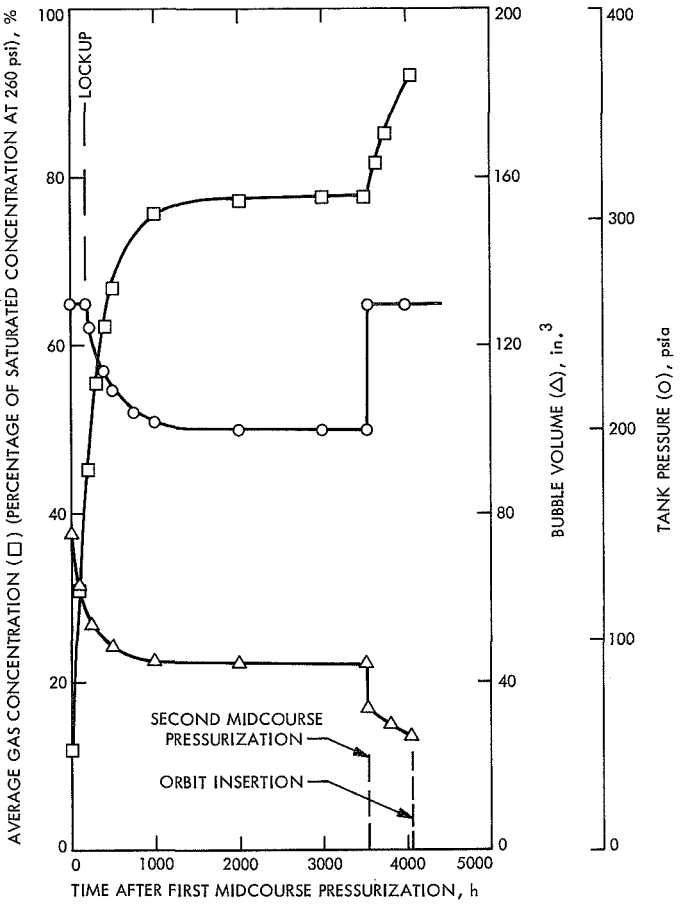

Fig. 29. Fuel tank predicted MMH saturation, pressure, and bubble volume vs time

If the pressurant squib valves are left open and the tanks are exposed to 260 psi for 24 wk, the oxidizer will become 80% saturated and the fuel 100% saturated before the orbit-insertion firing. Variations in propellant diffusivity and bladder permeability could increase the oxidizer saturation to 90% and decrease the oxidizer and fuel saturations to 55 and 85%, respectively. Again, the bubble inside the oxidizer bladder will dissolve into solution before the second midcourse pressurization, but most of the gas inside the fuel bladder will remain.

c. Conclusion. When the predictions for the nominal mission profile are combined with results from engine flow tests and feed-line waterhammer tests, it is concluded that:

(1) There will be little or no mixture ratio shift due to dissolved gas.

(2) Waterhammer pressures will be high enough to shift the feed-line pressure transducer by 30 to 35%, but not high enough to burst a component or result in any external leakage.

Although no problems are expected, the fuel standpipe's bubble retention capacity and the potential check-valve gas or vapor leakage are still being evaluated. Full-scale propellant storage tests are also being conducted and the computer program will be modified for the 1-g configuration (decrease in bladder permeation area and possible increase in propellant diffusivity). The test results will hopefully further verify the mathematical model.

4. Scan Latch Subsystem Manifold Assembly

The scan latch subsystem is a prepressurized gaseous nitrogen system that, when actuated, will unlatch the planetary platform to point the scientific instrument payload with great precision at the Martian surface. The subsystem consists of the manifold assembly, a spring-loaded pneumatic cylinder, an unlatching mechanism, and a closely-coupled opposed nozzle overboard vent.

The manifold assembly consists of a normally-closed explosive valve to control the start of flow, a ball-type fill valve, and a flow manifold block. A similar assembly was used on the *Mariner* Mars 1969 planetary platform latch subsystem (scan latch subsystem). The manifold assembly fill valve allows pressurization of the system with 1500 psig of nitrogen. At pressurization, the pneumatic piston is forced back against the return spring until the spring is closed. The piston is linked to a hooking latch (similar to the household hook and eye arrangement) that locks the scan platform in a fixed position during the launch phase. When required, the explosive valve is fired to the open position thus starting the flow of gas to the overboard vent. As pressure decays, the piston spring overcomes the pneumatic force acting on the piston head and returns it to its original position. This motion is transmitted by linkages to the latch mechanism, which unlocks the platform for positioning as required.

Although a valve assembly of similar design was qualified for the *Mariner* Mars 1969 Program, certain problems discovered then and resolved prior to launch strongly suggested a revision of the design for continued use in order to assure satisfactory performance. The problems that were identified and their solutions were as follows:

(1) The rams overtraveled when *Mariner* Mars 1969 squibs were used in place of surplus *Mariner* Mars 1964 squibs with which the preproduction valves had originally been tested. Nominal ram travel was achieved by redesigning the ram to stop sooner.

(2) The brazed joints failed as the result of ram overtravel. The resulting nitrogen leakage was excessive. The external joints were electron beam welded to reinforce the braze material. This solution, together with the solution in (1) above, resulted in no further valve failures.

(3) The annealed (dead-soft) aluminum crush gaskets, used in conjunction with serrations in the flanges, yielded beyond recovery at valve operation (firing shock). This condition resulted in nitrogen leaks at both the inlet and outlet ports. The problem was solved by substituting an elastic material (viton rubber) washer with a stainless-steel hub for the aluminum gasket. The nonstandard configuration of the gland prevented the use of a catalog seal or O-ring.

(4) The fill valve seat yielded from the impact with the ball during valve operation because of the magnitude of pyro shock. The result was excessive nitrogen leakage past the ball. This problem was resolved by a change to the seat lapping procedure to achieve a larger seat contact area. This larger area reduced the transient but high loading on the seat during the pyro shock condition.

The resolution of the *Mariner* Mars 1969 valve problems provided the basis for the improved design used for *Mariner* Mars 1971 (Fig. 30). The *Mariner* Mars 1971 version of the valve incorporated the following modifications:

(1) The ram modification was retained with some minor complimentary refinement in the bore taper. A positive stop in the form of a shoulder was added in the bore. Surplus *Mariner* Mars 1969 squibs from the flight lot designated for *Mariner* Mars 1971 were used to test the preproduction valves. The results of these tests were satisfactory.

(2) The valve body structure was redesigned to improve the rigidity at the outlet port flange and between the fill valve and explosive valve bosses. Structural changes included the reduction of external joints from two to one and the number of internal joints from three to two. The braze void was modified further to improve flow of braze material and flux. The improvement to joint efficiency was clearly discernible in the X-ray plates.

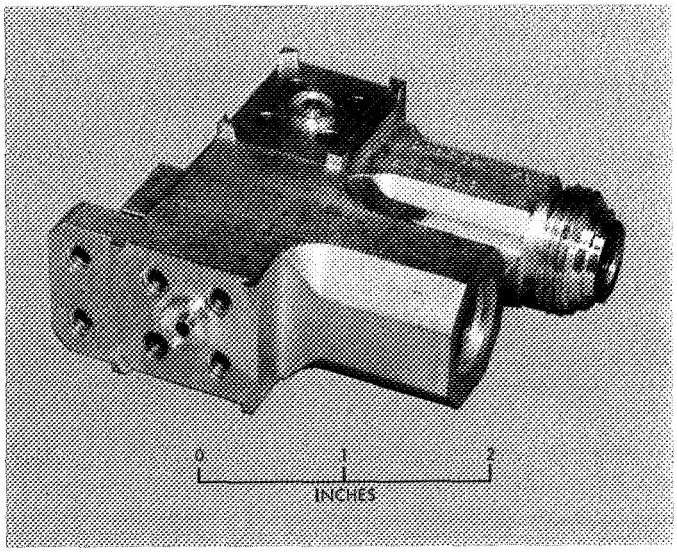

Fig. 30. Scan latch manifold assembly (without squib and fill cap)

(3) The seal gland was redesigned to incorporate a standard viton O-ring seal at both the inlet and outlet ports. Leak tests showed that the O-ring configuration was more stable than the washer used in *Mariner* Mars 1969 under both increasing or decreasing pressure conditions.

(4) The earlier refinements to the fill valve seat were continued without change.

Because of the type and number of changes involved, it was decided to requalify this valve. The *Mariner* Mars 1971 qualification test (or type approval test) program was performed and satisfactorily completed on four manifold assemblies.

In summary, this valve design is considered satisfactory for its application.

5. Study of the Effects of Solvent on *Mariner* Mars 1971 Liquid Propellant Expulsion Teflon Bladder Bags

a. Introduction. Liquid propellant expulsion Teflon bladder bags for *Mariner* Mars 1971 have been failing due to the formation of tears and cracks near an aluminum seal ring that forms the mouth of the bag. From a consideration of the conditions imposed on the bags during flight acceptance testing, four factors believed to be critical in contributing to the failures were identified. These are as follows:

(1) Solvent sensitivity.

(2) Biaxial stresses.

(3) Fatigue.

(4) Crystallinity.

A detailed investigation of these properties for the standard laminate bladder bags has been initiated. This article, the first report on the results of these studies, is concerned with solvent sensitivity. Also discussed are results obtained on a new experimental material designated "co-dispersion laminate."

b. Experiment. The effects of solvent on co-dispersion- and standard-laminate Teflon bladder bag materials were assessed through an analysis of uniaxial stress–strain properties measured on dumbbell specimens immersed in solvents. The solvents employed were heptane, isopropyl alcohol, Freon–TF, and water. Heptane was included because of its known effect on Teflon materials, while the latter three solvents were selected because they are employed as the referee fluids in the flight-acceptance testing of the bladder bags.

Dumbbell specimens were tested immediately after immersion, after a 64-h presoak period, and after a 168-h presoak period. After the 64-h presoak, specimens were removed from the test solvents, allowed to air dry for 24 h, and then tested in air. The 24 h air-drying period was found adequate to dry the samples free of test solvent, except for the freon-exposed samples, which were found to contain upwards of 5 wt% solvent after 24-h of air drying. An additional drying period of 3 days under vacuum prior to test reduced the solvent content of these samples to about 1 wt%.

The test results are tabulated in Tables 6 and 7. A stress–strain curve typical of these materials is shown in Fig. 31.

c. Discussion. The stress–strain curve shown in Fig. 31 is characterized by two distinct regions, the first an initially steep rise in stress at very low strains followed by a large increase in strain with only a gradually increasing stress. The stress corresponding to the bend in the curve is the yield stress for the Teflon materials. Although solvent exposure did not alter the basic appearance of this stress–strain curve, it did affect the magnitudes of the yield stress and the stress and strain at break (ultimate properties). These are the data tabulated in Tables 6 and 7.

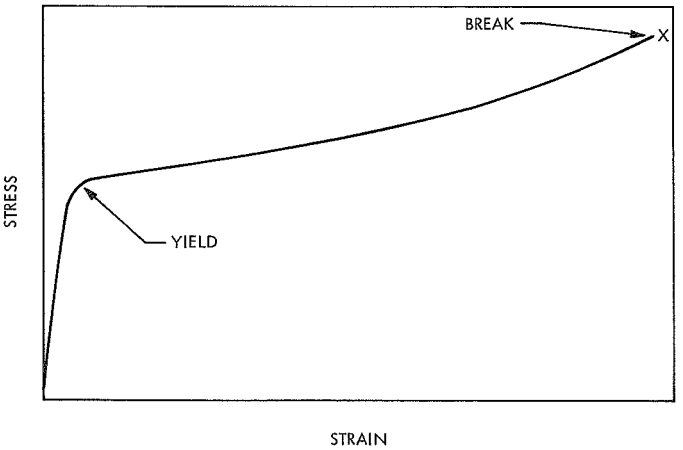

Fig. 31. Stress–strain curve typical of Teflon bladder bag materials

Table 6. Uniaxial data from exposure of co-dispersion and standard laminates to solvent (crosshead speed = 10 in./min)

Test condition	Co-dispersion laminate (S/N 1113)			*Standard laminate* (S/N 2)		
	Yield, psi	Ultimate stress, psi	Ultimate strain, %	Yield, psi	Ultimate stress, psi	Ultimate strain, %
Control, air tested	1874	4455	450	1925	3391	435
Heptane, immersion tested:						
Presoaked: 0 h	1930	3930	396	1911	2346	162
64 h	1740	4480	462	1700	2620	223
168 h	1683	4633	464	—	—	—
Dried in air 24 h and air tested after 64-h presoak	1805	4504	484	1700	3500	424
Iso-propyl alcohol, immersion tested:						
Presoaked: 0 h	1968	3396	324	1927	3152	330
64 h	2040	4814	446	1900	2950	282
168 h	1999	5046	472	—	—	—
Dried in air 24 h and air tested after 64-h presoak	2050	4915	498	1900	4000	488
Water, immersion tested:						
Presoaked: 0 h	1984	4128	392	1888	3444	324
64 h	2017	4623	454	1970	4076	394
168 h	2038	4876	434	—	—	—
Dried in air 24 h and air tested after 64-h presoak	1980	4920	504	1921	4039	490
Freon–TF, immersion tested:						
Presoaked: 0 h	1930	3813	407	1907	2772	254
64 h	979	4297	516	900	2600	321
168 h	796	4422	542	—	—	—
After 64-h presoak:						
Tested in air after 24-h air dry	1377	4528	512	1209	3486	452
Tested in air after 24-h air dry plus 3 days under vacuum	1638	4799	504	1632	4040	472

Table 7. Uniaxial data from exposure of co-dispersion and standard laminates to solvents (crosshead speed = 2 in./min)

Test condition	Co-dispersion laminate (S/N 1113)			*Standard laminate* (S/N 2)		
	Yield, psi	Ultimate stress, psi	Ultimate strain, %	Yield, psi	Ultimate stress, psi	Ultimate strain, %
Control, air tested	1746	4500	471	1753	3178	399
Heptane, immersion tested after 64-h presoak	1563	4509	489	1560	2520	313
Iso-propyl alcohol, immersion tested after 64-h presoak	1888	4518	459	1854	3018	339
Water, immersion tested after 64-h presoak	1938	5142	488	1749	3692	417
Freon–TF, immersion tested after 64-h presoak	600	3510	489	609	2133	312

In general, the following principal effects were observed:

(1) All solvents significantly reduced the ultimate properties of the standard laminate, which indicates that this material is highly sensitive to solvent stress-cracking.

(2) Solvent exposure did *not* affect the ultimate properties of the co-dispersion laminate, which indicates that this material is *not* prone to solvent stress-cracking.

(3) Freon reduces the yield stress of both laminates, although it affects the ultimate properties only of the standard laminate.

(4) The solvent sensitivity of standard laminate is revealed only during immersion testing. Removing the specimens from the test solvent and air drying them results in a recovery of their initial properties.

(5) Co-dispersion laminate displays a significant improvement in resistance to solvent attack as compared to the highly solvent-sensitive standard laminate.

(6) Freon plasticizes both laminates, imparting a more rubbery character to the materials.

(7) Both co-dispersion and standard laminates experience an immediate reduction in ultimate properties upon exposure to solvents, although the effect is more critical with the standard laminate. With further exposure, both co-dispersion and standard laminates undergo a recovery in ultimate properties. The co-dispersion laminate achieves or surpasses its initial properties, while the standard laminate, even with some recovery, displays significantly lowered properties as compared to its initial properties.

(8) Water and isopropyl alcohol exposure appear to improve the ultimate stress of the co-dispersion laminate, either in the wet or dry condition.

(9) The solvent sensitivity of standard laminate appears to increase with increasing crosshead speed on the Instron.

d. Conclusions. Three conclusions can be inferred from the data:

(1) Co-dispersion laminate is not susceptible to solvent stress cracking; therefore, no effect from fuel and N_2O_4 would be expected.

(2) Standard laminate, being susceptible to solvent stress cracking, can be expected to be affected by exposure to N_2O_4 and fuel.

(3) Mechanical property data[5] has indicated that N_2O_4, like freon, plasticizes the teflon materials. Since no stress-cracking effect of N_2O_4 on co-dispersion laminate is expected, this material should assume more rubber properties in the presence of N_2O_4, thus helping to increase service lifetime.

F. Engineering Mechanics

1. Introduction

During the present reporting period, several problems have been encountered with the propulsion support structures and the solar panel deployment/damper mechanisms. A description of the problems and the changes resulting from their solution are discussed in Subsections 2–6. Also included are descriptions of the new medium gain antenna RF plug design, the propellant tank fluid dynamics tests, and the cracked solder joint investigations.

2. Propulsion Support Structure

a. Introduction. SPS 37-62, Vol. I, pp. 7–11 contains a description of the propulsion support structure design and fabrication techniques, along with materials used and the rationale for their selection. Since then, all units have been fabricated and structural qualification testing completed.

As designed, the primary truss structure and pressurant bottle supports (beryllium tubes bonded to magnesium end fittings) weighed 18.20 lb, which is 11.5 lb less than the weight of an aluminum design. However, during the test program, several difficulties that were encountered resulted in design changes that increased the structure weight by 2.55 lb.

Fabrication and handling techniques set forth initially proved to be adequate. The moderate amount of care that had to be exercised for personnel safety and for protection of the material had minimal impact on fabrication and assembly procedures.

[5]Unpublished results from A. B. Sorkin, JPL Materials Section.

b. Propulsion structure problems. During developmental testing, the propulsion structure experienced several difficulties which resulted in the generation of nine problem/failure reports (P/FRs) and some concern about the integrity of the subsystem. The problems, their causes, and the solutions are summarized in Table 8.

The propulsion support structure P/FRs are listed in Table 8 in the order of their occurrence. Along with each is a brief description of the cause and corrective action taken. Figure 32 shows the propulsion support structure; the locations of the various failures are shown in Fig. 33. (The circled numbers in Fig. 33 refer to the failure item numbers in Table 8.)

Two of the P/FRs (items 3 and 4 covering failure of the upper truss fittings) are the result of a design deficiency; item 7 (pressurant bottle support tube fracture) resulted from failure to recognize the impact of the severe subsystem test environment on a marginal member. Of the remainder, two P/FRs (items 2 and 9) stem from manufacturing or assembly problems, two (items 1 and 5) involve improper test procedures, and two (items 6 and 8) result from repeated testing at the more severe subsystem level. The remainder of this subsection contains supplemental information on each failure.

Item 1—beryllium tube strength. During each truss bonding operation, a bond test specimen was prepared

Table 8. Propulsion support structure problems

Item	Date	Nature of problem	Cause	Corrective action
1	1/15/70	Low-strength beryllium tube in bond test specimen (bond qualification test program).	Improper installation of specimen in tensile test machine induced binding.	None. Stress calculations considering bending and tension produced a satisfactory value.
2	1/23/70	Local buckling of tank support ring (system-level testing).	Installation of misaligned oxidizer vent nozzle deformed ring causing buckling under load.	Doubler bonded to ring to decrease sensitivity to misalignment. The brazing tool was modified.
3	2/4/70	Failed upper fitting on end truss (system-level testing).	Originally believed to have been caused by item 2. In reality, same cause as item 4.	The subassembly was replaced and testing continued.
4	2/6/70	Cracked upper fittings (4) on center and end trusses (system-level testing).	Stress riser resulting from insufficient fillet radius.	All fittings along tank centerline were reworked to increase fillet radius to 0.090 (W truss fittings were not changed).
5	4/8/70	Failed upper fittings (4) around oxidizer tank (propulsion subsystem testing).	Shaker control system capabilities exceeded resulting in overtest at critical frequency.	Test controls were improved and expanded. Center and end truss upper fittings were changed to steel.
6	6/26/70	W truss cracked upper fitting (propulsion subsystem testing).	Fatigue-subjected to 35 axes of vibration testing at levels up to and including design ultimate.	All upper W truss mag fittings were replaced and testing was continued.
7	7/8/70	Failed beryllium tube in the upper pressurant tank support (propulsion subsystem testing).	Subsystem-level test loads greater than the minimum allowable for beryllium.	Beryllium tubes were replaced with steel (in these members only). Tanks were response-limited during subsystem testing.
8	7/17/70	Lower pressurant tank support fittings both cracked (propulsion subsystem testing).	Cumulative damage from repeated testing at subsystem level (subjected to 24 axes of vibration).	The tanks were removed and testing completed. N_2 tanks will be response-limited during future subsystem testing.
9	7/22/70	Cracked threads in both mag fittings around inserts (propulsion subsystem testing).	Lead thread and/or C′ sink crushed by insert installation tool.	The suspected parts were tensile-tested to verify integrity. The tool will be modified.

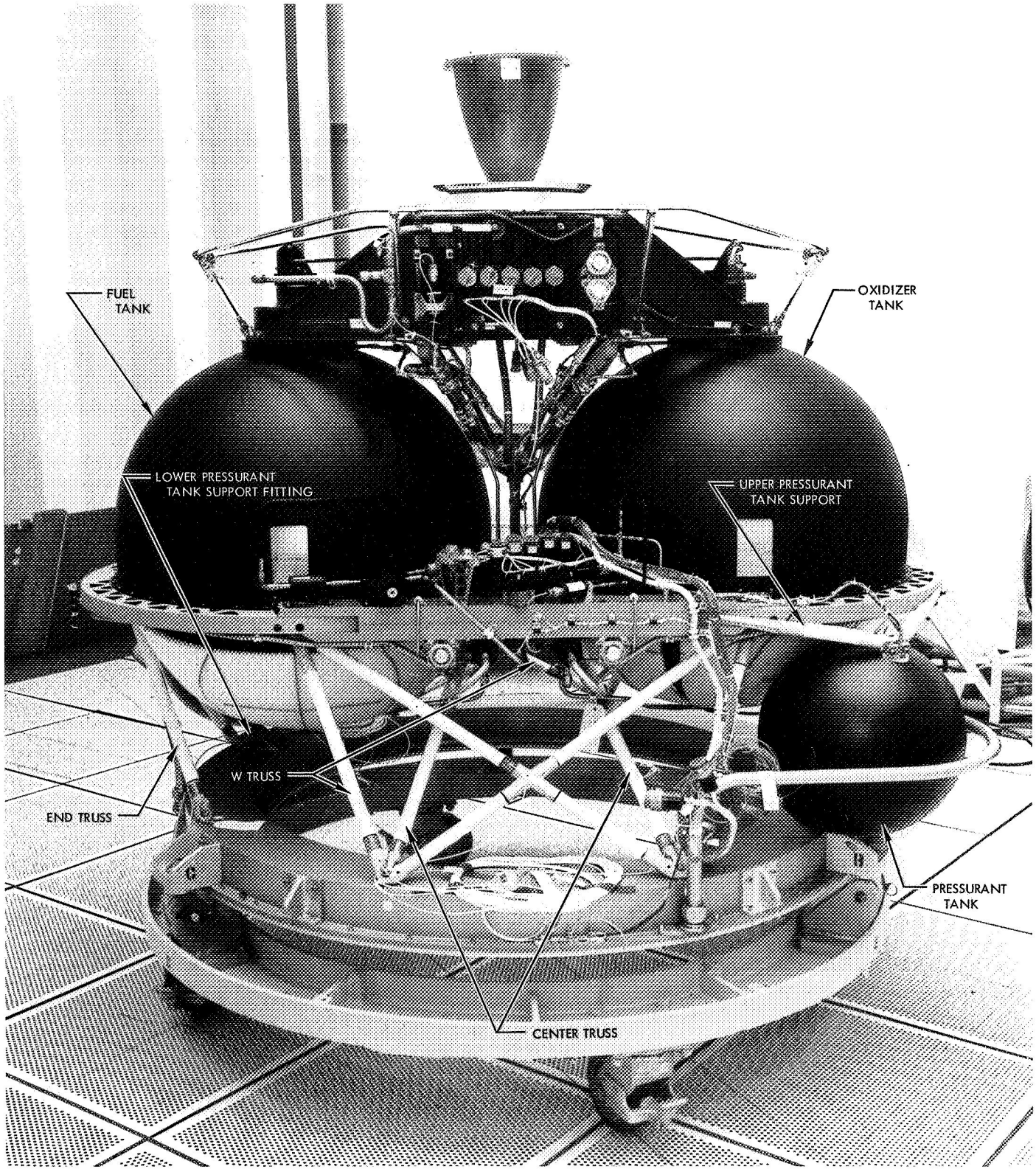

Fig. 32. Propulsion module and support structure

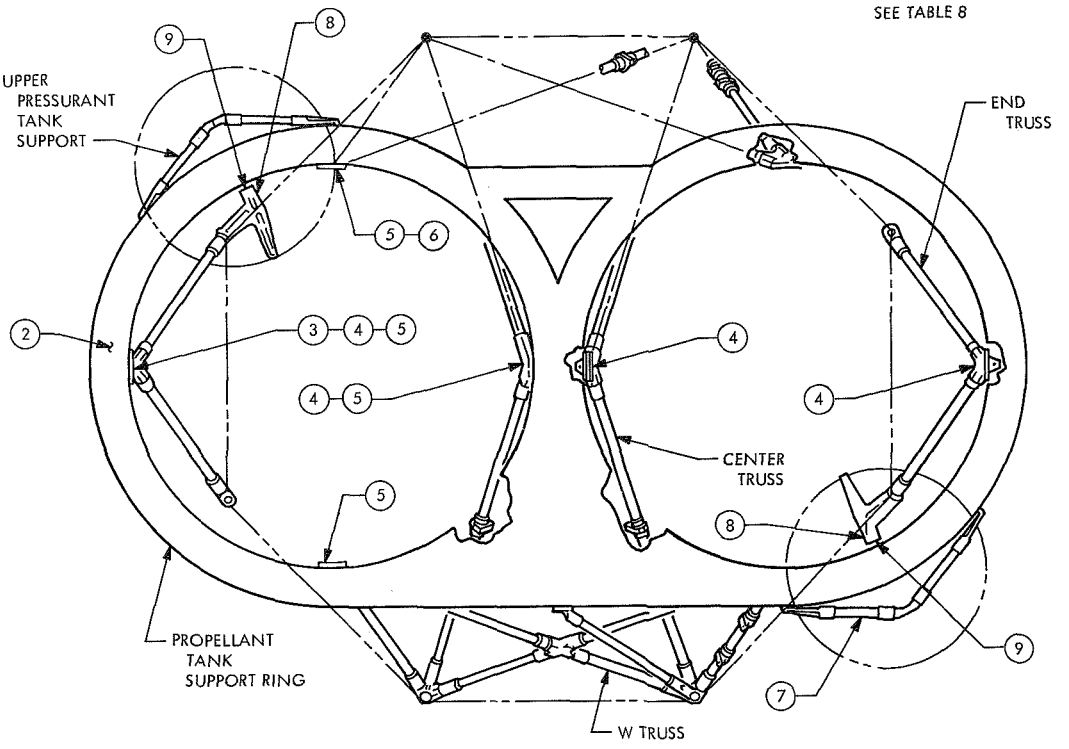

Fig. 33. Support structure failure locations

for continual monitoring of adhesive quality and surface preparation techniques. One specimen utilized an end fitting that allowed improper installation in the pull test machine. The beryllium tube in that specimen failed at an apparent stress level 20% below that experienced in previous specimens. A normalized fracture stress value in the proper range was obtained when bending induced by improper installation was combined with the axial load stress.

Item 2—local ring buckling. Attach points are provided on the under-surface of the propellant tank support ring for the fuel and oxidizer vent nozzles. The tooling used to braze nozzle plumbing created a misalignment between the nozzle and ring and, during assembly, the nozzle was forced into position and the attach screws installed. The resultant deformation, coupled with vibration-induced loads, produced local buckling in the ring. Doublers were bonded to the inner surface of the ring in both vent attach areas to stiffen the ring. Additionally, tooling used in brazing the nozzle plumbing has been modified to preclude misalignment.

Items 3 and 4—upper bipod fittings center and end trusses. During Developmental Test Model (DTM) system-level vibration testing, the upper fitting on one of the end trusses fractured. The bipod containing the broken fitting was replaced and testing continued. After the test, all fittings were examined microscopically. Four upper fittings (both center and both end bipods) exhibited cracks in the fillet radius at the base of the vertical flange (Fig. 34).

Ring buckling (item 2) was originally thought to be the cause of the fracture; however, following discovery of the cracked fittings, a thorough investigation was made. Analysis showed that an unsatisfactory root radius (less than 0.030 in.) resulted in a stress concentration factor greater than 2. All center and end truss upper fittings were modified to increase the root radius to 0.090 in. (Fig. 35).

Item 5—failed upper truss fittings. During Engineering Test Model (ETM) propulsion subsystem testing at the Edwards Test Station, all four fittings supporting the oxidizer tank successively fractured. As each fitting failed, its neighbor picked up a larger share of the load and in turn failed. The ring assembly was damaged locally at each of the fitting locations.

The failures, which occurred within a 45-s period during down-sweep, Z-axis, type approval (TA)-level

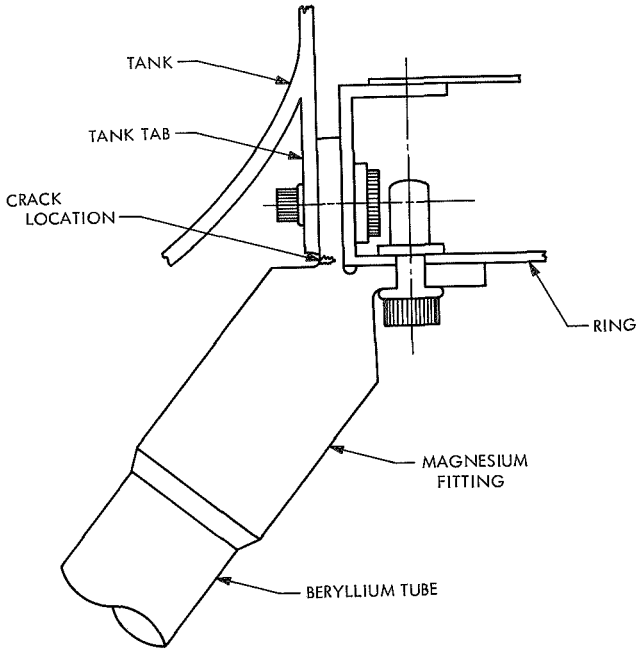

Fig. 34. Vertical flange fillet radius crack location

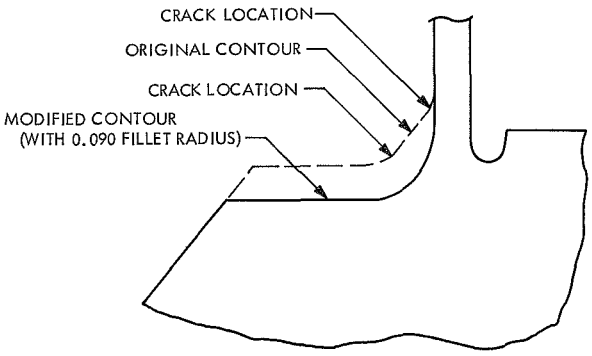

Fig. 35. Vertical flange fillet radius modification

testing, resulted from a 2-times TA test level input overshoot at the first fundamental frequency during upsweep. The test was concluded 1½ min after the first fracture without damage to other hardware.

The overtest did not stem from either operator error or equipment malfunction. It resulted from a previously unrecognized short-coming in the peak control system that allowed overshoot during switching from one control channel to another under certain conditions. The location of the hazardous test shaker, several hundred yards from the control center, precluded manual shutdown of the test as the result of visual or audible warnings. Real-time monitoring of oscilloscopes and printout data did not provide suitable information about the nature of the problem to trigger manual shutdown.

Anomalies with the shaker control have been investigated and the limitations of the system are now understood. Protective trip limiting circuitry has been applied to several of the more critically loaded members for back-up protection. In addition, the upper fittings on the center and end truss members have been changed to steel to preclude additional schedule impact from unit overtesting.

Item 6—cracked W-truss upper fitting. Because of the large number of test runs, the magnesium fittings in the DTM truss were microscopically examined prior to committing it to TA-level testing with live propellants. During the examination, cracks were observed in one of the W-truss upper fittings. The three companion fittings exhibited no sign of cracking either microscopically or under dye penetrant inspection.

The cracking resulted from cumulative damage due to extensive testing at high levels (Table 9). Because all four fittings in the DTM structure had the same test history, they were replaced prior to test continuation.

Item 7—beryllium strut fracture. During z-axis TA-level subsystem testing, one of four beryllium struts in the upper pressurant tank support truss failed. The failure resulted from bending stress induced by N_2 bottle response at its fundamental resonant frequency. The subsystem-level test environment is approximately 50% more severe than in the systems-level tests. Because identical members had successfully survived numerous tests

Table 9. DTM propulsion support structure test history

Test type	Systems testing			Subsystem testing	
	Flight acceptance	Type approval	Design ultimate	Flight acceptance	Type approval
Input level, grms	(0.50)	(0.75)	(0.94)	(1.0)	(1.5)
Z axis	1	1	1	2	2
−XY axis	1	1	1	1	1
+XY axis	1	1	1	1	1
Y axis	1	1	1	1	1

NOTE: In addition to the above, the structure has been subjected to approximately 16 exploratory runs at ½ flight acceptance input levels.

on the DTM (Table 9) and ETM at similar levels, no N_2 tank response control was exercised.

To aid in understanding the problem, a thorough analysis was made of the data obtained during bond specimens testing (see item 1). During the program, 32 specimens were prepared and tested to failure (both bond and beryllium tube) at ultimate tensile load values from 4800 to 8000 lb. Of the group, 16 (ranging in failure at values from 4910 to 7500 lb) for which cross-sectional areas were available, were examined statistically. Though the distribution of this data appears irregular, it should be understood that normal material property variations as well as cross-sectional area differences of 17% are contributors. (Tolerances called out on the tube drawing allowed a 21% spread.) When load values were normalized to stress, ultimate tensile strength values ranged from 53.3 ksi to 78.9 ksi.

Initial findings from the statistical analysis are shown in Fig. 36. Plotted in the figure are the highest load recorded for each of the 16 members in the main truss at each of 12 different loading conditions to which it was exposed (i.e., 12 × 16 data points), all available loading data on the N_2 tank support strut, the statistically derived design allowable tensile load for any beryllium tube in the structure, and the 16 bond-test specimens previously mentioned.

The probability of failure of any of the 16 members in the main truss due to axial loading is remote. It is equally clear from Fig. 36 that the N_2 tank strut loading

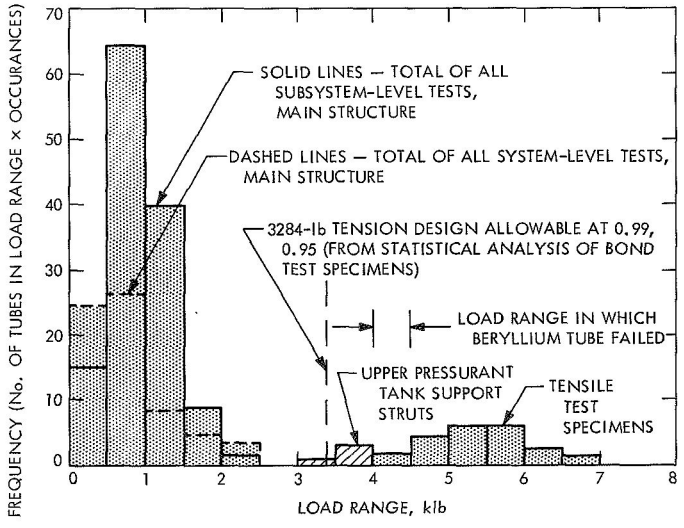

Fig. 36. Beryllium tube loading

exceeds the statistical design allowable bending and the minimum load capability demonstrated by the test specimens.

The four beryllium tubes in the upper pressurant tank support truss have been replaced with 4130 steel tubes, which increases the allowable bending approximately 2.5 times. Response limiting of the N_2 tanks to a level slightly higher than experienced during systems-level testing will be exercised on all future subsystem tests to preclude overloading the next weakest link in the load path.

Item 8—cracks in lower pressurant support fittings. Both lower pressurant support fittings were found to be cracked just prior to concluding DTM pathfinder testing at the Edwards Test Station. The cause was diagnosed to be cumulative damage from repeated subsystem testing. These parts have survived subsystem testing (150% as severe as system-level tests) through 12 exploratory sweeps at ½ flight acceptance (FA) test levels, six axes at FA test levels, and six axes at TA test levels. (Refer to Table 9 for *g* levels.)

Item 9—cracked threads around threaded inserts. After the TA subsystem tests, microscopic examination of lower pressurant support fittings revealed cracked threads in the parent material around the threaded inserts. Several other insert installations were examined and similar crushing of parent material was discovered in all cases. It was found that the insert locking key setting tool was crushing parent material to a maximum depth of 0.030 in. This drive tool will be modified to reduce or eliminate this damage.

Pull tests were conducted to verify the integrity of hardware with cracked lead-in threads. Flight-quality bolts were installed in the inserts and pulled to failure (6500 and 6700 lb tension) without further damage to the fitting or inserts.

3. Solar Panel Deployment/Damper Mechanism Damping Problem

a. Introduction. As reported in SPS 37-63, Vol. I, pp. 25–27, the solar panel deployment/damper mechanism was not providing the minimum critical damping at lower specification temperatures during simulated ¼-*g* motor firings. Careful attention to filling technique and compensator interaction has resulted in predictable

damping performance in excess of the required minimum of 20% of critical. This subsection discusses the approaches that were investigated.

b. Vacuum filling. First efforts were directed toward refining the filling technique to ensure against air entrapment in the damping fluid. A system was devised wherein both the fluid and the mechanism were in vacuum during filling. The fluid was degassed in vacuum and then forced into the mechanism by an externally pressurized piston. (The fill pressure was 50–60 psia.) After pressure equalization, the mechanisms were exposed to the atmosphere to enable the bellows compensator to expand back to its nominal set point. In that way, the mechanism was overfilled and then allowed to return to a nominal condition. The fill plug was ported to minimize air entrapment during sealing. Any improvement in damping performance effected by the refined filling technique was obscured by the normal scatter of data. However, the new technique did give a high degree of confidence that no air was trapped in the fluid.

c. Increase fluid viscosity. The viscosity of the fluid was increased from 200,000 to 300,000 cS. This change eliminated the need for special mixing because 300,000 cS is a standard viscosity. Although the viscosity increase effected a corresponding increase in deployment time and average damping coefficient, the critical damping ratio showed no discernible increase.

d. Redesigning compensator. During the course of testing, two distinct occurrences pointed to compensator coupling as the source of the damping problem. They were: (1) the critical damping ratio decreased with decreasing temperature despite increasing fluid viscosity and (2) the critical damping ratio increased with increasing internal pressure. At low temperatures, the expanded bellows compensator was in a low-pressure state so that resistance to fluid flow into the compensator cavity during a pressure surge was quite low (i.e., fluid flow through the damping annulus was reduced). Conversely, at higher internal pressures, the flow of fluid into the compensator cavity was considerably less, and the desired shear forces were generated as the fluid was forced through the damping annulus. These observations dictated changes that would restrict flow into the compensator cavity.

The damping performance showed some improvement when a flat plate with a 6-mil orifice was interposed between the compensator and the damper. Low-temperature performance, however, was still inadequate. The final step was to replace the bellows with a piston compensator. An air spring and a compression spring in parallel make the piston compensator considerably stiffer than the bellows. The orifice plate was retained in the design to give added flow resistance and to provide a means of restraining the piston during assembly and filling (Fig. 37).

With the new compensator, the nominal internal pressure of the mechanism at +70°F is approximately 4 atm. Proper filling is verified by X-raying the unit and measuring the displacement of the compensator piston. Volume compensation is available from 0 to +160°F. Damping performance of a typical damper is shown in Fig. 38. The damping of the eight flight units has been satisfactory.

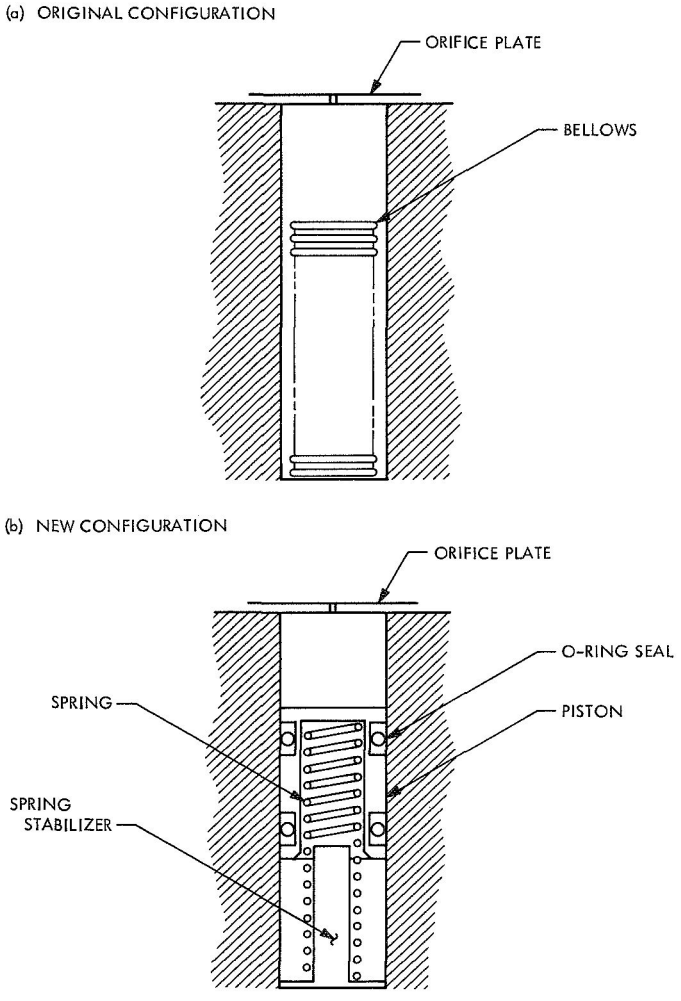

Fig. 37. Compensator cavity configuration

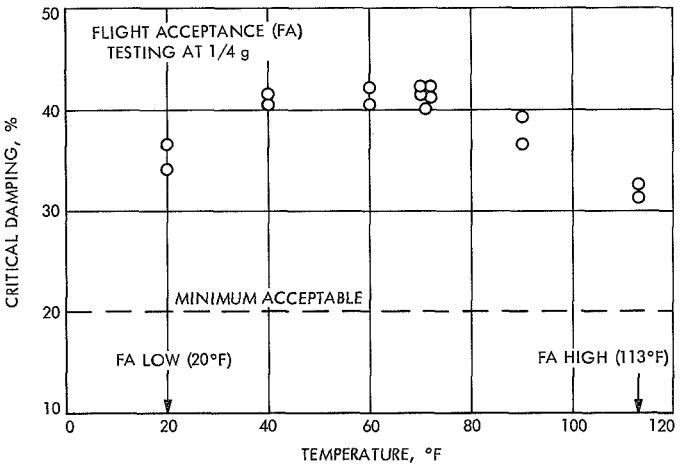

Fig. 38. Solar-panel deployment/damper mechanism critical damping vs temperature

4. Medium-Gain Antenna RF Plug Assembly

The medium-gain antenna RF plug assembly attenuates the radiated energy that impinges on the *Centaur* forward electronics platform prior to separation. The plug is ejected by a release mechanism that is actuated by solar panel deployment.

The telecommunication specialists specified the plug configuration and supplied the RF resistance material from which the plug was fabricated (Fig. 39). Two slats of resistance material are held together by bonding two fiberglass rings to the slats with fiberglass angles. One slat has a guide-pin assembly at each end that consists of a headed stainless steel pin, a mounting tab, and a music wire compression spring. When released, the compression springs provide the necessary force to eject the plug.

The plug is installed into the antenna reflector with the guide pins extending through an aluminum stationary ring bonded to the reflector. The stationary ring serves as alignment for the plug guide pins and as an alignment support for a rotating ring. The rotating ring latches the plug assembly by machined heads on the guide pins. The rotating ring is held in a locked position by a lanyard attached to a stowed solar panel. The solar panel deployment relaxes the lanyard allowing the rotating ring to be turned by two small extension springs. The ring rotates until the guide pin heads align with the holes, thus allowing the plug assembly springs to force the plug out of the reflector.

The plug assembly has six adjustable bumpers that reduce the plug-to-reflector radial clearance to minimize adverse dynamic effects. The clearance is adjusted to 0.002 in. to compensate for the thermal coefficient variation between the plug (fiberglass) and the reflector (aluminum). The antenna–RF plug assembly was successfully ejected at −35°F (which represents the lowest predicted temperature from lift-off to plug ejection).

5. Propellant Tank Fluid Dynamics Tests

a. Introduction. Adequate prediction of the dynamic loads imposed on the spacecraft, either in qualification test or in flight, entails a knowledge of the inertia loads attributable to fluid propellants. While the open literature contains much information on fluid behavior in unbladdered tanks, little information of use to the *Mariner* Program has been available on fluid behavior in bladdered tanks.

A test program was conducted early in 1970 to determine the effective mass and damping coefficient of a fluid in a propulsion subsystem heavyweight test tank subjected to sinusoidal vibration. The frequency range of interest was that of the first several normal modes of the spacecraft on its cantilevered adapter. The results of these tests were inconclusive because of a perforation of the bladder during the course of the tests and the ensuing indeterminate distribution of propellant on each side of the bladder.

Subsequently, a decision was made to launch the spacecraft with the ullage gas at low pressure (e.g., 10 psig) inside of the propellant tank bladders. Accordingly, in May, another test program was initiated to determine the effects of ullage gas placement on the fluid dynamics. These tests, and their results, are discussed in this subsection.

b. Test implementation. Schedule and resource constraints dictated the choice of test method. The test tank and its mounting yoke were supported on flexures from a structural test wall, and resonance tests were conducted with three 150-lb vector-force shakers as the means of excitation. Figure 40 shows the physical setup for lateral vibration. A similar setup was used for vertical excitation.

Two ullage volumes, 4.3 and 10%, were used in each direction of vibration. These volumes correspond to nominal ullages at launch for fuel and oxidizer tanks, respectively. Two complete series of tests were run: one with pressurant inside the bladder at 10 psig, and one with pressurant between the bladder and the tankwall at 50 psig.

(a) REFLECTOR CUTAWAY WITH PLUG DETAIL

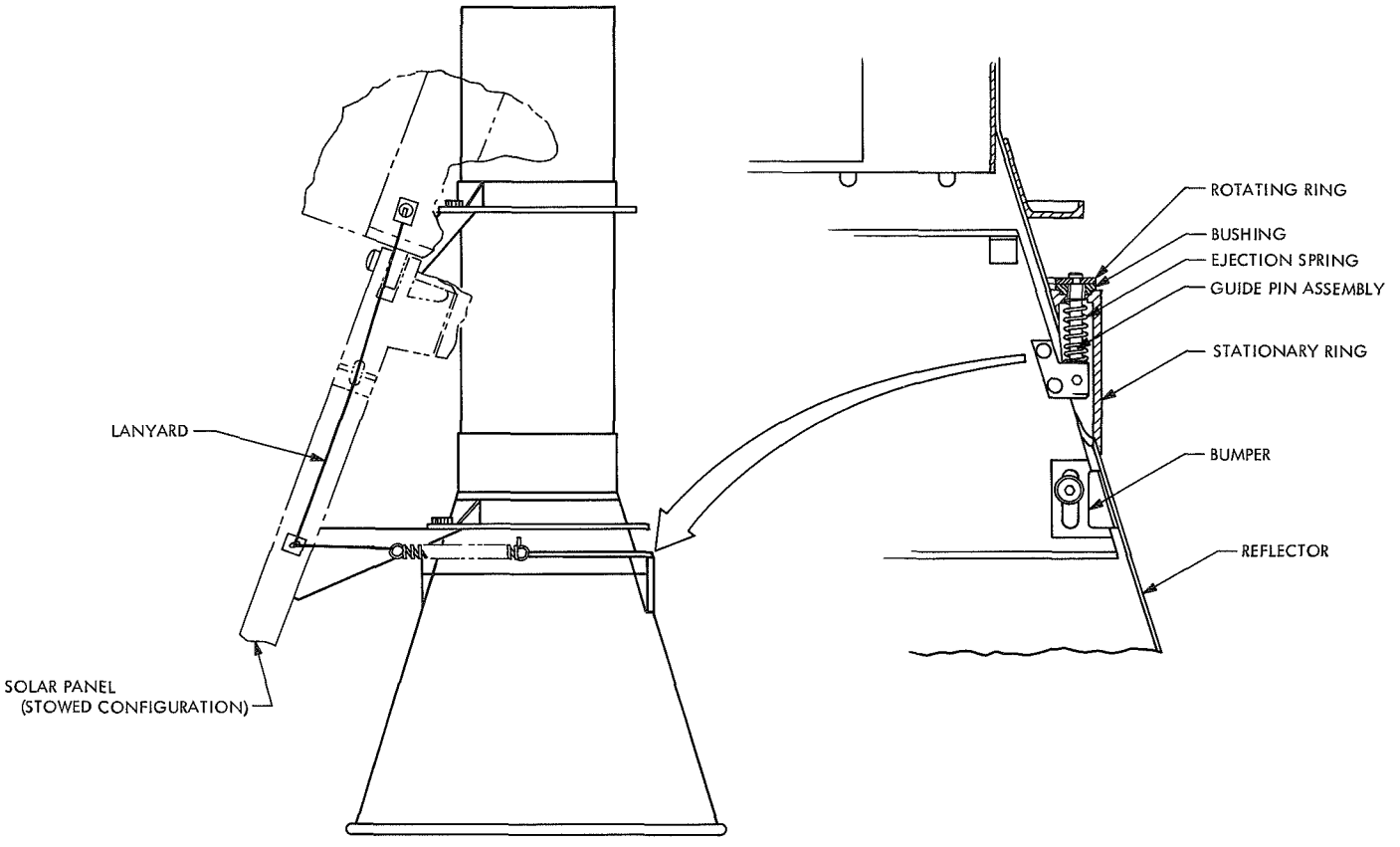

(b) PLUG

(c) ROTATING RING

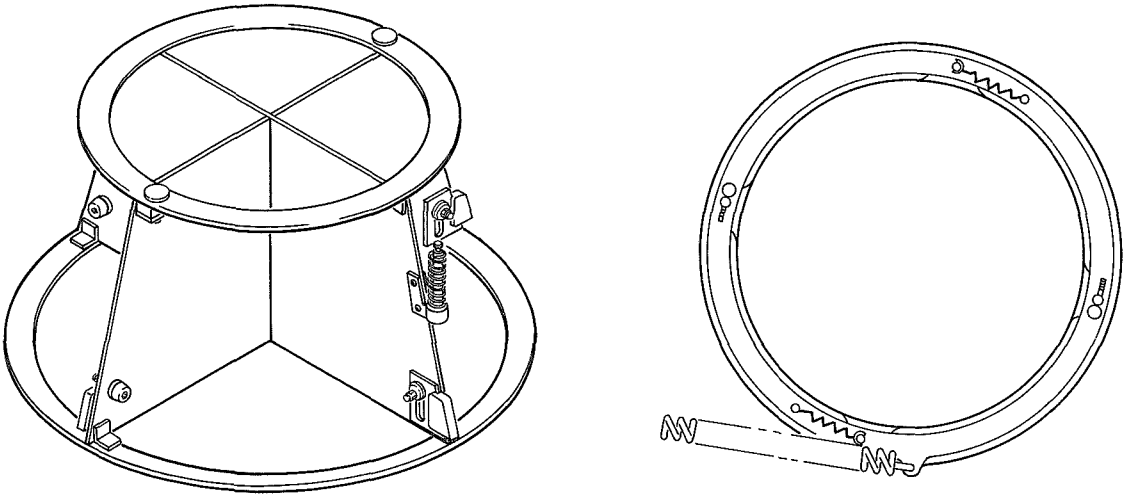

Fig. 39. Medium-gain antenna RF plug assembly

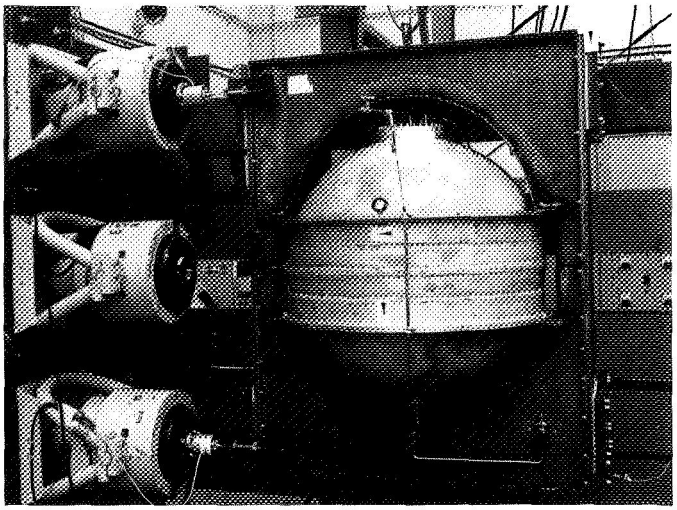

Fig. 40. Test tank setup for lateral excitation

Figures 41–43 present the concept of the test method and the data reduction. For each test configuration, a condition of resonance was established at each of several prechosen rms acceleration levels by adjustment of shaker force and driving frequency to place force in phase with velocity, as observed by a Lissajous pattern on a cathode-ray oscilloscope. The period of the resonance so determined was digitally displayed to five significant figures, with a reproducibility of about 0.03%.

For each test condition (including acceleration level), incremental weights ΔW of about 1% of the gross weight of tank and yoke were added, successively, to permit the plotting of resonant period vs ΔW as shown in Fig. 42.

At the conclusion of the tests, the tank and fluid were replaced with a beam to which additional weights were affixed. The total "calibration weight" W_{cal} of beam and ballast was adjusted to give a resonant period within the range spanned in each of the tank tests. The *effective* weight of the fluid W_{eff} was then determined as indicated in Fig. 42.[6]

The damping provided by the fluid only was determined from data obtained under steady-state excitation (Fig. 43). The difference in force at a specified acceleration level is associated with the damping contributed by W_{eff}.

[6]A more direct means of determining effective weight might have been used had not the structural support of the sprung tank participated in the overall modal response to a frequency-dependent degree.

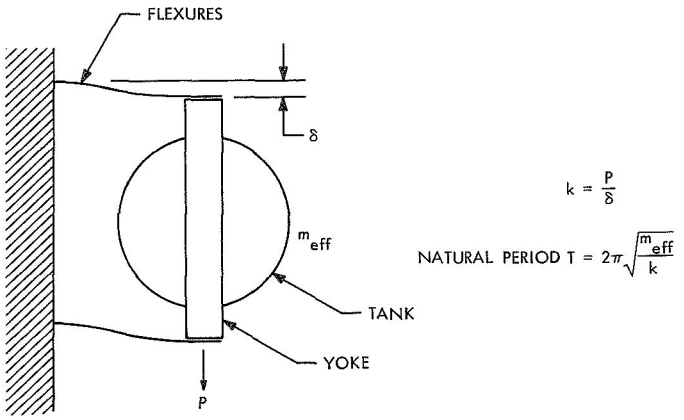

Fig. 41. Sprung support of test tank

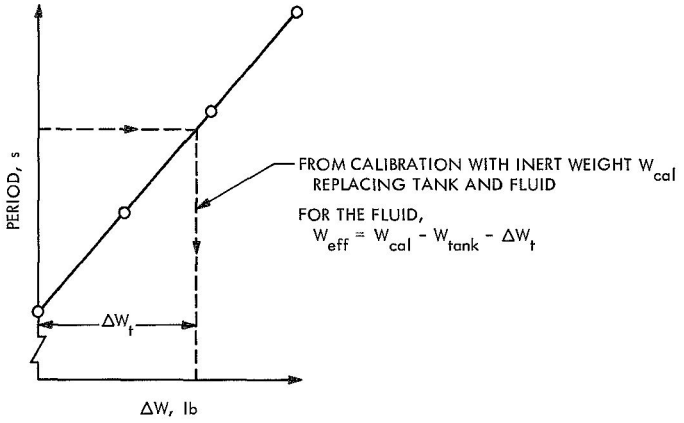

Fig. 42. Graphical means of determining W_{eff}

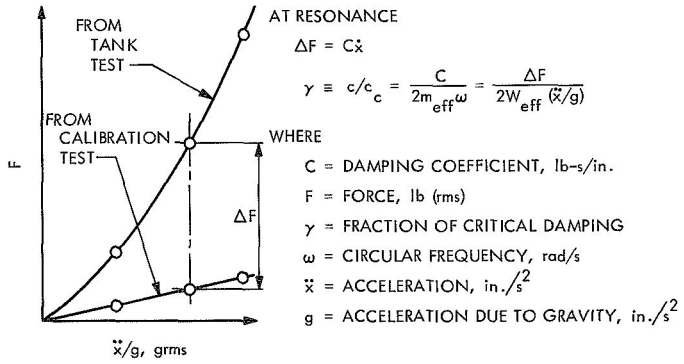

Fig. 43. Method of determining damping coefficient for steady-state excitation

c. Test results. The test results are presented in Figs. 44 and 45.

In Fig. 44, the widths of the dark bands in the plots of W_{eff}/W vs vertical acceleration are indicative of test reproducibility. The associated dispersion in damping

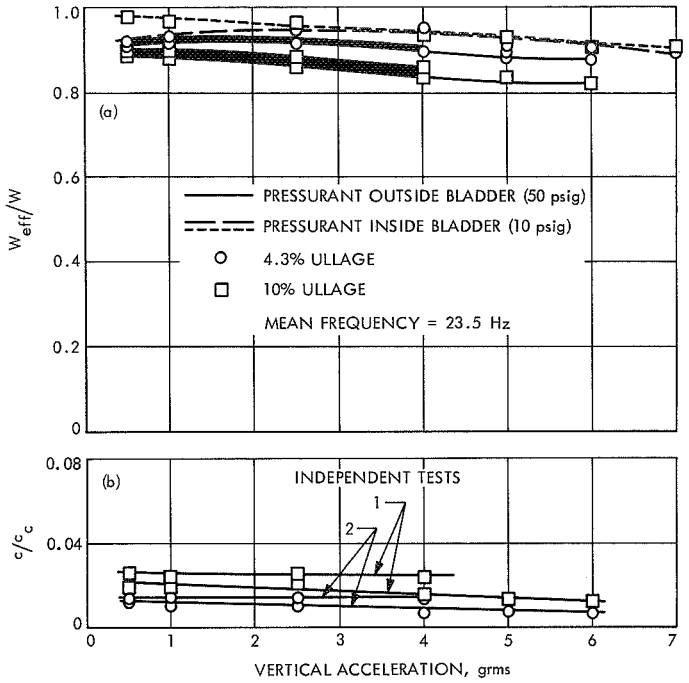

Fig. 44. Dynamic characteristics of fluid under steady-state vertical acceleration ($f >> f_{slosh}$) (damping with gas inside bladder <0.005)

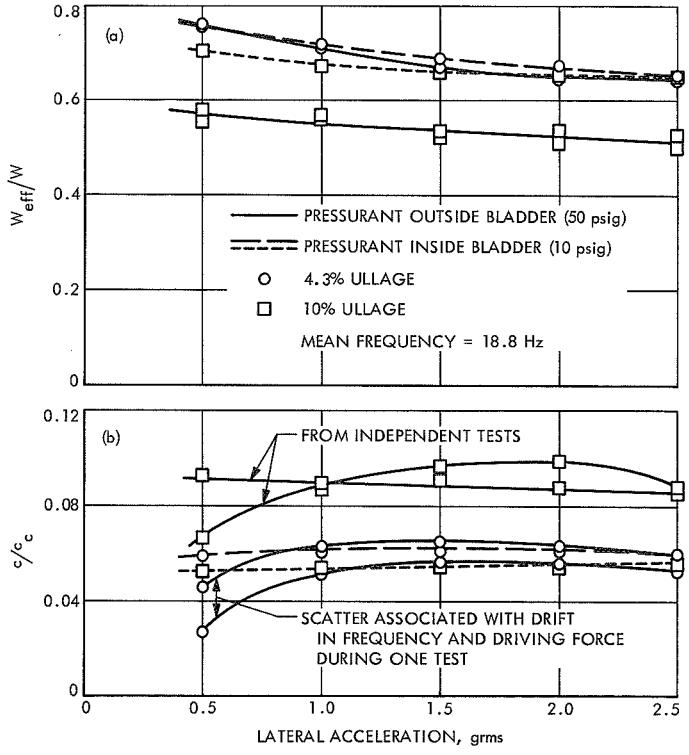

Fig. 45. Dynamic characteristics of fluid under steady-state lateral acceleration ($f >> f_{slosh}$)

ratio for the tests with pressurant outside of the bladder is less than 1%. By virtue of the use of force differences (Fig. 43) to determine damping, the resolution is judged to be no better than 0.005 with the particular setup used.

Figure 45 shows that under lateral excitation, the dynamic behavior of the fluid in the 4.3% ullage configuration is not affected significantly by the placement of the ullage gas. However, in the 10% ullage configurations, the effective mass of the fluid is significantly lower with the ullage gas outside of the bladder. Moreover, the damping ratio, though showing relatively large dispersion in magnitude and trend between the results of independent tests, is significantly higher.

d. Conclusion. In the frequency range of the lower normal modes of the cantilevered spacecraft, the dynamic effects of placing the ullage gas inside of the bladder, instead of between the bladder and the tank wall, are to increase W_{eff} and to reduce the damping ratio. These effects are larger for lateral excitation than for vertical excitation.

If the simple-pendulum mechanical model of the first slosh mode is assumed to apply, then, as an approximation, the slosh weight

$$W_{slosh} = W - W_{eff}$$

The tests described herein contribute no information on the frequency of the first slosh mode nor on the damping in this mode.

6. Cracked Solder Joints on *Mariner* Mars 1971 Flight Equipment

a. Introduction. Two separate cracked solder joint problems have been investigated on the *Mariner* Mars 1971 flight equipment: one in the inertial electronics subassembly (IES), in which an electrical open was recorded; and the other involving both the flight command subsystem (FCS) and data storage electronic subsystem (DSSE).

b. IES flight equipment. The cracked solder joints appeared around the rollover (swaged end) of terminals soldered to the printed circuit board. Although the solder joints were reworked by wicking and soldering in the conventional manner, the cracks soon reappeared. The location of these cracks was at the interface between the solder fillet and the edge of the terminal rollover swage (Fig. 46).

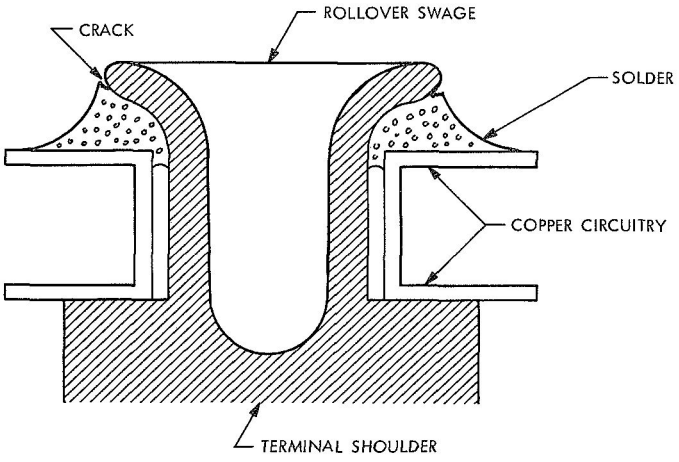

Fig. 46. Cracked solder joint cross-section

The vendor's soldering and handling processes were reviewed; however, no obvious problem areas were found. A simple solderability test was performed on some sample terminals with excellent results. It was concluded that the cracks resulted from stresses caused by the shrinkage of the metal as it cooled from soldering temperatures to room temperature. Due to the swaging operation, the possibility that a less-than-optimum soldering surface at the rollover also existed.

The rework approach selected consisted of the use of a redundant interconnect strap between the rollover and the circuitry (Fig. 47). No additional problems were encountered with these joints.

c. FCS and DSSE flight equipment. The FCS and DSSE design incorporates a unique sandwich construction, i.e., two separate printed circuit assemblies folded together with the welded modules in between (Fig. 48).

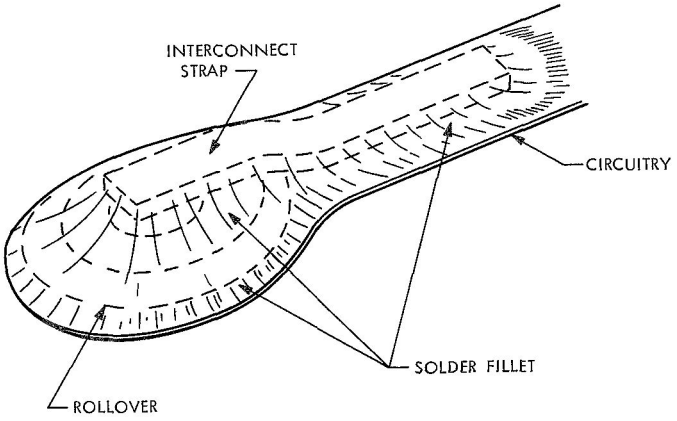

Fig. 47. Redundant interconnect strap

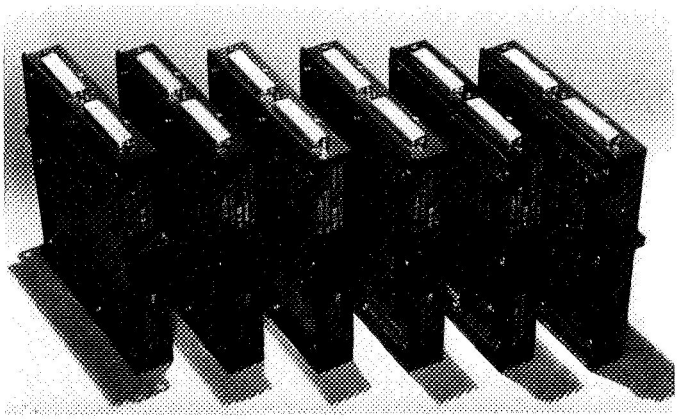

Fig. 48. Flight command subsystem

The modules are soldered to both sides of the printed circuit board resulting in a non-inspectable blind solder joint side and an inspectable visible solder joint side (Figs. 49 and 50).

The cracked solder joint problem first appeared in the FCS on the visible side of the module solder joints as "stress lines" (Fig. 51a). Later, the cracks developed (Fig. 51b). Initial investigation by the vendor indicated that stresses were developed as a result of an accumulation of tolerances that reduced the space provided by the spacers between the printed circuit boards, modules, and conformal coating. The length of the spacers was increased by adding special washers, which appeared to eliminate the undesirable stresses. However, the stress lines and cracks reappeared approximately 1 mo later. A subsequent investigation revealed the following conditions, any one of which could produce stresses sufficient to cause cracks:

(1) Module not physically attached to the printed circuit board.

(2) Short straight through lead with no stress relief.

(3) Very short dwell time in soldering.

(4) No handling fixture through the fabrication phase.

(5) Apparent board warpage.

(6) Soldering procedures (as a whole) apparently marginal.

(7) Cleaning procedures apparently marginal.

Recommendations were made that included a simple soldering test, use of handling fixtures, inspection criteria

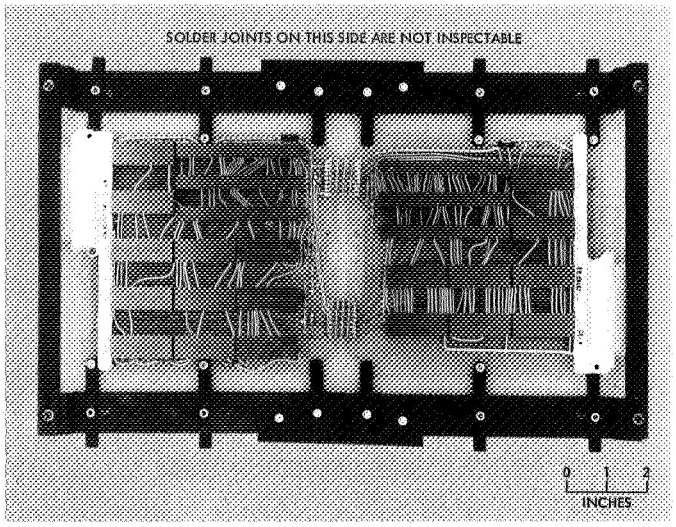

Fig. 49. A subassembly prior to sandwiching

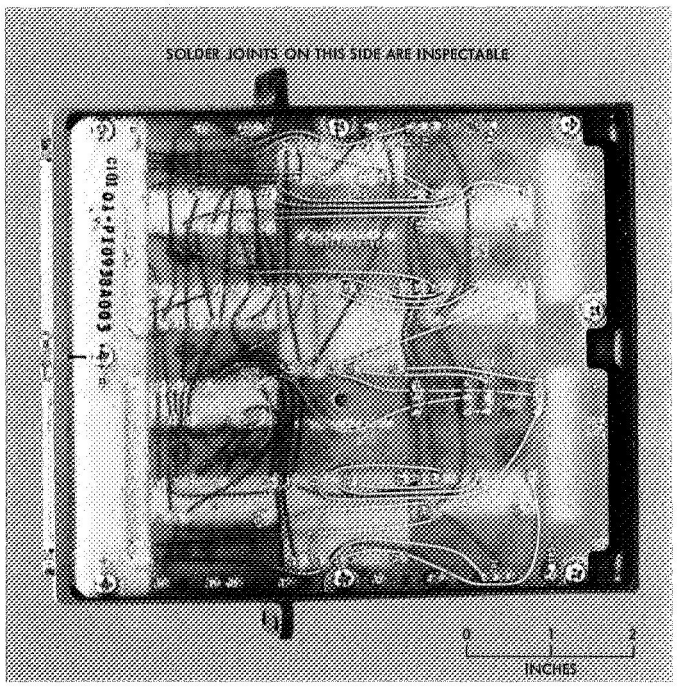

Fig. 50. Side view of sandwiched subassembly

for warpage, specific soldering requirements, and possible design changes. The design changes were considered to be a means of eliminating the problem, while the other recommendations were considered a means of controlling the problem.

Soldering test. The purpose of this test was to determine if the soldering process was the primary cause of cracking; however, the test results indicated that this was

(a) STRESS LINES ON SOLDER JOINT

(b) CRACKED SOLDER JOINT

Fig. 51. Solder joint stress lines and cracks

not the case. As made, the solder joints (including selected control test joints) were stronger than the module lead wire, which failed at a 21-lb load. These joints exhibited creep strength degradation consistent with the text-book predictions.[7] The soldering process was still considered marginal, i.e., it could contribute to the problem, but changing the process would not materially reduce the cracks.

Handling. Attention was focused at upgrading the fabrication handling techniques. Handling fixtures were

[7]Failure mode appearing 24 to 72 h under a constant load of 1000 psi.

adopted for the fabrication of later equipment. This reduced the "in-process" stressing of the solder joints by operating personnel.

Environmental restraints. An analysis was performed of the module–board design to determine the extent of stresses from thermal excursions. The results of this analysis were compared with the solder test results. It was concluded that thermal excursions of 50°C were sufficient to produce a cracked solder joint. Inspection points were established prior to and after vibration and thermal testing to determine the extent of cracking as a result of these tests.

d. Connector solder joint. Because of the added inspection points and increased attention, large quantities of solder joints were being "noted" as unacceptable due to a condition described as dewetting (Fig. 52a). Initially, a number of discrepancies were noted on the FCS welded-module-to-printed-circuit-board solder joints. Prior to testing, the greatest number of discrepancies were observed in the module solder joints. After testing, the greatest number of discrepancies were against the connector solder joints. Then the DSSE began experiencing larger quantities of rejections for dewetted connector-to-printed-circuit-board solder joints. It was concluded, however, that the testing factor represented a point in time more than a condition to produce a discrepant joint.

A DSSE flight printed circuit board with both connectors soldered in place was supplied for the purpose of metallurgical cross-sectioning and examination (Fig. 52b). In addition, a flight-equivalent board with connectors soldered in place was also provided. This board represented the proposed rework by the contractor.

The conclusions drawn from the metallurgical examinations of 22 various solder joints were:

(1) The soldering process was not completed.

(2) The existing flight solder joints could not be reworked by conventional methods.

(3) All the existing solder coatings and copper–tin intermetallic on the lead wires must be removed before an acceptable solder joint can be achieved.

The method of stripping the magnet wire was considered the primary cause for the discrepancies. This, coupled with a marginal soldering process,[8] resulted in

(a) DEWETTED SOLDER JOINT

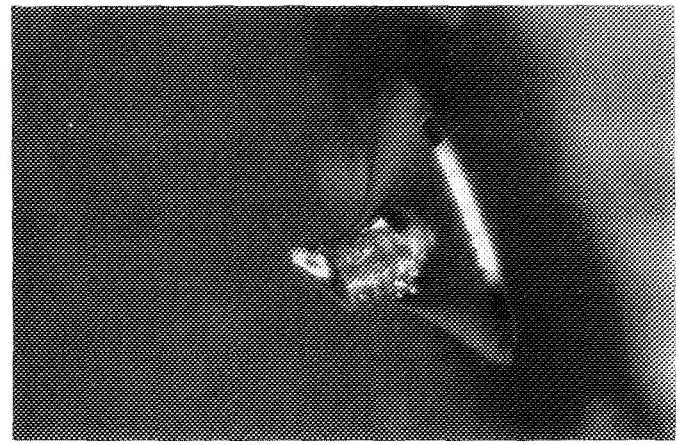

(b) MICRO CROSS-SECTION OF DEWETTED JOINT (90-deg ANGLE)

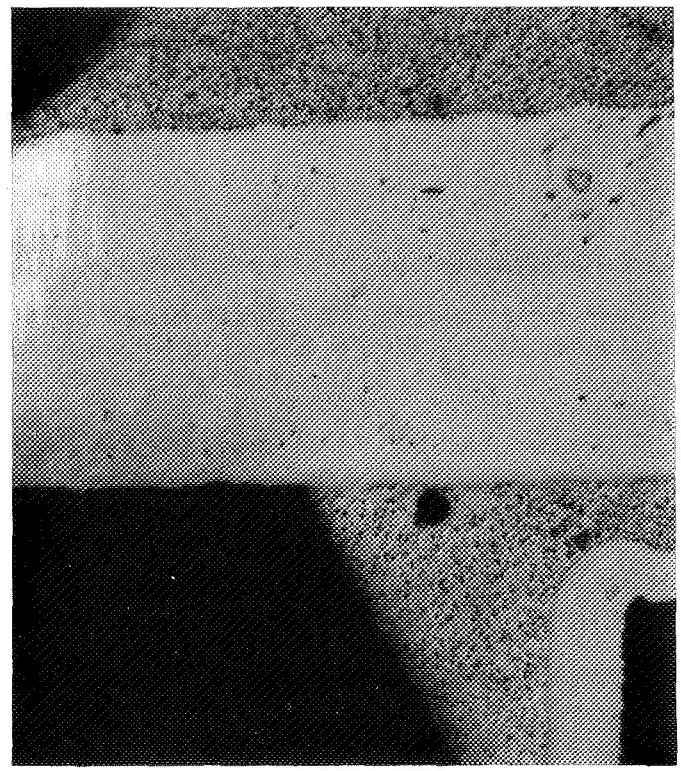

Fig. 52. Dewetted solder joint and micro cross-section

incomplete solder joints. All the connector-to-printed-circuit-board solder joints on the FCS and DSSE were considered to be in this category.

Because of the resource constraints on the Project, it was necessary to resolder the cracked joints rather than rebuild or extensively rework any of the equipment. Samples of the most recent reworked solder joints indicate that three of the four joints sectioned are acceptable.

[8]Not the same as in the soldering tests.

II. *Mariner* Venus–Mercury 1973 Project

A. Project Description

The *Mariner* Venus–Mercury 1973 Project was authorized in December 1969. The primary objective of this first dual-planet mission is to conduct exploratory investigations of the planet Mercury's environment, atmosphere, surface, and body characteristics, and to obtain environmental and atmospheric data on the planet Venus (first priority assigned to Mercury investigations). The secondary objectives are to perform interplanetary experiments enroute to Mercury, and to obtain experience with the gravity-assist mission mode.

A single *Mariner* spacecraft is planned for launch by an *Atlas/Centaur* vehicle from Cape Kennedy in October 1973. The Venus encounter, in February 1974, will provide both an opportunity to obtain scientific data at that planet and the necessary energy, by means of gravity-assist, to reach Mercury some 7 wks later. The spacecraft design is expected to resemble that used in the *Mariner* Mars 1969 mission and that being developed for the *Mariner* Mars 1971 mission, with appropriate modifications defined by the Venus–Mercury mission requirements. The scientific experiments, which include television and other planet-oriented elements together with interplanetary fields-and-particles investigations, were selected by NASA Headquarters during July 1970. These experiments are listed in Table 1, along with the corresponding Principal Investigators and Science Team Leaders. The Deep Space Network and other NASA facilities will be committed to support the mission. It is planned that a System Contractor will be selected in early 1971. The Contractor's effort would encompass the spacecraft detail engineering, system assembly, test and operations, and selected support to other elements of the Project.

Table 1. Experiments and principal investigators

Experiment	Principal Investigator	Affiliation
Celestial Mechanics–Radio Science	H. T. Howard[a]	Stanford University
Charged-Particle Telescope	J. A. Simpson	University of Chicago
Infrared Radiometer	S. C. Chase	Santa Barbara Research Corp.
Magnetic Fields	N. F. Ness	Goddard Space Flight Center
Plasma Science	H. S. Bridge	Massachusetts Institute of Technology
Television Science	B. C. Murray[a]	California Institute of Technology
Ultraviolet Spectroscopy	A. L. Broadfoot	Kitt Peak National Observatory

[a]Science Team Leader.

B. Environmental Sciences

1. High-Intensity Solar Simulation

High-intensity solar simulation will be required to perform developmental testing of instruments on the *Mariner* Venus–Mercury 1973 spacecraft that will be exposed to the solar radiation. The radiation intensity level expected is 5.4 times that at Earth or 700 W/ft^2. A test has been conducted in the 10-ft space simulator using a small collimating mirror to produce a small high-intensity beam. The purpose of this test was (1) to determine the uniformity of intensity throughout the beam using the existing integrating lenses, which are not geometrically optimized for the optical system thus developed, and (2) to gain experience in the operation of instrumentation exposed to high-intensity solar radiation.

In order to generate a high-intensity beam, all the available energy had to be concentrated in a small diameter. The minimum-size beam that can be generated in the off-axis optical system used here (Ref. 1) is determined by the included angle subtended by the lamp array. In order to utilize all the available energy, the included angle of the exiting beam from the integrating lenses can be no smaller than the included angle of the lamp array. In practice, a small collimating mirror was placed close to the integrating lenses to intercept the beam at a diameter adequate to produce a reflected beam of required intensity (Fig. 1). The internal geometry of the chamber required the reflected beam to be inclined 10 deg from the vertical.

The instrumentation used to determine the beam parameters were a radiometer to measure the absolute intensity and a pair of silicon solar cells to measure the uniformity of intensity. The location of these instruments is shown in Fig. 1. The radiometer was stationary at all times and measured the intensity of only one spot in the beam. The two solar cells were connected in a ratioing circuit, with one cell being moved throughout a plane

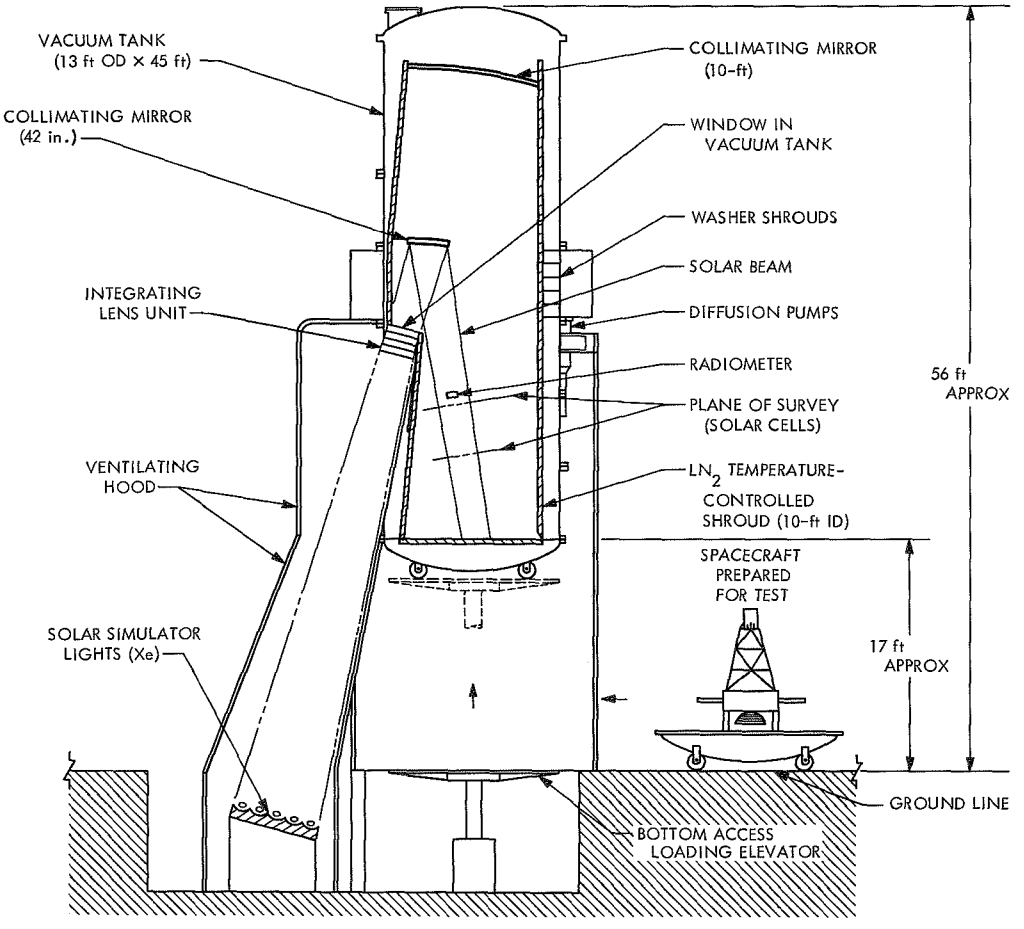

Fig. 1. Cross-section of the 10-ft space simulator

while the other was held stationary. Thus, the output data showed the relative intensity of one cell to the other. Two planes were surveyed: one approximately 6 ft above the chamber floor and the other approximately 10 ft above the floor. Both planes were perpendicular to the axis of the solar beam. The tests were run using 10 of the 5-kW xenon compact arc lamps, which resulted in an intensity of 767 W/ft^2. The uniformity of intensity was $\pm 5\%$ for a 2-ft-diam beam within each of the two planes surveyed. It was not possible to measure the difference of absolute intensity from one plane to the other, but the theoretical value is about 2%. The collimation angle, which is the angle of divergence of the worst ray from the central axis, was determined optically using a theodolite. This was ± 4.5 deg at the edges of the beam.

A final test was run to measure absolute intensity only. Due to the resultant high heat load, the surveying mechanism was retracted from the beam area and only the radiometer, which is water cooled, was operated. For this test, 19 of the 5-kW xenon arc lamps were used, which produced a beam of 1415 W/ft^2 intensity. For simplicity of operation, all tests were run with the chamber at atmospheric pressure.

The data from the tests indicates that an acceptable uniformity of intensity is produced using the existing integrating lenses. However, the rather large collimation angle would affect shadows on a test item having a large depth of field, such as 1 ft or greater. All the instruments used during the tests operated satisfactorily for the relatively short time they were exposed to the high-intensity radiation.

Reference

1. Bartera, R. E., and Barnett, R. M., *Development of the Jet Propulsion Laboratory Solar Simulator, Type A,* Technical Report 32-638. Jet Propulsion Laboratory, Pasadena, Calif., July 15, 1969.

III. *Viking* Project, Orbiter System and Project Support

A. Project Description and Status

1. Description

The primary objective of the *Viking* Project is to significantly advance the knowledge of the planet Mars by direct measurements in the atmosphere and on the surface and by observations of the planet during approach and from orbit. Particular emphasis will be placed on obtaining information concerning biological, chemical, and environmental factors relevant to the existence of life on the planet at this time, at some time in the past, or the potentials for the development of life at a future date. Two spacecraft, each consisting of an Orbiter System and a Lander System, are planned for launch during the 1975 opportunity. The Orbiter System is being developed by JPL; the Langley Research Center is responsible for the Lander System, which is being developed under contract by the Martin Marietta Corporation. Langley has overall management responsibility for the *Viking* Project.

The orbiter will transport and insert the lander into Mars orbit at the appropriate point for a given range of preselected landing areas. The topography of Mars will be mapped during orbital operations, with special emphasis on mapping proposed landing sites prior to deorbit of the lander and on supporting the lander after it is on the surface of Mars by determining if changes are apparent in the vicinity of the lander. After the lander has landed, the orbiter will relay telemetered data from the lander to earth. Scientific instruments on the orbiter will be used to measure atmospheric and surface parameters at various times and locations to determine the dynamic characteristics of the planet. Both visual and infrared coverage will be possible during the presently planned 140 days of orbital operations.

During entry the lander will measure Mars' upper atmospheric composition and lower atmospheric temperature, pressure, and density. After landing, surface soil analyses will be conducted by an integrated biology instrument to detect evidence of biological growth and/or metabolism and by a gas chromatograph/mass spectrometer to measure the molecular composition with particular emphasis on determining organic compounds. In addition, the landing site and surrounding areas will be mapped visually, and measurements will be made of the planet's atmospheric composition, temperature, pressure, humidity, and wind speed. Seismological, magnetic, and physical properties will be determined.

2. Status

A significant effort was concluded to support the Project-wide Mission Trade Study Review. A number of

action items were assigned to JPL, with responses due for most items by the end of August 1970. Efforts are continuing in support of the Project Preliminary Reference Mission.

Initial sections of the Orbiter Design Book have been released and draft copies of other sections of this document are under review. Several Orbiter Control Documents, for internal operations, were completed and released; these included the Design Review Plan and Orbiter Procurement Instructions. The *Viking* Orbiter Office provided support to a Project-wide review of documentation. A detailed internal review of the work elements necessary for the complete Orbiter Imaging Investigation was initiated, and significant planning information was obtained as a result.

Final assembly of the Gas Chromatograph/Mass Spectrometer Engineering Breadboard is underway, and instrument tests are being conducted. Integration of the Instrument Data System with the Engineering Breadboard is expected immediately after the close of this reporting period. Physical configuration studies of the Engineering Model are in progress.

Adjustments are being made in the FY71 Orbiter operating plan to attain consistency with the resources available to the *Viking* Project.

B. Guidance and Control

1. Power Subsystem

a. Power requirements. During this reporting period, the power profile has been revised to include a 2% allocation of power required for operation off the solar panel maximum power point, a 42-W subsystem contingency, and refinements to some subsystems. As a result, the total energy required during the orbit insertion maneuver has been reduced to approximately 920 W-h. The reduction in battery energy required was also due to the decision to eliminate a 60-min sun occultation period immediately following the orbit insertion maneuver (SPS 37-60, Vol. I, pp. 37–44). On this basis, the battery depth of discharge has been reduced to approximately 53%. This is a reduction of 17% from the original 70% allowed during the original baseline design. (SPS 37-56, Vol. I, pp. 42–47.) A summary of the latest total power requirements is given in Table 1.

b. Solar panel. The available power from the solar panels for *Viking* Orbiter 1975 has been reviewed based upon more recent trajectory and temperature data. Also contributing to the updated performance predictions are the data accumulated from the in-flight operation of the *Mariner* Mars 1969 solar panels. Since the general environmental predictions for *Viking* Orbiter 1975 are similar to those experienced by *Mariner* Mars 1969, and the manufacturing processes and specifications are expected to be comparable, losses in power are considered to follow parallel patterns.

Table 1. *Viking* Orbiter preliminary power profile

Operational mode	Power requirement, W	Power source
Launch	546	Battery
Sun acquisition	473	Battery
Canopus acquisition	476	Solar panels
Cruise, high-rate battery charging on	518	Solar panels
Cruise, low-rate battery charging on	462	Solar panels
Cruise, lander capsule TWT maintenance	536	Solar panels
Trajectory correction/orbit trim	560	Battery
Orbit insertion maneuver turns	343	Battery
Orbit insertion maneuver burn	392	Battery
Solar occultation, post orbit insertion	320	Battery
Orbit cruise with lander capsule, battery charging on	520	Solar panels
Orbit cruise with lander capsule	466	Solar panels
Orbit cruise with lander capsule, science on	582	Solar panels
Solar occultation with lander capsule	478	Battery
Orbit cruise with lander capsule, high-rate battery charging on, science playback	550	Solar panels
Orbit cruise with lander capsule, science playback	478	Solar panels
Lander capsule preseparation checkout	470	Solar panels
Lander capsule initiate separation, gyro warm-up	490	Solar panels
Lander capsule initiate separation, S − 2.5 h	919	Solar panels/battery
Lander capsule initiate separation, S − 2.0 h	824	Solar panels/battery
Lander entry, relay on	406	Solar panels
Orbit cruise, lander capsule separated	421	Solar panels
Periapsis pass, science and relay on	555	Solar panels
Orbit cruise, science on, relay off	532	Solar panels
Solar occultation, lander capsule separated	433	Battery
Orbit cruise, high-rate battery charging on, science playback, lander capsule separated	500	Solar panels

The mechanical configuration of the solar panels, upon which the predicted power is based, is a gross panel area of 158 ft² (142 ft² net solar cell area); the substrate is assumed to be of the sheet stringer type used on previous *Mariner* missions and temperature characteristics are similar.

During the early investigations, it was determined that, based on *Mariner* Mars 1969 performance and the predicted space environment for *Viking* Orbiter 1975, some reduction in weight and cost could be accomplished by reducing the solar cell and coverglass thicknesses from those specified for *Mariner* Mars 1969. The coverglass thickness has been reduced from 20 mils to 6 mils, and the solar cell thickness from 18 mils to 14 mils (SPS 37-60, Vol. I, pp. 36–37). Neither of these changes will result in increasing the risk of the solar panel development.

Solar panel power, for design purposes, has been calculated for *Viking* Orbiter 1975 utilizing the JPL M-132 computer program. Predictions have been made for both trajectories A (launch August 16, 1975, arrival August 1, 1976) and B (launch August 19, 1975, arrival September 2, 1976).

Figures 1 and 2 are power vs voltage curves for each trajectory indicating the available power at the time of launch, planetary orbit insertion, and approximately 40 days after orbit insertion. Trajectory B (Fig. 2) also depicts the power available 79 days prior to orbit insertion, which, for this trajectory, is the time of minimum power availability. Minimum available power for trajectory A occurs 16 days prior to orbit insertion. However, since the difference in power between orbit insertion and minimum power is so small (3 W at maximum power), this curve has been omitted from Fig. 1 for simplification.

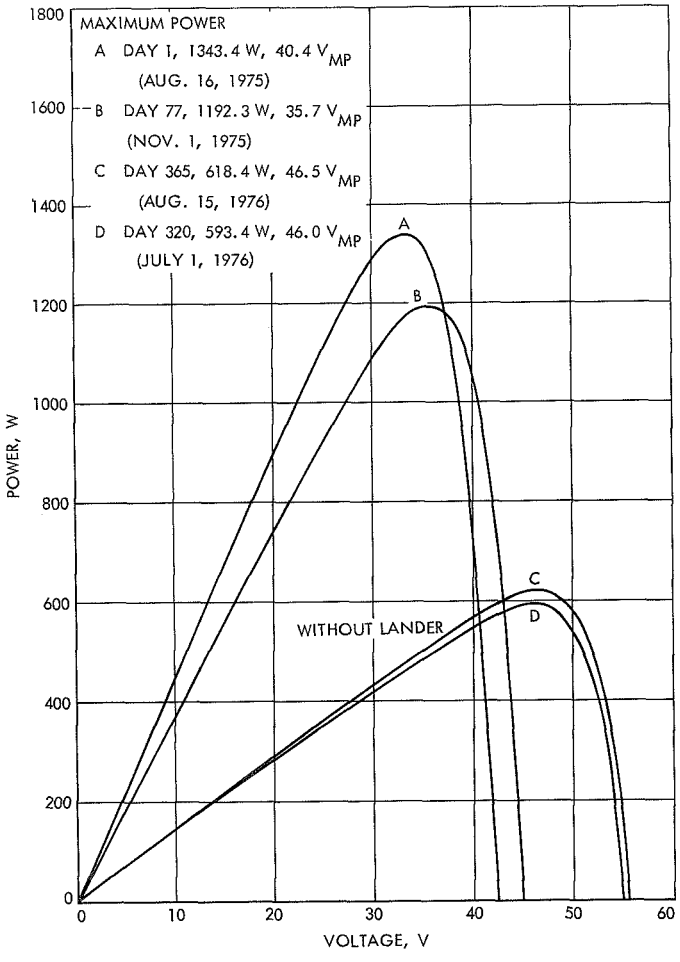

Fig. 1. Trajectory A power vs voltage

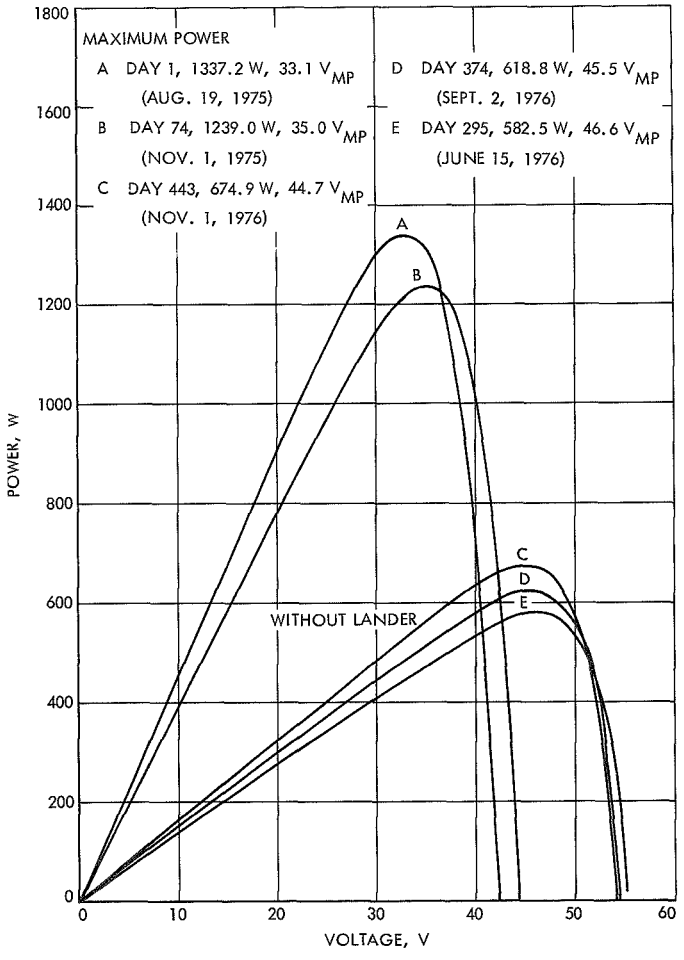

Fig. 2. Trajectory B power vs voltage

At this time, the effects of planet albedo have not been calculated precisely. The warming effects of planet albedo at periapsis have been estimated to be as much as 12°C. An increase of this magnitude in panel operating temperature could result in as much as a 5% loss in power during this period. Losses which have been included in predicting the available design power are as follows:

Condition	Losses, %
Fabrication losses	6
Contingency for packing factor and fabrication uncertainties	4
In-flight degradation due to effects of space environment	8
Contingency for performance prediction accuracy	4
In-flight degradation due to neutron environment induced by the onboard radioisotope thermoelectric generator	2
Total assumed power losses	24

c. Battery charging. Present studies related to the 1975 Mission indicate that the battery charge rate (C/15) selected for the 1973 Mission (SPS 37-61, Vol. I, pp. 28–32) may not be adequate. Under certain operating conditions (sun occultations, share modes, temperature extremes, etc.), it is possible that the rate may not be high enough to sufficiently recharge the batteries between required discharges. Therefore, it is apparent that an additional rate (C/10) must be included in the design of the charger to meet all mission conditions. One of three charge rates: high (C/10), medium (C/15), and trickle (C/40) will be selected by ground command. The actual high and medium current rates will be chosen such that the spacecraft can accommodate all expected combinations of mission parameters. A comparison of the *Viking* Orbiter 1975 nickel–cadmium battery charging times vs depth of discharge and available battery capacity for both the C/10 and C/15 rates is shown in Fig. 3.

2. Reaction Control Assembly

The FY70 activity on the *Viking* Orbiter reaction control assembly (RCA) was addressed to the definition of both the assembly characteristics and the components requirements.

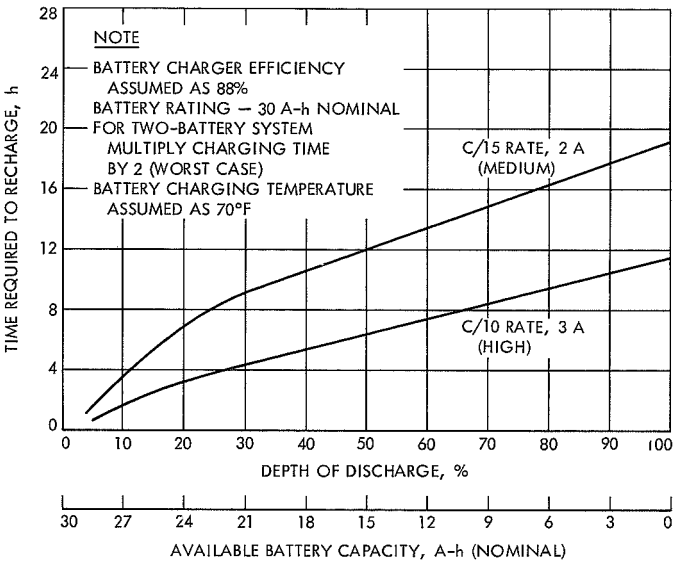

Fig. 3. Nickel–cadmium battery charging time vs depth of discharge and available battery capacity

The RCA requirements have been preliminarily identified in terms of performance, weight, configuration, and ground handling procedures using the mission requirements and the spacecraft overall configuration definition. The *Viking* Orbiter RCA (Fig. 4) will be essentially a *Mariner*-type, dual-redundant, cold-nitrogen thruster system. Alternate configurations (i.e., a dual thrust-level configuration, a single pressure vessel configuration, and others) were examined for the purpose of reducing the overall expected assembly weight, but the slight improvement did not warrant their selection for the *Viking* Program.

The primary changes from the *Mariner*-type RCAs have stemmed from considerations of spacecraft geometry, increased spacecraft inertias, and environmental requirements. The larger size of the *Viking* spacecraft, and the presence of the lander capsule, affects the location of some of the RCA components. For instance, the high-pressure subassemblies are now located inside two diametrically opposed bays in the spacecraft bus, instead of on the upper surface of the bus. Also, the larger spacecraft will require some special consideration for the configuration of the low-pressure lines to allow convenient subassembly handling flexibility. The handling of the *Mariner* RCA assemblies is performed by means of special frames simulating the spacecraft bus and solar panel configuration. These frames are used for RCA shipping, ground testing, and spacecraft assembling. The greater length of the *Viking* RCA low-pressure lines will probably yield a multiple folded configuration to reduce

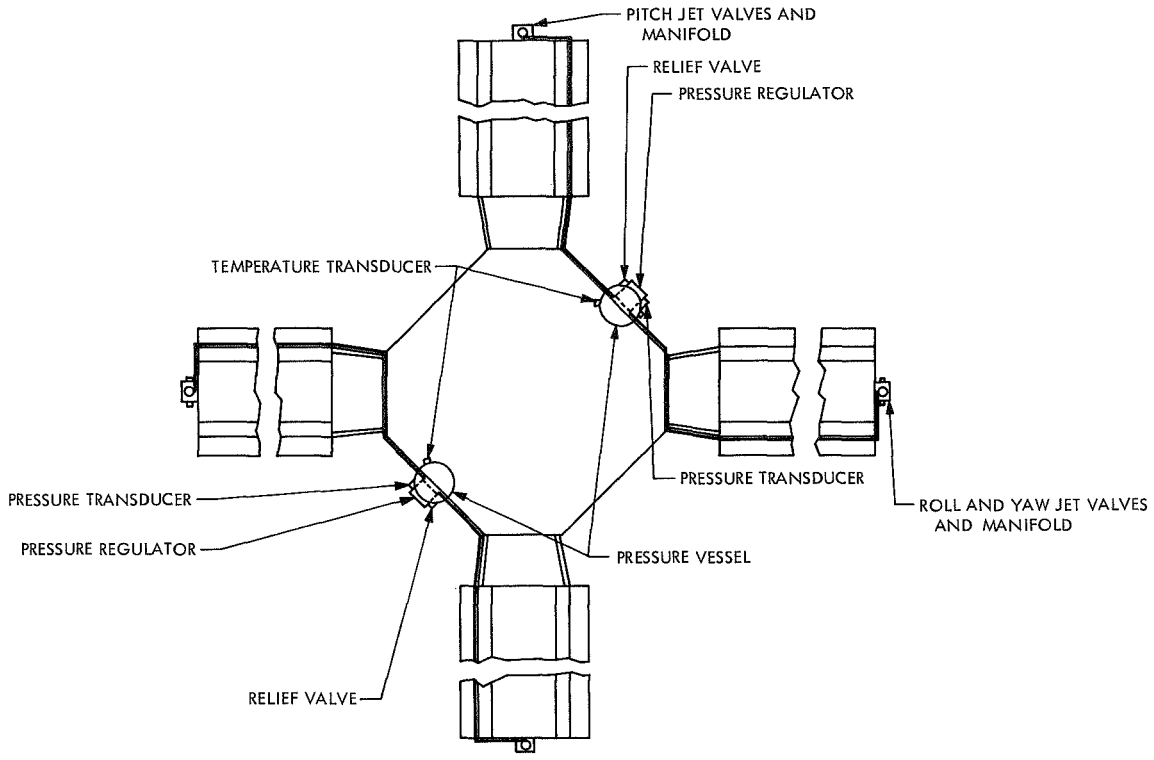

Fig. 4. *Viking* Orbiter RCA

the handling frames and the shipping container to a reasonable size. The RCA component capability must increase due to the higher total impulse requirements for the *Viking* Mission and the higher thrust levels associated with the increased spacecraft inertias. *Viking* RCA thrust levels will be one order of magnitude higher than those of previous *Mariners* (i.e., from 5.5 to 67 mlb) in the pitch and yaw directions; therefore, the component (pressure regulators, jet valves, tubing) flow rate capability must increase accordingly. Environments associated with the new launch vehicle, the long sun occultation periods during Mars orbit, and the presence of radioisotope thermoelectric generators in the lander will also place new requirements on the RCA.

Table 2 shows the values of significant parameters applicable to the *Mariner* Mars 1969 and to the *Viking* RCAs. At this time, the values relative to *Viking* are only approximate and subject to changes following more specific mission definition.

The difference in the high-pressure level is due to the *Viking* requirement for keeping the pressure vessel size within the limits defined by the maximum bay size in the spacecraft bus. The associated weight penalty is approximately 1 lb per vessel. The weight of the pressure vessel was estimated using the new fracture mechanics approach developed by the JPL Engineering Mechanics Division. With this approach, nondestructive testing at cryogenic pressures equivalent to the normal temperature burst pressure will be possible for each unit, including flight units, thereby providing additional safety control. The higher value of the low-pressure level is aimed towards a reduction of the relative uncertainty in pressure regulation and possibly a reduction in component size.

Table 2. Comparison of *Viking* Orbiter and *Mariner* Mars 1969 RCA parameters

Parameter	*Mariner* Mars 1969	*Viking* Orbiter
Propellant weight, lb	5.0	26.2
Pressure vessel diameter, in.	8.9	13.8
Initial high-pressure level, psi	2650	4000
Low-pressure level, psi	15	25
Pitch and yaw thrust level, mlb	5.5	67.0
Roll thrust level, mlb	3.3	15.0
Overall assembly weight, lb	28.3	75.0

Additional features of the *Viking* RCA are the presence of a relief valve in each half-assembly and the replacement of the traditional potentiometric pressure transducer with a strain-gage type transducer. The relief valves are required because the self-relieving jet valves used on *Mariner* spacecraft will not be carried over to *Viking* and the more conventional non-relieving valve design is anticipated. The strain-gage pressure transducer was selected because of higher accuracy and lower cost compared to potentiometric pressure transducers. However, the strain-gage transducer will require more power than the old transducers.

Work has been initiated in component selection since it was readily apparent that none of the *Mariner* RCA components would be directly applicable to *Viking* program, with the possible exception of the fill manifold. The major development items are the jet valves and the pressure regulators. A plan has been established to identify as many sources as possible for each component and to select the best options on the basis of an engineering evaluation, including prototype procurement and testing of actual hardware.

3. Inertial Reference Unit Integrator Redesign

a. Introduction. The electronic integrator used in the inertial reference unit (IRU) for the *Mariner* Mars 1971 Attitude Control System is presently being redesigned for the *Viking* Orbiter 1975 Program. Three integrators are used in the IRU in conjunction with three single-degree-of-freedom gyros to provide angular position information during the inertial-hold mode of spacecraft attitude control. Because of recent advances in the state-of-the-art of integrated circuit operational amplifiers, the National Semiconductor devices LM101 and LM108 were considered to be capable of meeting the same low drift requirement (as an active integrator) that the Fairchild μA726 transistor pair and operational amplifier circuitry fulfill for the *Mariner* Mars 1971 Program. Substitution of the LM101 or LM108 devices for the μA726 and associated operational amplifier results in a significant reduction in circuit complexity, thereby reducing the power requirements and increasing the reliability.

Twenty-five each of the LM101 and LM108 devices were obtained and have been screened for open loop gain, input offset current, input offset voltage and drift over a temperature range of +25 to +60°C.

The μA726 device achieves a low integrator drift over a temperature range of 70°C by the use of integral heaters that control the chip temperature. The new integrator design using the LM101 and LM108 devices eliminates the need for temperature control, and thus the need for $\pm$15 Vdc regulated heater power supplies. In fact, the new design has reduced the total component parts count from 128 to approximately 78, with an accompanying reduction in power of over 4 W. In addition, the reduction in parts count has made feasible the substitution of a single-sided printed circuit board for the double-sided printed circuit board required for the *Mariner* Mars 1971 IRU.

The screening data from the LM101 and LM108 indicated that about 70% of these units required temperature compensation. As seen in Fig. 5, the integrator

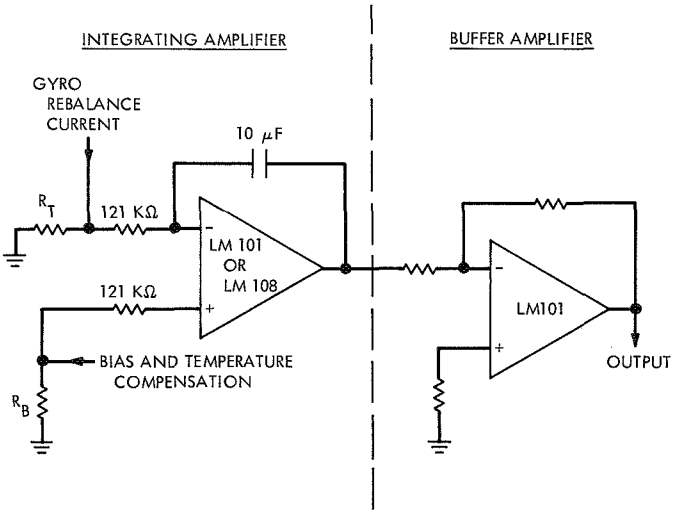

Fig. 5. Electronic integrator partial schematic

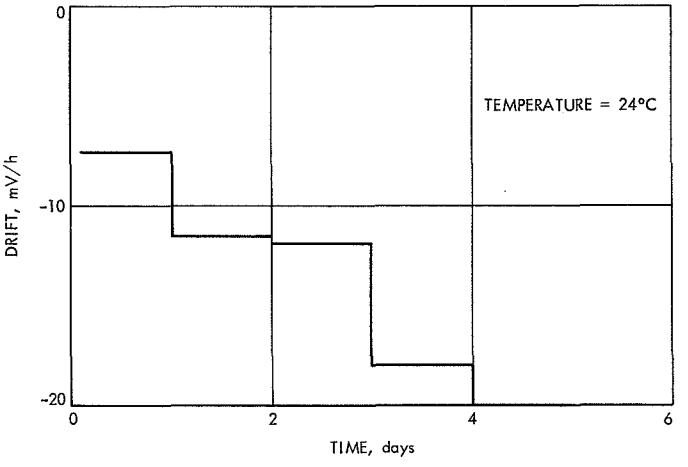

Fig. 6. Day-to-day integrator drift

design features a biasing network to achieve a net gyro and integrator drift of 0.08°/h as initially trimmed. A temperature compensation network (using a sensistor) is also incorporated to maintain a total drift of less than 0.1°/h over a range of temperatures from −10 to +65°C.

b. Test results. The stability of integrator drift is shown in Fig. 6 for day-to-day stability at ambient temperature. Large voltage offset drift at ±5V is shown in Fig. 7; drift changes with temperature (−10 to +60°C) are shown in Fig. 8. The data reflect a typical LM101 device initially biased to a low value of drift at room temperature. As seen from the graphs, the worst-case

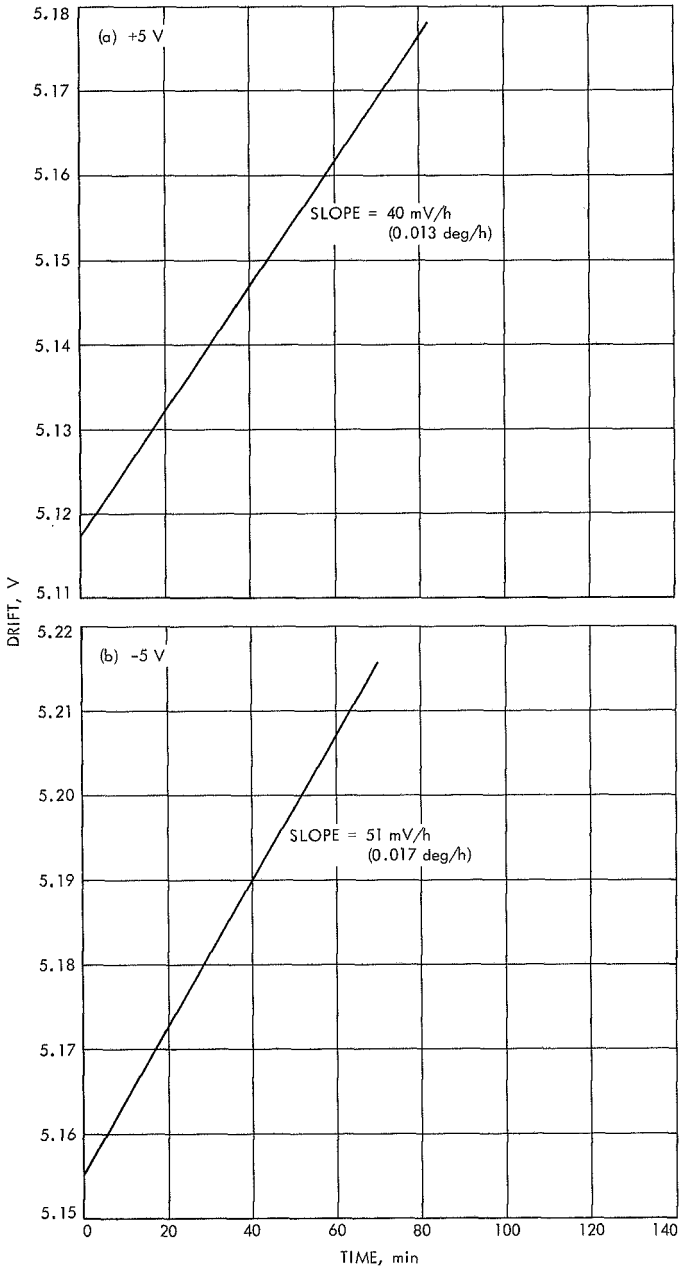

Fig. 7. Integrator large voltage offset drift at ±5 V

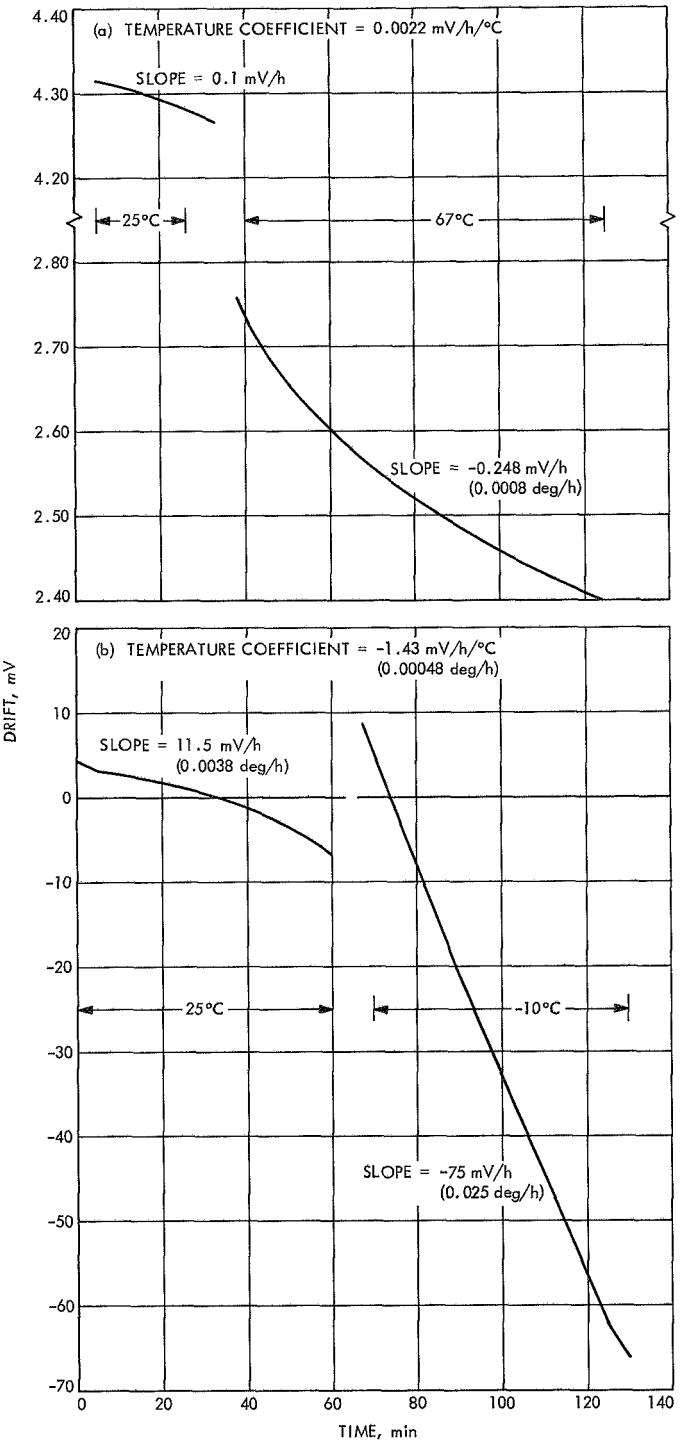

Fig. 8. Integrator drift changes with temperature

drift was 0.024 deg/h for a change of 35°C. The drift values, shown in degrees per hour, are equivalent to gyro drift at the input to the integrator for a measured integrator output voltage change with time. Although the data reflect test results from an LM101 operational amplifier, comparable results were obtained with an LM108.

The test results indicate that the new integrator design will meet a requirement of less than 0.1°/h over the expected operational temperature range of +15 to +45°C.

An LM108 integrator circuit has been evaluated with a gyro in the *Mariner* Mars 1971 IRU breadboard. This circuit was initially trimmed to less than 0.1°/h at room temperature. Total drift (gyro and integrator) remained less than 0.1°/h over a temperature range of −10 to +60°C. Two identical integrator circuits have been breadboarded and continued drift evaluation is planned to demonstrate that the two circuits do not interact with each other in a circuit board layout that simulates a flight hardware configuration.

Subject Index

Subject Index (contd)

NASA — JPL — Coml., L.A., Calif.

N71-14152

TECHNICAL REPORT STANDARD TITLE PAGE

1. Report No. 37-65, Vol. I	2. Government Accession No.	3. Recipient's Catalog No.
4. Title and Subtitle SPACE PROGRAMS SUMMARY, VOL. I FLIGHT PROJECTS		5. Report Date September 30, 1970 6. Performing Organization Code
7. Author(s) JPL Staff		8. Performing Organization Report No.
9. Performing Organization Name and Address JET PROPULSION LABORATORY California Institute of Technology 4800 Oak Grove Drive Pasadena, California 91103		10. Work Unit No. 11. Contract or Grant No. NAS 7-100 13. Type of Report and Period Covered Space Programs Summary July 1 to Aug. 31, 1970
12. Sponsoring Agency Name and Address NATIONAL AERONAUTICS AND SPACE ADMINISTRATION Washington, D.C. 20546		14. Sponsoring Agency Code

15. Supplementary Notes

16. Abstract

The Space Programs Summary is a multivolume, bimonthly publication that presents a review of technical information resulting from current engineering and scientific work performed, or managed, by the Jet Propulsion Laboratory for the National Aeronautics and Space Administration. The Space Programs Summary is currently composed of four volumes:

Vol. I.	Flight Projects (Unclassified)
Vol. II.	The Deep Space Network (Unclassified)
Vol. III.	Supporting Research and Advanced Development (Unclassified)
Vol. IV.	Flight Projects and Supporting Research and Advanced Development (Contents Confidential)

17. Key Words (Selected by Author(s))	18. Distribution Statement
Not applicable for this type of report	Unclassified -- Unlimited

19. Security Classif. (of this report)	20. Security Classif. (of this page)	21. No. of Pages	22. Price
Unclassified	Unclassified	68	